

**OBSERVATION OF TRAPPED-ELECTRON MODE MICROTURBULENCE IN
IMPROVED CONFINEMENT REVERSED-FIELD PINCH PLASMAS**

by

James R. Duff

A dissertation submitted in partial fulfillment of
the requirements for the degree of

Doctor of Philosophy

(Physics)

at the

UNIVERSITY OF WISCONSIN–MADISON

2018

Date of final oral examination: 22 December 2017

The dissertation is approved by the following members of the Final Oral Committee:

John S. Sarff, Professor, Physics
Weixing Ding, Senior Scientist, Physics, UCLA
Paul W. Terry, Professor, Physics
Cary Forest, Professor, Physics
Chris Hegna, Professor, Engineering Physics

© Copyright by James R. Duff 2018

All Rights Reserved

ACKNOWLEDGMENTS

I would like to thank John Sarff and Weixing Ding for advising me through my grad school career.

I would like to thank Eli Parke and Liang Lin for the incredibly useful chats regarding the FIR system, and for helping to keep the system working.

I would like to thank Paul Terry, Dan Carmody, Zach Williams, and M.J. Pueschel for doing very interesting gyrokinetic simulations on the plasmas I study. These simulations, and the explanations that came with them, helped motivate the types of analysis I did, while my data helped motivate the types of simulations that were done. This intergroup cooperation was quite fulfilling, and I'm glad it worked out so well.

I would like to thank the rest of the MST staff for useful discussions, and generally aiding in my work. Keeping the MST running is no easy feat, and I'm grateful to everyone who accomplishes it day to day, from the daily operators to the staff scientists. This work wouldn't be possible without the support of the entire MST team.

I would like to thank my undergraduate professors, Dr. Williams, George, Voytas, Fleisch, and Dollhopf for fostering my interest in physics and introducing me to a wide array of research topics. The opportunity to work with Dr. Jeremiah Williams in a dusty plasma plasma lab led to my interest in plasma physics, and led to some of the prettiest pictures I've ever taken. By keeping the course-work and research challenging (sometimes a bit excessively so), I was never bored during undergrad.

I would like to thank the various friends I've made in Madison, for making my time here so much fun. In particular, I'd like to thank Antonia, Zig, and Goat for ensuring I had a social life while I've been here. From Thanks-physics-givings, to barhopping on a Friday night, to just

relaxing in the middle of lake Mendota, I will cherish many of the memories I've made with everyone I've known here.

Finally, I'd like to thank my wife, Sarah, for being there for me throughout my graduate school career.

DISCARD THIS PAGE

TABLE OF CONTENTS

	Page
1 Introduction	1
1.1 The reversed-field pinch	3
1.2 Improving confinement	5
1.3 Magnetics on the MST	12
1.4 Other diagnostics	12
1.5 Summary	13
2 FIR	14
2.1 Interferometry theory	14
2.2 Polarimetry	20
2.3 The MST FIR system	21
2.4 The FIR upgrade	27
2.5 Summary	29
3 Transport and instabilities	32
3.1 Plasma transport	32
3.1.1 Stochastic transport	32
3.1.2 Heat transport	34
3.2 Microinstabilities	34
3.2.1 The trapped electron mode	36
3.2.2 The ion temperature gradient driven mode	38
3.2.3 The micro-tearing mode	38
3.3 Summary	39
4 Overview of GENE simulations	40
4.1 Modeling	40
4.1.1 Kinetics	40
4.1.2 Gyrokinetics	42
4.2 Gyrokinetic modeling in the RFP	45

	Page
4.3 Linear GENE results	46
4.4 Nonlinear GENE results	49
4.5 Summary	54
5 Electron Density Fluctuations in RFP Plasmas	55
5.1 Density fluctuations in standard plasmas	56
5.2 Description of TEM-like density fluctuations in 200 kA PPCD plasmas	59
5.2.1 Equilibrium and fluctuating electron density characteristics	59
5.2.2 Wavenumber analysis	64
5.2.3 Residual magnetic fluctuations	67
5.3 Other plasma equilibria	71
5.3.1 400kA PPCD plasmas	72
5.3.2 Crash-heated 500kA PPCD	75
5.3.3 Medium-confinement 200kA PPCD	76
5.4 Measurement with the upgraded FIR system	77
5.5 Summary	79
6 Summary and Future Work	82
6.1 Density fluctuations	82
6.2 GENE Comparison	83
6.3 FIR upgrades	84
6.4 Conclusions	84
6.5 Future Work	85
LIST OF TABLES	v
LIST OF FIGURES	vi
ABSTRACT	xii
LIST OF REFERENCES	87
APPENDIX Spectral analysis	96
APPENDIX Other plots	111

DISCARD THIS PAGE

LIST OF TABLES

Table	Page
2.1 Name, impact parameter, toroidal angle, and chord length for each FIR chord. (Reproduced from Lanier, Ref. [44])	25

DISCARD THIS PAGE

LIST OF FIGURES

Figure	Page
1.1 Basic magnetic configuration of an RFP device. The toroidal and poloidal magnetic fields are comparable in magnitude, and the toroidal field reverses sign near the plasma edge. (Courtesy J.S. Sarff.)	3
1.2 Safety factor, q , in the RFP for an ensemble of PPCD discharges. The safety factor is less than 1.0 everywhere in the plasma, and decreases monotonically, changing sign at the reversal surface.	4
1.3 Basic layout of the PPCD circuit. (Reproduced from Chapman internal document, Ref. [29])	6
1.4 MST confinement relative to tokamak H-mode empirical scaling, assuming a tokamak with the same size, magnetic field strength, and heating power as the MST. (Reprinted from ITER Physics Guidelines, ITER report N 19 FDR 1 01-07-13 R 0.1.) [30]	7
1.5 Relative toroidal magnetic fluctuations in standard (<i>blue</i>) and improved confinement (<i>red</i>) plasmas. (Reproduced from Sarff et al., Ref. [31])	7
1.6 Simulated puncture plot of magnetic field in standard (<i>blue</i>) and improved confinement (<i>red</i>) plasmas. The field structure outside of the reversal surface is not captured in this figure, since only $0 < n < 33$ modes are plotted in this case. (Reproduced from several sources, Refs. [32, 4, 33])	8
1.7 Equilibrium electron density profile in standard (<i>black</i>) and PPCD (<i>red</i>) plasmas. (Reproduced from Lin et al., Ref. [34])	9
1.8 Equilibrium electron temperature profile in standard (<i>gray</i>) and PPCD (<i>black</i>) plasmas. (Reproduced from Sarff et al., Ref. [30])	10
1.9 Radial particle flux associated with $n=6$ tearing mode. (Reproduced from Lin et al., Ref. [34])	10

Figure	Page
1.10 Ion temperature profile in high current regular PPCD and crash-heated PPCD discharges. (Reproduced from Sarff et al., Ref. [30])	11
2.1 Simplified configuration of the 11 chord FIR interferometer-polarimeter system. (Reproduced from Parke, et. al, Ref. [45])	22
2.2 Cartoon of the three types of vibration a CO_2 molecule is subject to. (Reproduced from Lanier, Ref. [44])	23
2.3 Schematic of the 11 vertically viewing FIR chords separated into 2 sets, displaced 5° toroidally. (Reproduced from Lanier, Ref. [44])	24
2.4 (a) Corner-cube (and amplifier) and (b) VDI planar-diode (and amplifier) mixers designed for operation with 700 GHz source radiation. (Reproduced from Ding, et. al, Ref. [46])	28
2.5 Faraday-effect phase fluctuation frequency spectra for cases with (red) and without (black) plasma using (a) corner-cube mixer and (b) planar-diode mixer. Data are ensembled over 32 events during the time window 0.5-2.5 ms after sawtooth crash. (Reproduced from Ding, et. al, Ref. [46])	30
3.1 Rational surfaces permit tearing and reconnection of the magnetic field to occur, allowing islands to form. Magnetic islands degrade confinement by allowing rapid transport across the island's width. (Reproduced from Lanier, Ref. [44])	33
3.2 Heat transport conductivity χ_e compared to the stochastic heat transport conductivity in standard and PPCD plasmas. In areas of the plasma where the magnetic field is stochastic, the stochastic quantity adequately describes the heat transport. (Reproduced from Sarff, Ref. [33])	35
3.3 Physical mechanism for a drift wave. (Reproduced from Chen, Ref. [49])	37
4.1 Gyrocenter approximation used in gyrokinetic codes. (Reproduced from Garbet et al., Ref. [77])	42
4.2 Linear growth rates at several radial locations as computed in GENE, given a 200 kA PPCD equilibrium. (Reproduced from Carmody et al., Ref. [14])	47
4.3 Linear growth rates for TEM at $r/a = 0.8$ versus the inverse normalized density gradient scale length as computed in GENE. (Reproduced from Williams et al., Ref. [57])	47

Appendix	Page
Figure	
4.4 Linear growth rates for TEM at several radial locations versus the normalized wavenumber as computed in GENE. (Reproduced from Williams et al., Ref. [57])	48
4.5 Structure of the TEM in the RFP. The TEM has ballooning structure in Φ across a field aligned coordinate θ , which is dominantly poloidal in the region of interest. (courtesy Zach Williams)	49
4.6 Heat transport in simulated 200 kA PPCD plasmas with (<i>blue</i>) and without (<i>red</i>) an enforced magnetic perturbation on the scale of residual global magnetic tearing. (Reproduced from Williams et al., Ref. [57])	50
4.7 Electrostatic potential with and without enforced residual magnetic fluctuations. Without the ad hoc magnetic perturbations, zonal flows form sheets in the electrostatic potential that act as a transport barrier. With the magnetic perturbation, the zonal flows are “shorted out”, and become broader. (Reproduced from Williams et al., Ref. [57])	51
4.8 Linear growth rates (<i>blue</i>), nonlinear heat flux without an external B_r (<i>purple</i>), and nonlinear heat flux with an external B_r (<i>red</i>) for TEM at $r/a = 0.8$ versus the inverse normalized density gradient scale length as computed in GENE. (Reproduced from Williams et al., Ref. [57])	52
4.9 Puncture plot of magnetic fluctuations outside the reversal surface, as calculated by GENE. Overlapping magnetic islands can form outside the reversal surface, allowing for rapid radial transport. (courtesy Zach Williams)	53
5.1 Density fluctuation power spectrum as a function of time over an ensemble of 173 sawtooth crashes at 3 impact parameters: $x = 0.06$ m (a), $x = 0.21$ m (b), and $x = 0.43$ m (c)	57
5.2 Frequency-wavenumber power spectrum for the density fluctuations in the edge of standard plasmas for an ensemble of 173 sawteeth in 200 kA standard plasmas, taken 1 ms after the sawtooth crash.	58
5.3 Frequency power spectra for line-integrated electron density fluctuations in 200 kA Standard (<i>black</i>) and PPCD (<i>red</i>) plasma conditions. Density fluctuations are suppressed during PPCD, and a new spectral feature emerges. (Reproduced from Duff, et. al, Ref. [37])	60

Appendix Figure	Page
5.4 Evolution of (a) the line-integrated electron density fluctuation power at $x = 0.43$ m and (b) the equilibrium density gradient for an ensemble of PPCD plasmas taken from an Abel inversion of the FIR measured line-averaged density profile. The evolution of the inverse normalized density gradient scale length, $R_0 \langle \nabla n_e _{0.8} \rangle / \langle n_e \rangle_{0.8}$, for radius $r/a = 0.8$ is shown in (c). (Reproduced from Duff, et. al, Ref. [37])	62
5.5 Ensemble-average of Abel-inverted density profiles on mid-plane at 20 ms (<i>black</i>) and ensemble-averaged amplitude of line-integrated density fluctuations frequency integrated from 40-65 kHz (<i>red</i>). (Reproduced from Duff et. al, Ref. [37])	63
5.6 Line-integrated density fluctuation power, $\langle \tilde{n}_e^2 \rangle$, (40-60 kHz) measured at impact parameter $x = 0.43$ m versus $R_0 \langle \nabla n_e _{0.8} \rangle / \langle n_e \rangle_{0.8}$. (Reproduced from Duff, et. al, Ref. [37])	64
5.7 Frequency-wavenumber power spectrum of the line-integrated electron density fluctuations between FIR chords at $x = 0.36, 0.43$ m at 20 ms. Positive (negative) wavenumber corresponds to wave propagation in the ion (electron) diamagnetic drift direction. (Reproduced from Duff, et. al, Ref. [37])	65
5.8 Weighted mean of the spectral power for each available wavenumber. For the spectral power between wavenumbers ~ -0.15 to ~ -0.05 cm^{-1} , a linear fit can be used to estimate the group velocity of the emergent density fluctuation.	66
5.9 Frequency-wavenumber power spectrum of the line-integrated electron density fluctuations at between FIR chords at $x = 0.28, 0.43$ m at 20 ms.	67
5.10 Mode amplitude for demodulated magnetic spectrum in the poloidal ($1 \leq n \leq 15$) and toroidal ($1 \leq n \leq 31$) directions for fluctuations resonant inside the reversal surface for an ensemble of 142 comparable 200 kA PPCD plasma discharges. During PPCD, the magnetic fluctuations are suppressed, and the $n=6$ mode dominates both spectra.	69
5.11 Mode amplitude for demodulated magnetic spectrum in the poloidal ($1 \leq n \leq 15$) and toroidal ($1 \leq n \leq 31$) directions for fluctuations resonant outside the reversal surface for an ensemble of 142 comparable 200 kA PPCD plasma discharges. The spectrum has a local peak at $n=8$, and is dominated by low n modes.	70
5.12 Profiles for the linear magnetic fluctuation eigenfunctions associated with the $m = 1, n = 10$ tearing mode, evaluated using RESTER. (Courtesy John Sarff)	71

Figure	Page
5.13 Evolution of (a) the line-integrated electron density fluctuation power at $x = 0.36$ m and (b) the equilibrium density gradient for an ensemble of 400 kA PPCD plasmas. The evolution of the inverse normalized density gradient scale length, $R_0 \langle \nabla n_e _{0.75} \rangle / \langle \bar{n}_e \rangle_{0.75}$, for radius $r/a = 0.75$ is shown in (c).	73
5.14 Ensemble-average of Abel-inverted density profiles on mid-plane at 20 ms (<i>black</i>) and ensemble-averaged amplitude of line-integrated density fluctuations frequency integrated from 65-100 kHz (<i>red</i>).	74
5.15 Frequency-wavenumber power spectrum of the line-integrated electron density fluctuations at $x = 0.36, 0.43$ m during PPCD in 400 kA plasmas. Positive (negative) wavenumber corresponds to wave propagation in the ion (electron) diamagnetic drift direction.	75
5.16 Frequency-wavenumber power spectrum of the line-integrated electron density fluctuations at $x = 0.36$ m during PPCD in 500 kA crash heated plasmas. Positive (negative) wavenumber corresponds to wave propagation in the ion (electron) diamagnetic drift direction.	76
5.17 Density fluctuation power spectrum for an ensemble of medium confinement 200 kA PPCD plasmas. A second emergent fluctuation appears in this plasma equilibrium, implying the presence of a second, sub-dominant drift wave instability.	78
5.18 Frequency-wavenumber power spectrum of the line-integrated electron density fluctuations at $x = 0.36, 43$ m during PPCD in medium confinement 200 kA PPCD plasmas at $t = 20 - 21$ ms. Positive (negative) wavenumber corresponds to wave propagation in the ion (electron) diamagnetic drift direction.	78
5.19 Photograph of planar diode mixer in mixer tube (left) and two mixer array for high wavenumber measurement experiments (right).	79
5.20 Frequency-wavenumber power spectrum of the line-integrated electron density fluctuations for high wavenumber measurement, with both mixers located at an impact parameter of $x = 0.43$ m.	80
 Appendix	
Figure	
B.1 Frequency-wavenumber power spectrum of the line-integrated electron density fluctuations between chords at impact parameters of (a) $R - R_0 = 36, 43$ cm and (b) $R - R_0 = 36, 28$ cm.	113

Figure	Page
B.2 Frequency-wavenumber power spectrum of the line-integrated electron density fluctuations between chords at impact parameters of (a) $R - R_0 = 21, 28\text{cm}$ and (b) $R - R_0 = 21, 13\text{cm}$	114
B.3 Frequency-wavenumber power spectrum of the line-integrated electron density fluctuations between chords at impact parameters of (a) $R - R_0 = 6, 13\text{cm}$ and (b) $R - R_0 = 6, -2\text{cm}$	115
B.4 Frequency-wavenumber power spectrum of the line-integrated electron density fluctuations between chords at impact parameters of (a) $R - R_0 = -9, -2\text{cm}$ and (b) $R - R_0 = -9, -17\text{cm}$	116
B.5 Frequency-wavenumber power spectrum of the line-integrated electron density fluctuations between chords at impact parameters of (a) $R - R_0 = -24, -17\text{cm}$ and (b) $R - R_0 = -24, -32\text{cm}$	117

ABSTRACT

This is a dissertation for the completion of a Doctorate of Philosophy in Physics degree granted at the University of Wisconsin-Madison.

Density fluctuations in the large-density-gradient region of improved confinement Madison Symmetric Torus (MST) RFP plasmas exhibit multiple features that are characteristic of the trapped-electron mode (TEM). In fusion relevant plasmas, thermal transport is a key avenue of research in order to achieve a burning plasma. In the reversed field pinch (RFP) magnetic geometry, the dynamics of conventional plasma discharges are primarily governed by magnetic stochasticity stemming from multiple long-wavelength tearing modes, that sustain the RFP discharge but have an adverse effect on the plasma confinement. Using inductive current profile control, these tearing modes are reduced, and global confinement is increased to that expected for comparable tokamak plasma. Under these conditions with certain plasma equilibria, new short-wavelength fluctuations distinct from global tearing modes appear in the spectrum at frequencies $f \sim 50$ kHz that have normalized perpendicular wavenumbers $k_{\perp}\rho_s \lesssim 0.2$, and propagate in the electron diamagnetic drift direction. By adjusting the plasma current or the inductive suppression, there are observable variations in the spectral features. They exhibit a critical-gradient threshold, and the fluctuation amplitude increases with a local density gradient dependent parameter. These characteristics are consistent with the predictions of unstable TEMs based on gyrokinetic analysis using the GENE code. This thesis represents the first observation and description of TEM-like instabilities in the RFP geometry.

Chapter 1

Introduction

The confinement of energy, particles, and momentum in a toroidal magnetic confinement fusion reactor plasma is anticipated to be limited by plasma turbulence. In present-day tokamak and stellarator plasmas, microturbulence associated with a variety of drift waves on scales close to the poloidal gyro-radius are most often thought to be responsible for turbulent transport [1, 2]. Larger-scale fluctuations can degrade confinement as well, for example, in conventional reversed-field pinch (RFP) plasmas, multiple tearing modes arise with overlapping magnetic islands that cause the magnetic field to become stochastic over a large volume of the plasma. Parallel streaming becomes a potent transport mechanism in this case [3, 4, 5, 6]. Stochastic transport is also important in microturbulence [7]. Understanding and controlling turbulent transport remains a central goal for magnetic confinement fusion research, and examining the behavior of these processes in different magnetic configurations offers an effective way to develop predictive models that are robust over a wide range of plasma parameters and magnetic configuration variables.

While conventional RFP plasmas suffer from global magnetic tearing instability, inductive current profile control yields a ten-fold improvement in the global energy confinement by suppressing large magnetic fluctuations associated with tearing modes [8, 9, 10]. Improved confinement is also obtained in self-organizing RFP plasmas through a spontaneous transition to the quasi-single-helicity regime in which one tearing mode is dominant and secondary tearing modes are reduced [11]. Once tearing is sufficiently suppressed, microturbulence could limit confinement in the RFP as it does in tokamak and stellarator plasmas. Recent gyrokinetic modeling reveals drift-wave instability for the RFP configuration, with some properties distinct from those seen in tokamak and stellarator configurations [12, 13, 14]. The critical-gradient threshold for instability is larger in the

RFP by a factor of the the aspect ratio, a feature associated with the lower safety factor and larger poloidal magnetic curvature. Zonal flows are also predicted to be much stronger and the nonlinear up-shift for the critical gradient (Dimits Shift) yields predictions for relatively lower transport due to saturated turbulence. However, residual magnetic fluctuations are able to severely reduce zonal flow amplitudes [15, 16], which increases the transport to values typical for tokamak plasmas [14].

The primary physics findings of this thesis are the measurement and description of a density-gradient-driven trapped-electron mode in the MST using a far infrared interferometer/polarimeter system, as well as a comparison of this measurement to gyrokinetic simulations in MST-like equilibria. By using an inductive profile control technique to suppress tearing instability and increase pressure gradients, the tearing instability becomes sub-dominant in the density fluctuation spectrum, as measured by the interferometer system, and an emergent density fluctuation is measured. This density fluctuation is found to be highly dependent on the local electron density gradient, travel in the electron diamagnetic direction, and has a frequency and wavenumber consistent with a trapped electron mode instability. Gyrokinetic simulations using the GENE [17] code predict unstable trapped electron mode turbulence in the large gradient region of the experimental equilibria. The comparison of experimental and simulation results leads to the expectation that the density fluctuation observed experimentally is related to trapped electron mode turbulence. To show these results, the thesis is organized as follows. First, the MST device will be introduced, including standard plasma operation, the method of improving confinement using an inductive current profile control technique called pulsed parallel current drive (PPCD), and a brief overview of the magnetics array in Chapter 1. Then, the FIR interferometer-polarimeter system will be introduced in Chapter 2, including the theoretical basis of the system, technical aspects, basic operation, and the recent system upgrade. This will be followed by a brief overview of plasma transport in the RFP in Chapter 3, and computational results from the gyrokinetic code GENE from several plasma equilibria in linear and nonlinear regimes in Chapter 4. Then, a thorough analysis of density fluctuations in standard and improved confinement plasmas will be presented in Chapter 5, going through frequency, wavenumber, and power analysis, as well as analysis of the magnetic features,

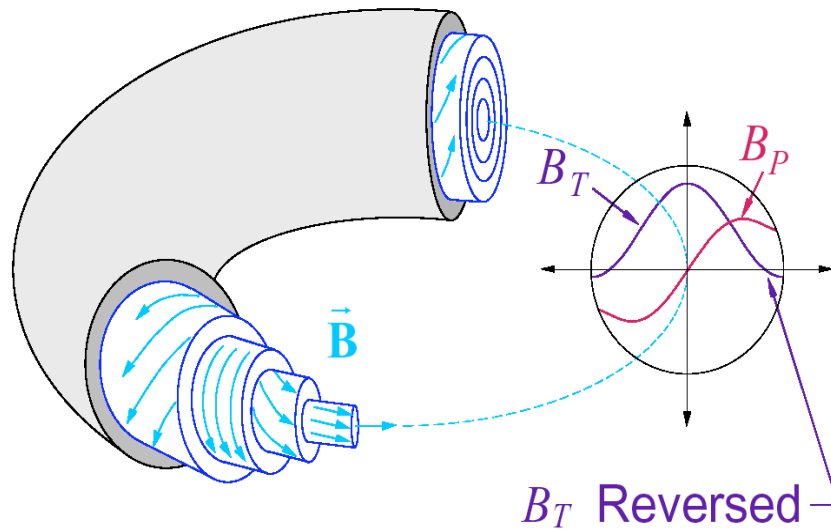


Figure 1.1 Basic magnetic configuration of an RFP device. The toroidal and poloidal magnetic fields are comparable in magnitude, and the toroidal field reverses sign near the plasma edge. (Courtesy J.S. Sarff.)

and a comparison of the GENE and experimental results. Finally, The work will be summarized in Chapter 6, and there will be a discussion of potential future work.

1.1 The reversed-field pinch

The reversed field pinch (RFP) is a toroidally axisymmetric plasma where the toroidal and poloidal magnetic field (B_ϕ and B_θ , respectively) are comparable in magnitude and the toroidal magnetic field reverses sign near the plasma edge, at a point called the reversal surface. This configuration is shown in Figure 1.1. A parallel current gradient can drive an MHD relaxation event called a sawtooth crash that flattens the parallel current profile. This relaxation process is responsible for the sustainment of the toroidal magnetic field, but degrades particle and energy confinement of the plasma [18].

The RFP preferred state was derived by Taylor in 1974 [18], based on the conjecture that the magnetic helicity K was conserved over the whole volume of the plasma:

$$\frac{d}{dt}K_0 = \frac{d}{dt} \int_V \vec{A} \cdot \vec{B} dV \approx 0. \quad (1.1)$$

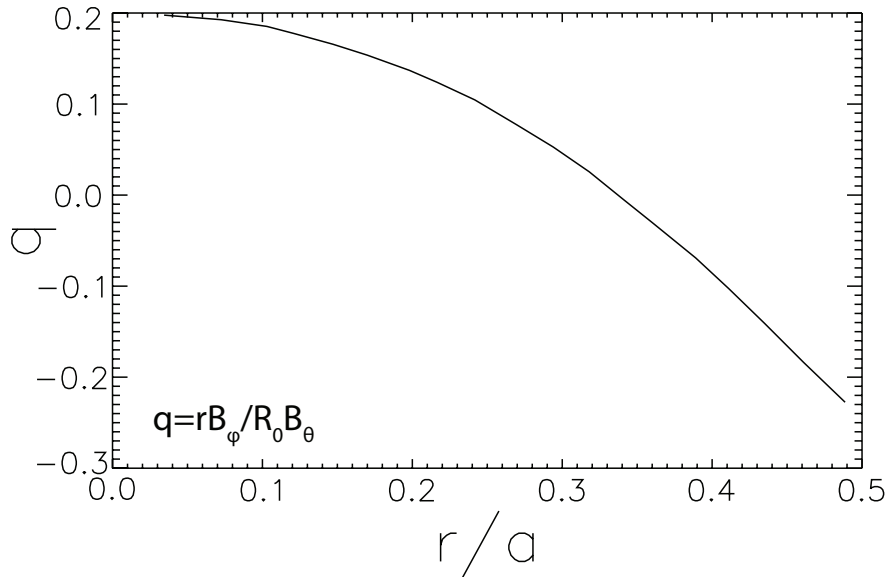


Figure 1.2 Safety factor, q , in the RFP for an ensemble of PPCD discharges. The safety factor is less than 1.0 everywhere in the plasma, and decreases monotonically, changing sign at the reversal surface.

Minimizing the magnetic energy of the plasma with respect to K_0 led Taylor to the preferred state of the magnetic field, described by:

$$\nabla \times \vec{B} = \lambda \vec{B}, \quad (1.2)$$

where λ is a constant. Equation 1.2 describes the RFP minimum energy state for a weakly diffusive plasma [18].

The dynamo has been studied exhaustively, with various studies attempting to describe the mechanisms of the process. This includes studies looking at the correlated cross product between magnetic and velocity fluctuations using spectroscopic diagnostics [19, 20] and Langmuir probe measurements [21] to show that $\langle \langle \tilde{v} \times \tilde{b} \rangle \rangle$ is sufficient to balance parallel Ohm's law in the RFP and sustain the discharge. More recently, Ding, et. al [22] used a polarimetry measurement, and Tharp, et. al [23] and Triana [24] used probe measurements to study MHD and hall dynamo effects.

Magnetic fluctuations that contribute to the dynamo result from resistive tearing modes that occur in the plasma. In the RFP, the relatively small toroidal magnetic field results in a safety factor, $q = \frac{aB_\phi}{R_0 B_\theta}$, that is less than one throughout the plasma, and decreases monotonically through the plasma. The safety factor changes sign at a point called the reversal surface, as seen in Figure

1.2. Consequently, the RFP has many closely spaced resonant surfaces where q is rational, i.e.:

$$q = \frac{m}{n}, \quad (1.3)$$

where m and n are integers. At these rational surfaces, magnetic tearing and reconnection can take place, allowing for magnetic islands. The effects of these islands will be expanded on in Chapter 3.

The experiments used in this thesis were performed on the Madison Symmetric Torus (MST) [25], an RFP based at the University of Wisconsin - Madison. It is a moderate sized toroidal plasma device with a major radius of 1.5 m and a minor radius of 0.52 m. The MST is able to operate under a wide array of plasma parameters. The plasma current is $I_p \leq 600$ kA. Plasma electron temperatures are $T_e \leq 2$ keV. Plasma densities in the core are around $n_e \sim 10^{19} \frac{\text{particles}}{\text{m}^3}$. The data in this thesis will be from plasma discharges with $I_p \sim 200 - 500$ kA, $n_e \sim 0.8 \cdot 10^{19} \text{ m}^{-3}$, and core $T_e \sim 800 - 1200$ eV.

1.2 Improving confinement

The RFP concept has some unique benefits that may make it desirable as a fusion device [26]. These benefits are primarily due to the concentration of the magnetic field within the plasma and relatively small applied toroidal field. Due to the small magnetic field at the magnets, copper can be used instead of the superconducting materials that may be required for some other fusion concepts. Additionally, because an RFP reactor can theoretically be ohmically driven to ignition, no plasma-facing auxiliary heating elements are required and would not need to be periodically replaced due to wear. In order to take advantage of these benefits, magnetic fluctuations must be suppressed to improve confinement [26].

Magnetic fluctuations, which dominate transport in standard RFP plasma operation, are a result of the plasma attempting to relax into a state of lower energy. Using an inductive current profile control technique, called pulsed poloidal current drive (PPCD), these magnetic fluctuations can be suppressed and other processes may become important to transport. The tearing mode arises from gradients in the parallel current profile J_{\parallel}/B , and degrade confinement while flattening the

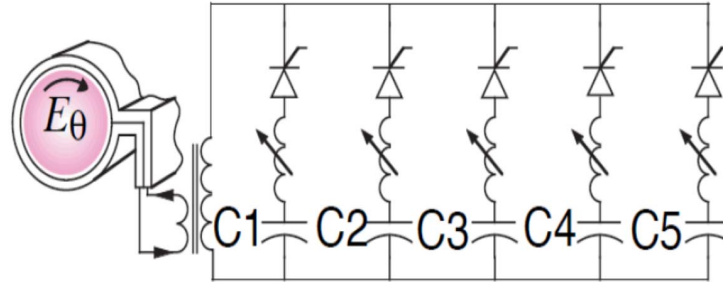


Figure 1.3 Basic layout of the PPCD circuit. (Reproduced from Chapman internal document, Ref. [29])

parallel current gradient. PPCD works to flatten this gradient to the same degree as a sawtooth crash applying a poloidal current in the wall, which reduces the magnetic flux in the plasma over time, inducing a parallel current in the edge of the plasma that flattens the parallel current profile [27, 28]. PPCD mitigates $v \times B$ fluctuations and reduces the available free energy for global magnetic tearing modes.

The circuit used for PPCD operation, seen in Figure 1.3, is fairly simple. Current is driven poloidally in the conducting shell, adjusting the toroidal magnetic field. From Faraday's law, $\nabla \times \vec{E} = -\partial \vec{B} / \partial t$, the change in toroidal magnetic field results in a poloidal electric field that drives poloidal current. Since the field in the edge is primarily poloidal, the driven current is parallel to the magnetic field, and this reduces the parallel current density gradient.

As a result of PPCD, confinement improves to tokamak-like levels [8], as seen in Figure 1.4. Additionally, toroidal magnetic fluctuations are reduced by an order 5 – 10 throughout the toroidal mode number spectrum, as seen in Figure 1.5, compared to standard plasmas. However there are still residual magnetic fluctuations, particularly at mode numbers $n = 6 - 7$, which are still prominent in the mode number spectrum. Using a field line tracing code to simulate the magnetic field for these magnetic fluctuations can reveal how stochastic the field is. Standard plasmas are expected to have fairly high stochasticity due to overlapping magnetic islands, as seen in Figure 1.6. For PPCD plasmas, the magnetic stochasticity is found to be significantly lower in the core, but is still a significant feature elsewhere in the plasma.

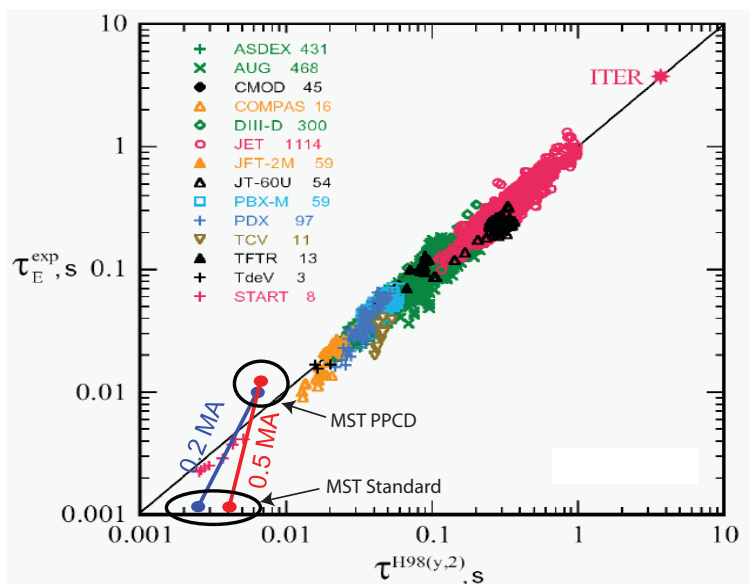


Figure 1.4 MST confinement relative to tokamak H-mode empirical scaling, assuming a tokamak with the same size, magnetic field strength, and heating power as the MST. (Reprinted from ITER Physics Guidelines, ITER report N 19 FDR 1 01-07-13 R 0.1.) [30]

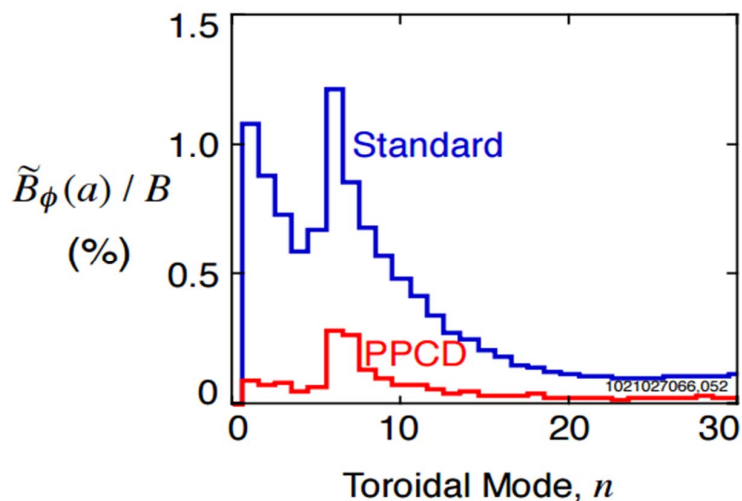


Figure 1.5 Relative toroidal magnetic fluctuations in standard (*blue*) and improved confinement (*red*) plasmas. (Reproduced from Sarff et al., Ref. [31])

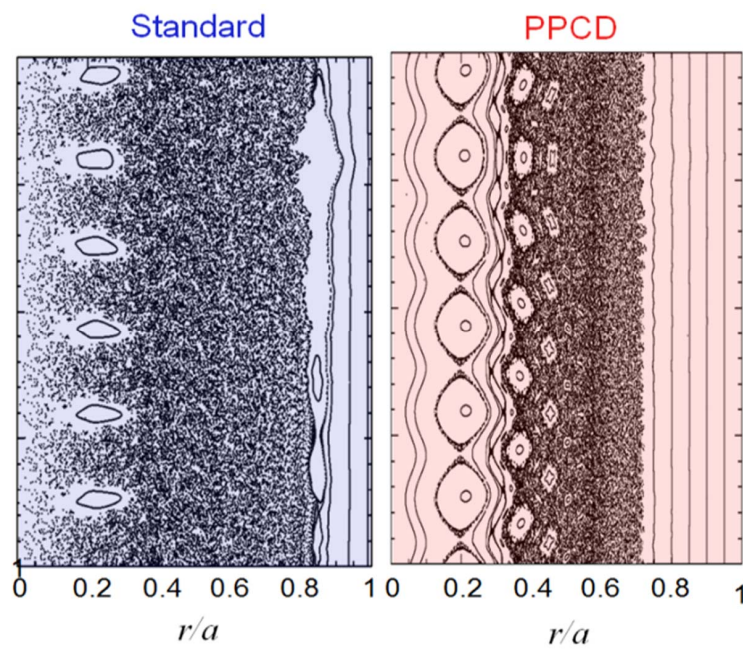


Figure 1.6 Simulated puncture plot of magnetic field in standard (*blue*) and improved confinement (*red*) plasmas. The field structure outside of the reversal surface is not captured in this figure, since only $0 < n < 33$ modes are plotted in this case. (Reproduced from several sources, Refs. [32, 4, 33])

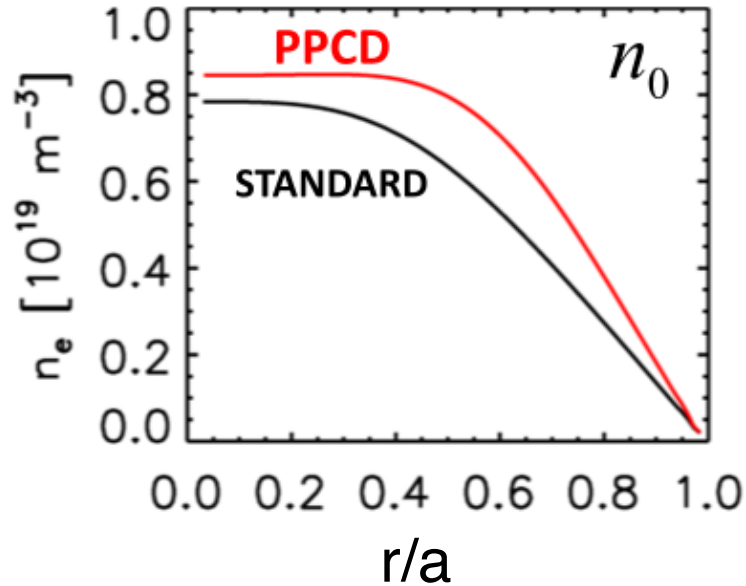


Figure 1.7 Equilibrium electron density profile in standard (*black*) and PPCD (*red*) plasmas. (Reproduced from Lin et al., Ref. [34])

PPCD has a significant impact on the equilibrium and fluctuating parameters of the plasma. The electron density flattens in the core, and the electron density gradient steepens in the edge, as seen in Figure 1.7. Due to the increase in confinement, the electron temperature also increases significantly, by up to a factor of ~ 3 , as seen in Figure 1.8. The electron temperature gradient reaches into the core of the plasma, significantly further than in standard plasmas. The radial particle flux associated with the $m=1, n=6$ tearing mode, plotted in Figure 1.9, drops significantly in most of the plasma. The drastic increase in the electron temperature does not hold for the ion temperature, as seen in Figure 1.10, where the core ion temperature only reaches $\sim 300\text{eV}$ during the PPCD cycle. The ions do not have a mechanism for heating under normal PPCD operation, but a method called crash-heating, where a magnetic tearing relaxation event is triggered immediately before PPCD, has been found to increase the ion temperature during PPCD significantly, up to $T_i \sim 2\text{ keV}$ [10].

Density fluctuations in these plasmas have been somewhat explored in previous work, but no exhaustive studies have been done. The previous studies were primarily concerned with the effects of PPCD on the tearing modes, but generally ignored high frequency fluctuations [35]. More recent

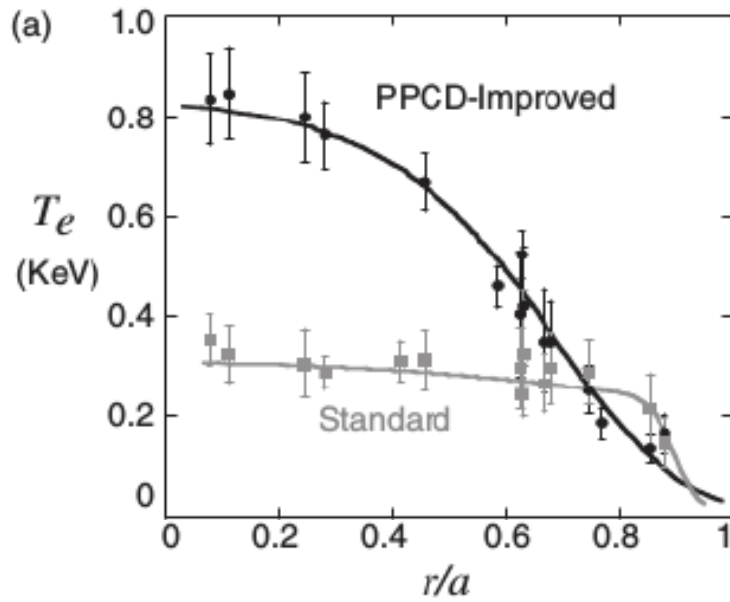


Figure 1.8 Equilibrium electron temperature profile in standard (*gray*) and PPCD (*black*) plasmas. (Reproduced from Sarff et al., Ref. [30])

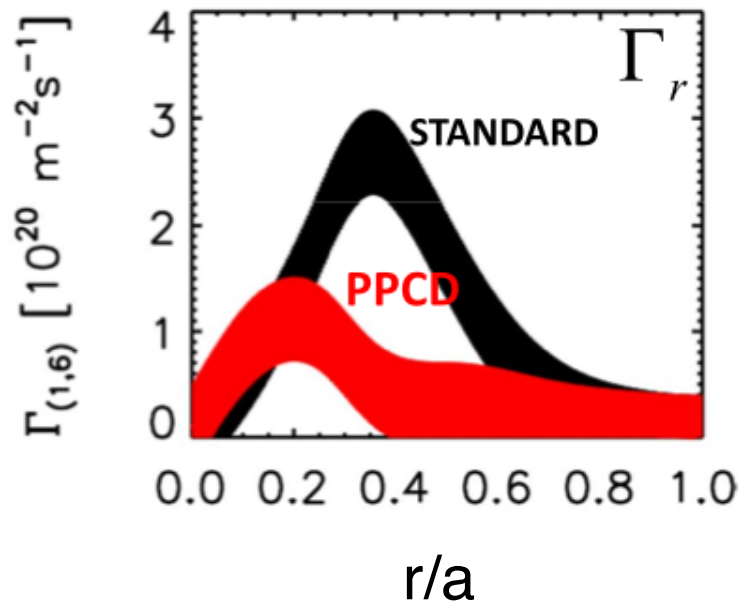


Figure 1.9 Radial particle flux associated with $n=6$ tearing mode. (Reproduced from Lin et al., Ref. [34])

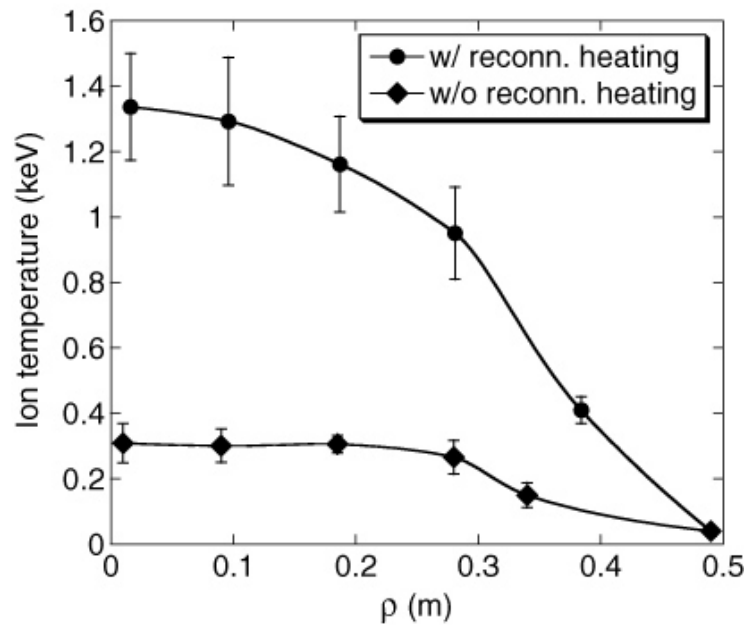


Figure 1.10 Ion temperature profile in high current regular PPCD and crash-heated PPCD discharges. (Reproduced from Sarff et al., Ref. [30])

analysis [36, 37] has explored higher frequency density fluctuations not associated with the global magnetic tearing mode, and will be the primary topic of this thesis.

1.3 Magnetics on the MST

The MST has magnetic coil arrays in the poloidal and toroidal directions. Each coil set contains two or three orthogonally facing coils, depending on the array, that measure the magnetic field at the wall in the poloidal, toroidal, and radial directions. These coils are mounted on the inside surface of the MST wall and are contained in ceramic heat shields. The toroidal magnetic array is made up of 64 evenly spaced magnetic coil sets at 241° poloidal with coils facing in three orthogonal directions. The poloidal array is made up of 32 evenly spaced magnetic coil sets at 180° toroidal with two orthogonally facing coils in the radial and poloidal directions. The signal from the magnetic arrays can be Fourier decomposed into components of the global magnetic tearing modes, which is routinely done for all MST discharges. For each mode number, up to the Nyquist limit of the array, the amplitude, phase, and phase velocity are stored in the MST database. Further processing of the magnetics data can decompose each mode into stationary, positive, and negative rotating components, which can prove useful for estimating the magnetic mode amplitude outside the reversal surface of the plasmas [38, 39].

1.4 Other diagnostics

While the data in this thesis was primarily compiled using the FIR interferometer/polarimeter diagnostic described in Chapter 2, several other diagnostics and analysis codes were useful for this research. Namely, the Thomson scattering system, and the MSTFit equilibrium reconstruction code were used for some of the data in this thesis.

Local electron temperature measurements can be made on the MST using a multi-point Thomson scattering diagnostic. Thomson scattering is the absorption of a photon and subsequent emission of a different photon by a free, charged particle. For the data used in this thesis, the Thomson scattering laser system was run at a repetition rate of 2kHz, had temperature sensitivity 10eV to

5keV, and radial extent $r/a \leq 0.8$. Further information about this system can be found in references [40, 41, 42].

MSTFit is a non-linear Grad-Shafranov toroidal equilibrium reconstruction code developed for the MST [43]. Utilizing the variety of diagnostics available on the MST, MSTFit can accurately resolve subtle changes in internal structures with implications for MHD stability. It does this by computing an axisymmetric solution of Maxwell's equations while satisfying radial force balance ($\vec{J} \times \vec{B} = \nabla P$). In this thesis, MSTFit has been used to calculate local parameters that can influence drift wave stability, such as pressure gradient scale lengths, safety factor, and magnitude of the magnetic field.

1.5 Summary

The MST RFP is a moderate sized plasma fusion experiment that is typified by its magnetic geometry and large-scale global magnetic tearing modes dominating the thermal transport characteristics. The global magnetic tearing modes help sustain the RFP discharge, but have a deleterious effect on the plasma confinement characteristics. By inductively applying a current in the edge of the plasma via PPCD, the global magnetic tearing modes can be suppressed, and other smaller scale instabilities may become important to thermal transport. The MST is a well diagnosed plasma, and many diagnostics, including the far-infrared interferometer-polarimeter system (described in Chapter 2), Thomson scattering system, and edge magnetics can be used to describe the dynamics of the improved confinement plasmas.

Chapter 2

FIR

The far-infrared (FIR) laser interferometer-polarimeter diagnostic is a high time response, multi-chord system used to measure plasma parameters that influence the index of refraction of the plasma. This includes the line-integrated electron density (n_e) and the magnetic field parallel to the laser path (B_z). These measurements are taken across the full diameter of the plasma and can be used to infer parameters like the equilibrium electron density, the fluctuating electron density, the electron density gradient, and the plasma current. This diagnostic was built by and is maintained in collaboration with the University of California at Los Angeles [44]. This chapter will include details on the theory behind the diagnostic in Section 2.1 for the interferometer and Section 2.2 for the polarimeter, both of which have been derived using the method in “Principles of Plasma Diagnostics” by Hutchinson [41]. This is followed by a detailed description of the physical FIR system in Section 2.3, and a description of the recent FIR mixer upgrades in Section 2.4.

2.1 Interferometry theory

For electromagnetic waves (such as a laser) in a plasma, the plasma can be treated as a continuous medium in which a current can flow, and is governed by Maxwell’s equations in a vacuum [41]. The important Maxwell’s equations for this formulation are:

$$\nabla \times \vec{E} = -\frac{\partial \vec{B}}{\partial t}, \quad (2.1)$$

and

$$\nabla \times \vec{B} = \mu_0 \vec{j} + \epsilon_0 \mu_0 \frac{\partial \vec{E}}{\partial t}, \quad (2.2)$$

where \vec{E} is the electric field, \vec{B} is the magnetic field, ϵ_0 and μ_0 are the permittivity and permeability of free space, and the electromagnetic qualities of the plasma are contained in the current \vec{j} . By taking the curl of Equation 2.1 and the time derivative of Equation 2.2, \vec{B} can be eliminated to obtain

$$\nabla \times (\nabla \times \vec{E}) + \frac{\partial}{\partial t}(\mu_0 \vec{j} + \epsilon_0 \mu_0 \frac{\partial \vec{E}}{\partial t}) = 0. \quad (2.3)$$

The plasma is assumed to be relatively homogeneous in space in time. This allows for Fourier analysis of the fields and currents such that:

$$\vec{E}(x, t) = \int \vec{E}(\vec{k}, \omega) e^{i(\vec{k} \cdot \vec{x} - \omega t)} \frac{d^3 \vec{k}}{(2\pi)^3} \frac{d\omega}{2\pi}, \quad (2.4)$$

where \vec{k} is the wavenumber and ω is the angular frequency. Therefore each field quantity can be linearized such that:

$$\frac{\partial \vec{E}}{\partial t} = -i\omega \vec{E}, \quad (2.5)$$

$$\nabla \times \vec{E} = i\vec{k} \times \vec{E}. \quad (2.6)$$

Ohm's law is, for each Fourier mode:

$$\vec{j}(\vec{k}, \omega) = \vec{\sigma}(\vec{k}, \omega) \bullet \vec{E}(\vec{k}, \omega), \quad (2.7)$$

where $\vec{\sigma}$ is the conductivity of the plasma. In general, a plasma may be an anisotropic medium so that $\vec{\sigma}$ is a tensor conductivity.

For a single Fourier mode, Equation 2.3 becomes:

$$\vec{k} \times (\vec{k} \times \vec{E}) + i\omega(\mu_0 \vec{\sigma} \bullet \vec{E} - \epsilon_0 \mu_0 i\omega \vec{E}) = 0, \quad (2.8)$$

which can be written:

$$(\vec{k} \vec{k} - k^2 \bar{1} + \frac{\omega^2}{c^2} \bar{\epsilon}) \bullet \vec{E} = 0, \quad (2.9)$$

where $\bar{1}$ is the unit tensor and $\bar{\epsilon}$ is the dielectric tensor

$$\bar{\epsilon} = (\bar{1} + \frac{i}{\omega \epsilon_0} \vec{\sigma}). \quad (2.10)$$

Equation 2.9 is three simultaneous equations for the components of the vector \vec{E} . For this equation to have a nonzero solution, then the determinant:

$$\det(\vec{k} \vec{k} - k^2 \bar{1} + \frac{\omega^2}{c^2} \bar{\epsilon}) = 0, \quad (2.11)$$

must be true. This equation represents the dispersion relation for waves in this framework.

The simplest case in this framework is:

$$\bar{\sigma} = \sigma \bar{1}, \quad (2.12)$$

$$\bar{\epsilon} = \epsilon \bar{1}, \quad (2.13)$$

where the plasma medium is isotropic. The waves separate into two cases: electric field polarization perpendicular to the electromagnetic wave ($\vec{k} \bullet \vec{E} = 0$), and electric field polarization parallel to the electromagnetic wave ($\vec{k} \times \vec{E} = 0$). For a wave traveling along the \hat{z} direction, the expression in the determinant of Equation 2.11 can be written expressly as the matrix:

$$\vec{k} \vec{k} - k^2 \bar{1} + \frac{\omega^2}{c^2} \bar{\epsilon} = \begin{bmatrix} -k^2 + \frac{\omega^2}{c^2} \epsilon & 0 & 0 \\ 0 & -k^2 + \frac{\omega^2}{c^2} \epsilon & 0 \\ 0 & 0 & \frac{\omega^2}{c^2} \epsilon \end{bmatrix}, \quad (2.14)$$

for which Equation 2.11 holds if:

$$-k^2 + \frac{\omega^2}{c^2} \epsilon = 0, \quad \text{if } \vec{E} \text{ perpendicular}, \quad (2.15)$$

or

$$\frac{\omega^2}{c^2} \epsilon = 0, \quad \text{if } \vec{E} \text{ parallel}. \quad (2.16)$$

The perpendicular wave dispersion relation is a standard expression for dispersion in a uniform dielectric medium. The parallel wave dispersion relation is just $\epsilon = 0$. This becomes more interesting when $\bar{\epsilon}$ is not isotropic and the wave cannot be divided easily into transverse and longitudinal parts, as the electric field is generally both, and the matrix in Equation 2.14 will have non-zero off-diagonal terms.

A relatively simple treatment of the plasma conductivity in a cold plasma approximation can provide insight into the behavior of electromagnetic waves in a plasma. The electrons are considered stationary except for motion due to electric fields. For a single electron, the equation of motion is:

$$m_e \frac{\partial \vec{v}}{\partial t} = -e(\vec{E} + \vec{v} \times \vec{B}_0), \quad (2.17)$$

where m_e is the electron mass, e is the fundamental charge, \vec{v} is the particle velocity, the magnetic field \vec{B}_0 is static, and collisions are ignored. For a cold plasma, a single Fourier mode in \vec{v} is purely harmonic such that $\vec{v} \propto e^{-i\omega t}$. For coordinates aligned to the magnetic field, $\vec{B}_0 = B_0 \hat{z}$, the components of the equation of motion for an electron are:

$$-m_e i\omega v_x = -eE_x - eB_0 v_y, \quad (2.18)$$

$$-m_e i\omega v_y = -eE_y + eB_0 v_x, \quad (2.19)$$

$$-m_e i\omega v_z = -eE_z, \quad (2.20)$$

which can be solved for v in terms of E :

$$v_x = \frac{-ie}{\omega m_e} \frac{1}{1 - \Omega^2/\omega^2} (E_x - i\frac{\Omega}{\omega} E_y), \quad (2.21)$$

$$v_y = \frac{-ie}{\omega m_e} \frac{1}{1 - \Omega^2/\omega^2} (E_y + i\frac{\Omega}{\omega} E_x), \quad (2.22)$$

$$v_z = \frac{-ie}{\omega m_e} E_z, \quad (2.23)$$

where $\Omega \equiv eB_0/m_e$ is the electron cyclotron frequency. Since all electrons move the same way in the cold plasma approximation, the current density is:

$$\vec{j} = -en_e \vec{v} = \vec{\sigma} \bullet \vec{E}, \quad (2.24)$$

where the conductivity tensor is:

$$\vec{\sigma} = \frac{in_e e^2}{m_e \omega} \frac{1}{1 - \Omega^2/\omega^2} \begin{bmatrix} 1 & -i\Omega/\omega & 0 \\ i\Omega/\omega & 1 & 0 \\ 0 & 0 & 1 - \Omega^2/\omega^2 \end{bmatrix}. \quad (2.25)$$

While this is only for the electrons, the ions are significantly more massive than the electrons, such that the ion contribution is small and can generally be ignored, provided the frequency is high enough.

The dielectric tensor $\bar{\epsilon}$ can be found using Equation 2.10:

$$\bar{\epsilon} = \begin{bmatrix} 1 - \frac{\omega_p^2}{\omega^2 - \Omega^2} & \frac{i\omega_p^2\Omega^2}{\omega(\omega^2 - \Omega^2)} & 0 \\ \frac{-i\omega_p^2\Omega^2}{\omega(\omega^2 - \Omega^2)} & 1 - \frac{\omega_p^2}{\omega^2 - \Omega^2} & 0 \\ 0 & 0 & 1 - \frac{\omega_p^2}{\omega^2} \end{bmatrix}, \quad (2.26)$$

where $\omega_p^2 = n_e e^2 / \epsilon_0 m_e$ is the electron plasma frequency. To make the equations simpler, the variables X and Y are introduced such that:

$$X = \frac{\omega_p^2}{\omega^2}, \quad (2.27)$$

$$Y = \frac{\Omega}{\omega}. \quad (2.28)$$

The axes are chosen such that $\vec{k} = k(0\hat{x}, \sin(\theta)\hat{y}, \cos(\theta)\hat{z})$, where θ is the angle between \vec{k} and \vec{B}_0 . The determinant equation then becomes

$$\det \begin{bmatrix} -N^2 + 1 - \frac{X}{1-Y^2} & \frac{iXY}{1-Y^2} & 0 \\ \frac{-iXY}{1-Y^2} & -N^2 \cos^2(\theta) + 1 - \frac{X}{1-Y^2} & N^2 \sin(\theta) \cos(\theta) \\ 0 & N^2 \sin(\theta) \cos(\theta) & -N^2 \sin^2(\theta) + 1 - X \end{bmatrix} = 0, \quad (2.29)$$

which represents a quadratic equation in N , the index of refraction of the plasma. The solutions are generally written in the form:

$$N^2 = 1 - \frac{X(1-X)}{1-X - \frac{1}{2}Y^2 \sin^2(\theta) \pm [(\frac{1}{2}Y^2 \sin^2 \theta)^2 + (1-X)^2 Y^2 \cos^2 \theta]^{\frac{1}{2}}}, \quad (2.30)$$

which is the Appleton-Hartree formula [41] for the refractive index of a cold plasma, where $\bar{\epsilon}$ is independent of \vec{k} .

For an electromagnetic wave propagating in a plasma device, θ can vary continuously, so a rigorous solution can be difficult to obtain. In order to simplify this result, there are two special cases that can be considered: when the wave is parallel ($\theta = 0$) or perpendicular ($\theta = \pi/2$) to the

background magnetic field. When the wave propagates parallel to the magnetic field ($\vec{k} \parallel \vec{B}$), the index of refraction becomes

$$N^2 = 1 - \frac{X}{1 - Y^2} \pm \frac{XY}{1 - Y^2} = 1 - \frac{X}{1 \pm Y}. \quad (2.31)$$

When the wave propagates perpendicular to the magnetic field ($\vec{k} \perp \vec{B}$) the index of refraction becomes:

$$N^2 = 1 - X, \quad \text{or} \quad N^2 = 1 - \frac{X(1 - X)}{1 - X - Y^2}. \quad (2.32)$$

The parameters $X (= \omega_p^2/\omega^2)$ and $Y (= \Omega/\omega)$ depend on only the electron density n_e and equilibrium magnetic field (B_0) respectively. This allows the refractive index to be used as a measure for these parameters with excellent confidence.

If the magnetic field is small, such that the cyclotron frequency is sufficiently smaller than the wave frequency, then $Y \rightarrow 0$, and the index of refraction becomes:

$$N^2 \approx 1 - X, \quad (2.33)$$

for all angles of the wavenumber relative to the background magnetic field. This simplification allows for the difference in the index of refraction of the plasma and of the air to be measured in such a way as to provide a measure of the electron density. The phase difference ϕ between a wave in a plasma and a wave in the air outside the plasma can then be described by:

$$\Delta\phi = \int (k_0 - k_{plasma})dl = \frac{\omega}{c} \int (N - 1)dl. \quad (2.34)$$

Substituting the index of refraction into Equation 2.34 yields

$$\Delta\phi = \frac{\omega}{c} \int ((\omega_p^2/\omega^2 - 1)^{1/2} - 1)dl, \quad (2.35)$$

which can be simplified further with a binomial expansion for the case where $\omega_p \ll \Omega$, defining the wave frequency as $\omega = 2\pi c/\lambda$ to substitute into Equation 2.35, which becomes

$$\Delta\phi = \omega/c \int (\omega_p^2/2\omega^2)dl = \frac{\lambda e^2}{4\pi c^2 m_e \epsilon_0} \int n_e dl. \quad (2.36)$$

For relevant MST parameters, Equation 2.36 becomes:

$$\Delta\phi = 2.814 * 10^{-15} \lambda \int n_e dz, \quad (2.37)$$

where λ is the wavelength of the electromagnetic wave, and z is the distance along the length of the chord in the plasma, in the vertical direction.

2.2 Polarimetry

The FIR laser system can also take advantage of the fact that the plasma exhibits birefringence. That is, the ordinary and extraordinary modes of a beam will have different indices of refraction, given a small but finite Y (Equation 2.28), which for interferometry was assumed to be $Y \ll 1$. The Appleton-Hartree dispersion relation for small, nonzero Y then becomes:

$$N^2 \approx 1 - X \pm XY \cos \theta, \quad (2.38)$$

with the addition referring to the ordinary (O) wave and the subtraction referring to the extraordinary (XO) wave. For interferometry this correction leads to a fractional correction on the order of $Y \cos \theta$ in the density which can be corrected for, but is often ignored given $\omega \ll \Omega$. If the O and XO modes of a polarized wave can be expressed as orthogonally polarized, an effect known as Faraday rotation will occur. The two modes will have a phase difference:

$$\Delta\phi = (N_O - N_X) \frac{\omega}{c} z, \quad (2.39)$$

which leads to the wave still having linear polarization, but being rotated by an angle $\Delta\phi/2$. The Faraday rotation angle therefore becomes:

$$\alpha = \frac{\Delta\phi}{2} = \frac{1}{2} (N_O - N_X) \frac{\omega}{c} z \approx \frac{1}{2} \frac{XY \cos \theta}{(1 - X)^{1/2}} \frac{\omega}{c} z. \quad (2.40)$$

For a nonuniform plasma, the total Faraday rotation of the beam along the path will therefore become:

$$\alpha = \frac{1}{2} \int \frac{\omega_p^2 \Omega \cos \theta}{c \omega^2 (1 - \omega_p^2 / \omega^2)^{1/2}} dl \approx \frac{e^2 \lambda^2}{8 \pi m_e^2 c^3 \epsilon_0} \int n_e \vec{B} \bullet \vec{dl}. \quad (2.41)$$

For relevant MKS values, Equation 2.41 becomes:

$$\alpha = 3 * 10^{-13} \lambda^2 \int n_e(l) \vec{B} \bullet \vec{dl}, \quad (2.42)$$

which gives a relation for the magnetic field parallel to the electromagnetic wave's direction of propagation.

2.3 The MST FIR system

The FIR interferometer-polarimeter system is a vertically viewing heterodyne system that can be used to measure parameters such as the electron density with high time response to a high degree of accuracy. The laser functions by having the three formic acid laser cavities optically pumped by a 70–100 W CO₂ gas laser, producing three FIR lasers with slightly different frequencies. When the lasers are combined, the result is a modulated signal which can be used to extract the relative phase between the lasers. The system can be operated with only two lasers, to provide only the density (one probe beam and reference beam) or Faraday rotation (two probe beams) or with all three lasers to provide two density measurements and the Faraday rotation, which can be differentiated by the three separate beat frequencies between the three lasers. A simplified schematic of the laser system can be seen in Figure 2.1, showing full three beam interferometer-polarimeter operation.

The pumping laser is a commercial continuous power 100 W CO₂ gas laser built by Coherent, Inc. It is an RF-excited sealed GEM-Select-100 which consists of a liquid cooled gas filled discharge tube, a partially reflective output coupler, a fixed grating, and a movable piezo electric mirror to adjust the cavity length. The piezo electric allows for the CO₂ laser frequency to be tuned to the FIR pumping frequency. The CO₂ laser operates at a wavelength of $\sim 9.27 \mu\text{m}$, and is driven by an external RF source that uses a DC power supply.

The CO₂ lasing transition results from molecular vibrational states, instead of the atomic transitions responsible for shorter wavelength lasers. The CO₂ molecule, seen in Figure 2.2, is subject to vibrational energy due to bending, symmetrical stretching, and asymmetrical stretching. When the molecule relaxes to a lower energy vibrational state, a photon is released, and due to the plentiful nature of the vibrational states, the output laser wavelength is more continuous than for shorter wavelength lasers, which generally depend on transition of electrons. In order to obtain the required monochromatic laser emission necessary to efficiently pump the FIR lasers, a controllable grating is used to isolate the wavelength for a vibration of interest. In order to enhance excitation of the CO₂, other gases are introduced. Nitrogen gas, which has one degree of vibrational freedom,

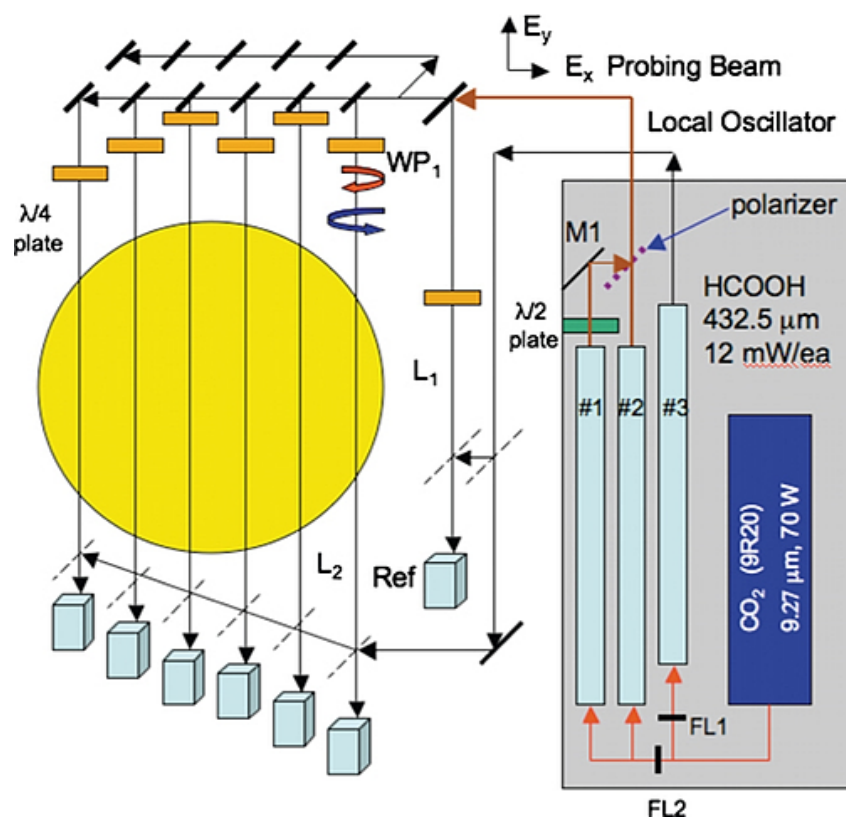


Figure 2.1 Simplified configuration of the 11 chord FIR interferometer-polarimeter system.
 (Reproduced from Parke, et. al, Ref. [45])

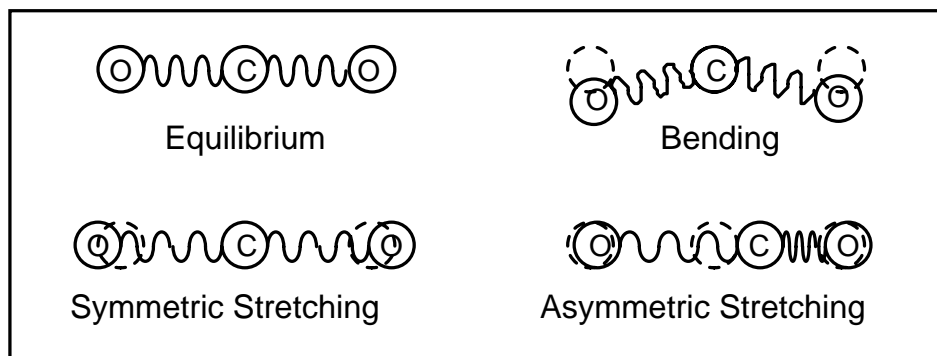


Figure 2.2 Cartoon of the three types of vibration a CO_2 molecule is subject to. (Reproduced from Lanier, Ref. [44])

is easily excited by collisions in the discharge tube to a similar energy to CO_2 , and can efficiently transfer energy to the CO_2 excited state via collision. Stimulated emission then allows the CO_2 molecule to radiate its energy. To prevent re-absorption, Helium gas is added, which enhances collisional de-excitation of the CO_2 molecules.

The FIR lasers convert the ~ 10 micron CO_2 laser radiation into three roughly independent lasers with significantly longer wavelength, on the order of 100's to 1000's of microns, depending on the lasing medium being used. For the MST FIR system, Formic Acid ($HCOOH$) is used, which yields a wavelength of ~ 432.5 microns (≈ 693 GHz). Output power can be optimized by using a Fabry-Perot etalon for each laser cavity consisting of a quartz plate output coupler and a wire mesh. Although the input CO_2 laser power is 20–30 W per FIR laser cavity, the output laser power is only on the order of ~ 10 –30 mW. When the laser power is optimized, the cavity length can be changed independently for each cavity by using a motor-mounted mirror. The cavity length dictates the laser frequency, and differences between the cavity frequencies produce the interference frequency (IF) of the lasers, which can be tuned based on the requirements of the system.

By using the same CO_2 laser to pump all three cavities, any fluctuations in CO_2 power will be equally distributed to each cavity. CO_2 power fluctuations can be caused by changes in temperature, vibrations, or feedback laser power from the system. With this configuration, even if the FIR laser power fluctuates, the modulated signal will be very stable.

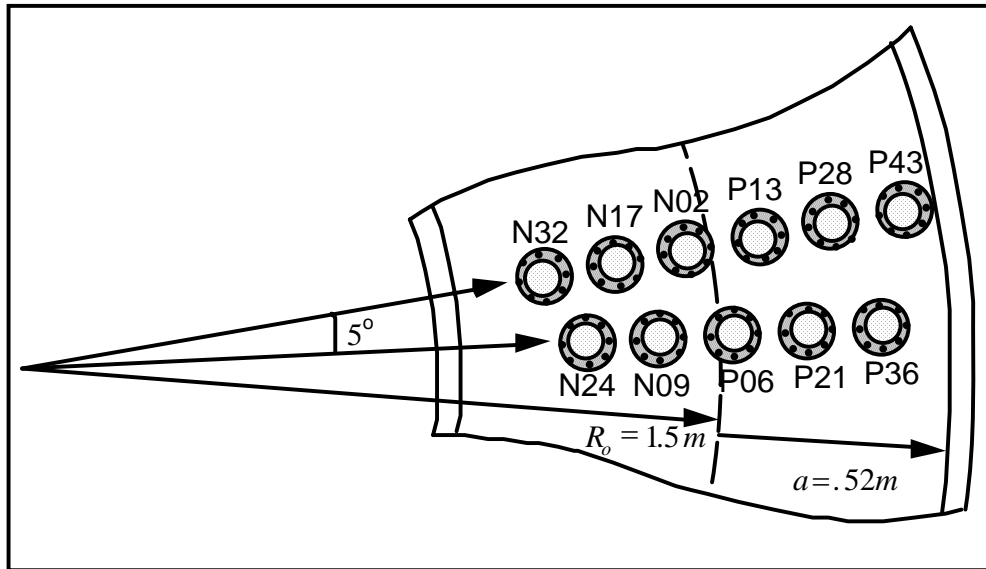


Figure 2.3 Schematic of the 11 vertically viewing FIR chords separated into 2 sets, displaced 5° toroidally. (Reproduced from Lanier, Ref. [44])

The eleven FIR chords are separated into two sets that are toroidally displaced by five degrees. Figure 2.3 shows how the chords are spaced on the MST, with each chord displaced along the minor radius of the machine by ~ 8 cm. The chords view impact parameters ranging from -32 cm to 43 cm, with the specific chord impact parameters, toroidal location, and vertical chord length cited in Table 2.1. While the toroidal separation was initially designed to limit field errors in the conducting shell of the vacuum vessel, it proves to be useful for measuring toroidal wavenumbers associated with density fluctuations related to the work in this thesis, as will be discussed in Chapter 5.

The laser power is distributed through the system via a system of thin metallic wire meshes acting as beam splitters. These wire meshes, manufactured by Buckbee/Mears of St. Paul, MN, with later precision electro-forming in New York, are electro-formed out of nickel substrate and can have a variety of line densities, controlling the reflected and transmitted power distributions. The meshes can be difficult to align with tip-tilt controls, resulting in difficulty in laser alignment, particularly for polarimetry alignments. They are also quite fragile, requiring a number of protective measures to limit replacement, which would require some degree of realignment for the laser. This

Chord Name	Impact Parameter $R - R_0$ (cm)	Toroidal Angle ϕ (degrees)	chord length L (cm)
N32	-32	255	81.97
N24	-24	250	92.26
N17	-17	255	98.29
N09	-9	250	102.4
N02	-2	255	103.9
P06	6	250	103.3
P13	13	255	100.7
P21	21	250	95.14
P28	28	255	87.64
P36	36	250	75.04
P43	43	255	58.48

Table 2.1 Name, impact parameter, toroidal angle, and chord length for each FIR chord.
(Reproduced from Lanier, Ref. [44])

includes covering the optics above the machine with aluminum, and the detection optics below the machine with plastic covers while the diagnostic is not in operation.

The lasers, after passing through the vacuum vessel and combining at wave-splitters under the machine, were measured with a UCLA fabricated diode/pre-amplifier assembly for much of the data taken in this thesis. The diode, which is a Gallium/arsenide (GaAs) Schottky corner-cube mixer, has a relatively low noise-equivalent-power ($\approx 10^{-10} \text{ W}/\sqrt{\text{Hz}}$) and a time response of several MHz [46]. However, the measurement efficiency of the corner-cube mixer is very sensitive to incident angle. This can be problematic for initial alignment and for cases such as high density fluctuations or high power plasma fluctuations, where the FIR beam can be steered away from the mixer. The FIR beam is focused into the mixers with a plano-convex polyethylene lens with a focal length of 8 cm [44]. The detector assembly for each chord is mounted on a rotating stage which is then affixed to 3 orthogonal translating stages, allowing a large amount of freedom of movement for detector placement. The alignment procedure involves iteratively adjusting the mixer incident angle and position until the signal power is maximized. The process is repeated for all 12 mixers (eleven chords and the reference), and should be repeated every few months to ensure peak diagnostic performance. The UCLA fabricated diode/pre-amplifier assembly was recently upgraded, and this upgrade will be discussed in Section 2.4.

This setup required a pre-amplification box fed into a variable amplifier to get appreciable signal [44]. This pre-amplifier, built by Don Holly, amplified and filtered the signal, removing low ($< 300 \text{ kHz}$) and high ($> 3 \text{ MHz}$) frequency components present in the signal. The preamp gain is $\sim 10^3$ for the frequencies near the laser interference frequencies used experimentally. The output of the two-stage preamplifier is then fed into a variable amplifier for adjusting signal levels before being fed into the digitizers. This allows modification of the signal amplitude to obtain optimal signal resolution on the digitizer. While the phase measurement is inherently amplitude independent, there is still a minimum and maximum allowed amplitude that should be avoided: too much power and the mixers can saturate, too little power and the phase can be difficult to extract. The amplitude modulation on the amplifier allows the signal from each mixer to be reliably larger than the minimum during operation. Even with minimal amplification, some channels have

sufficient signal to saturate the mixer pre-amplifiers, resulting in a non-sinusoidal output signal which severely contaminates the phase measurement. To dampen the power on these channels, pieces of paper are placed in the beam line between the lens and the mixer to attenuate the signal.

2.4 The FIR upgrade

Recently, in 2014, new planar-diode mixers were installed, replacing the previously used corner-cube mixers [46, 45]. The new mixers have increased sensitivity and reduced noise floor, allowing for resolution of fluctuations up to 250 kHz for polarimetry and up to 600 kHz for interferometry. This is seen as a five fold lower phase noise and a ten fold higher sensitivity. A picture of the old corner-cube (a) and new VDI planar-diode (b) mixers is included in Figure 2.4. The laser input for each mixer is pointed down in the figure, with an amplifier attached via an SMA connection on top of the mixer. The planar-diode mixers can also be deployed in a multi-mixer array, potentially allowing for a dramatic increase in wavenumber sensitivity. By increasing the frequency and wavenumber sensitivity of the diagnostic, it may become possible to describe a larger range of drift wave turbulence, which is the focus of this thesis.

Experiments were conducted to compare the operation of the corner-cube and planar diode mixers [46]. The two mixer configurations are differentiated primarily by the method of coupling the radiation, but have some similarities. Both mixers employ a Schottky-barrier diode for fast time response and have apertures of width ~ 1.5 mm. For the corner-cube mixer, the radiation is coupled into a whisker-diode contact via a quasi-optical configuration. The planar-diode mixer has a 2 mm aperture conical horn built into the detector block and employs a fundamental waveguide coupling to the diode. Both mixers have the signal and local oscillator radiation coupled into the mixer via the same optical path. The corner-cube mixers consist of a whisker contact with a diode chip, which is delicate and has a noise response dependent on the quality of the electrical contact, while the planar-diode mixers are constructed using semiconductor planar deposition techniques. The corner-cube mixers were made at UCLA, and had been used reliably on the MST for over 20 years, while the planar-diode mixers have been in use for ~ 2 years. The planar-diode mixers

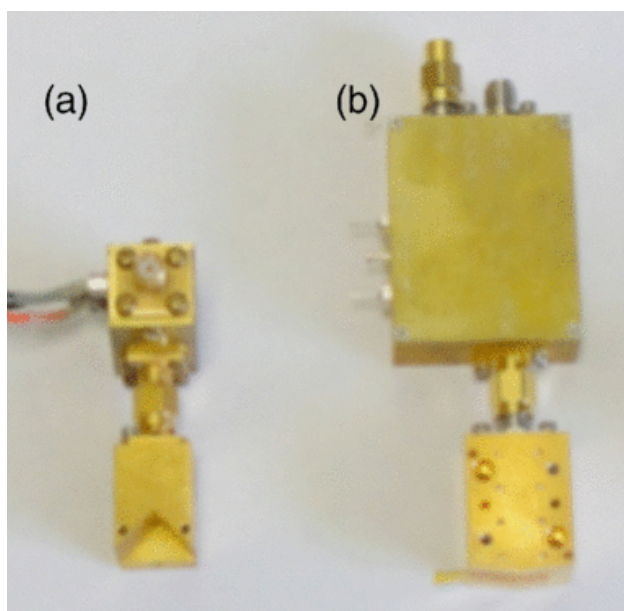


Figure 2.4 (a) Corner-cube (and amplifier) and (b) VDI planar-diode (and amplifier) mixers designed for operation with 700 GHz source radiation. (Reproduced from Ding, et. al, Ref. [46])

do not require the additional amplification stages to maintain appreciable power, so there are no bandwidth restrictions due to amplifier response [46].

Plasma tests of the corner-cube and planar-diode mixers using Faraday rotation show significant improvement in noise floor and sensitivity. By examining phase fluctuations in the Faraday effect measurement, broadband magnetic turbulence fluctuations can be explored. Data is taken near the magnetic axis and the first order expansion for the fluctuating Faraday signal is given by $\Phi_F \sim \int \delta n_e \vec{B} \cdot d\vec{l} + \int n_e \delta \vec{b} \cdot d\vec{l}$, where the first term is negligible because the equilibrium magnetic field is perpendicular to the laser propagation direction. Broadband fluctuations, likely dominated by radial magnetic field fluctuations for the central chord in standard sawtoothed RFP discharges for the two mixers, shown in Figure 2.5, show a reduction of the noise floor by a factor of 5 for the planar-diode mixers, and a sensitivity to fluctuations up to ~ 400 kHz, compared to ~ 150 kHz for the corner-cube mixers. This clearly demonstrates that the planar-diode mixers are significantly more well-suited for turbulence measurements.

The planar-diode mixers have several other potential benefits over the corner-cube mixers. Due to the increased sensitivity of the planar diode mixers, they can be operated without a focusing lens while maintaining an acceptable signal to noise ratio. The planar-diode mixers also have precision located dowel pins on each side, allowing multiple mixers to be arranged in a linear array. When in this configuration, the maximum measurable wavenumber of the system increases from $\sim 0.18 \text{ cm}^{-1}$ by an order of magnitude, to $\sim 2 \text{ cm}^{-1}$. This allows for the potential to measure high frequency, high wavenumber drift-wave-like instabilities. While much of the data in this thesis was taken with the corner-cube mixers, several experiments were done with the planar-diode mixers which are discussed in Section 5.4.

2.5 Summary

The FIR system is an eleven chord vertically viewing interferometer/polarimeter diagnostic system. The system can be used to measure high frequency fluctuations, up to several hundred kHz, in both line-integrated density and Faraday rotation. Toroidal separation of the chords allows for toroidal wavenumber measurements up to 0.18 cm^{-1} . The system has been upgraded with

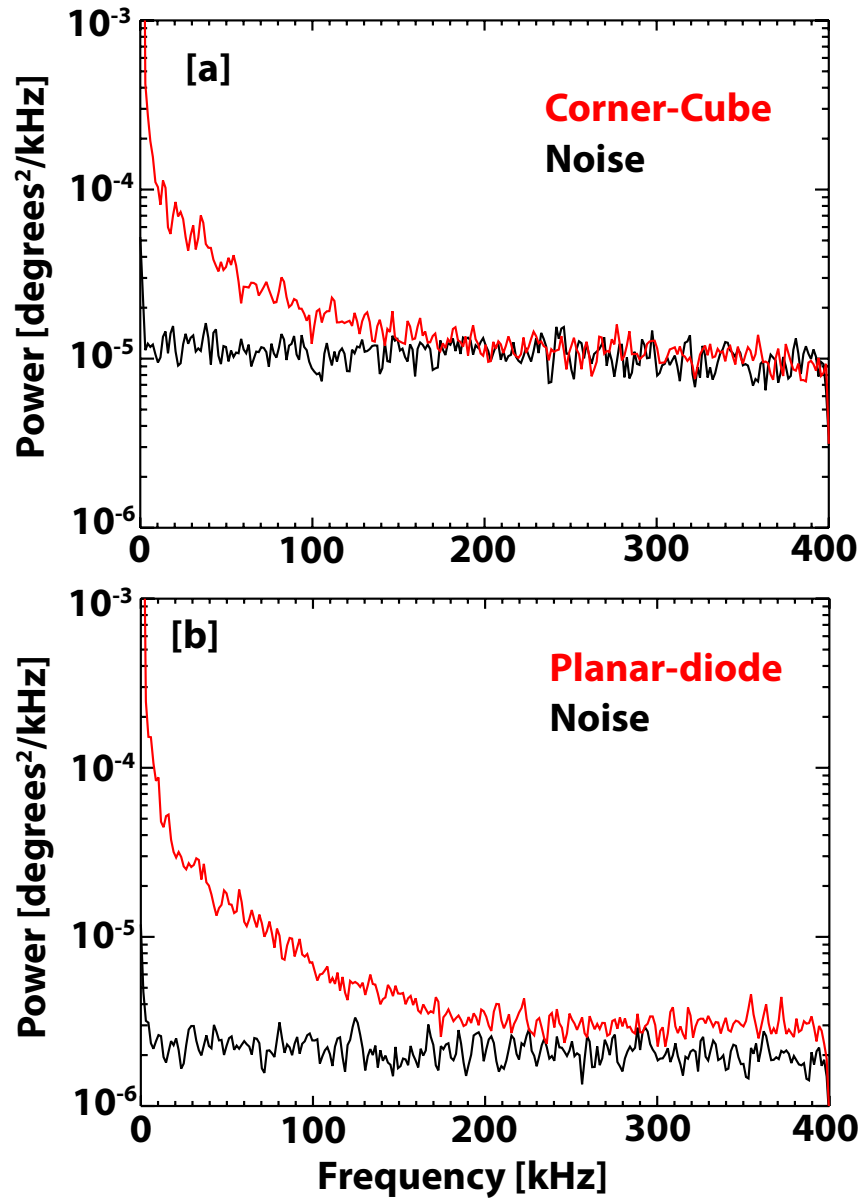


Figure 2.5 Faraday-effect phase fluctuation frequency spectra for cases with (red) and without (black) plasma using (a) corner-cube mixer and (b) planar-diode mixer. Data are ensemble over 32 events during the time window 0.5-2.5 ms after sawtooth crash. (Reproduced from Ding, et. al, Ref. [46])

new planar-diode mixers that are significantly more sensitive than the previously used corner-cube mixers. The new mixers are easier to align and require less input power, allowing them to be used in various interesting new experiments that may improve turbulence measurements available both temporally and spatially, initially by increasing sensitivity to high frequencies, and by allowing multiple measurements per chord.

Chapter 3

Transport and instabilities

A major focus of work across many devices and plasma configurations has been the study of thermal transport in fusion relevant plasmas. In order to attain a burning plasma, thermal transport must be reduced to acceptable levels. A major source of transport has been attributed to plasma instabilities, via either stochastic transport or through small scale turbulence [47]. This chapter will initially focus on stochastic transport in the RFP due to MHD scale turbulence in Section 3.1. Then the focus will shift in Section 3.2 to micro-instabilities that can dominate transport when large-scale instabilities are suppressed, including brief discussions of several of the instabilities that are predicted in improved confinement RFP plasmas.

3.1 Plasma transport

3.1.1 Stochastic transport

Tearing and reconnection at rational surfaces allows for magnetic islands. These islands, seen in Figure 3.1, allow heat and particles to rapidly traverse the radial extent of the island, degrading the confinement. If islands overlap, as they do in standard RFP operation, then the magnetic field can become stochastic, as seen in Figure 1.6(a), further degrading confinement. Instead of heat and particles only transporting across the island width, they can transport across a whole stochastic region, which can include a significant radial extent of the plasma.

Rechester and Rosenbluth [3], by modeling electron heat transport via parallel conduction along wandering field lines, addressed the fusion relevance of transport in a stochastic magnetic field in 1978, where they conjectured that the magnetic diffusion coefficient D_m would take the

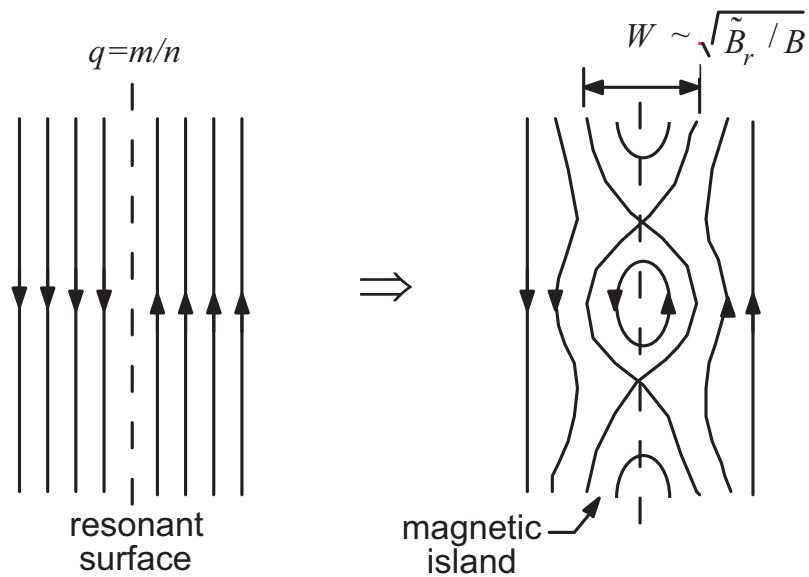


Figure 3.1 Rational surfaces permit tearing and reconnection of the magnetic field to occur, allowing islands to form. Magnetic islands degrade confinement by allowing rapid transport across the island's width. (Reproduced from Lanier, Ref. [44])

form:

$$D_m \approx L_{ac} \frac{\langle \tilde{b}_r \rangle^2}{B_0^2}, \quad (3.1)$$

where $\langle \tilde{b}_r \rangle^2 / B_0^2$ is the fluctuation to mean field ratio for the radial magnetic field, and L_{ac} is the autocorrelation length of the diffusion of the magnetic field. In the MST the ratio of the fluctuating to mean field is $\langle \tilde{b}_r \rangle / B_0 \approx 1 - 2\%$. The autocorrelation length is approximately a meter for the MST, and therefore $D_m \approx 1. \times 10^{-4}$ m. In the collisionless limit ($\lambda_{mfp} \gg L_{ac}$) the stochastic electron heat conductivity $\chi_{st,e}$ becomes:

$$\chi_{st,e} = \frac{\langle (\Delta r)^2 \rangle}{\Delta t} = \frac{D_m \lambda_{mfp}}{\tau_c} = D_m v_T, \quad (3.2)$$

where τ_c is the collision time, λ_{mfp} is the mean free path between collisions, and $v_T = \sqrt{T/m}$ is the thermal velocity. In the MST, λ_{mfp} is on the order of 10's of meters, so the collisionless limit is a good approximation [33].

3.1.2 Heat transport

Electron heat transport conductivity, χ_e , is decreased in the core of PPCD plasmas by over an order of magnitude compared to standard plasmas, as seen in Figure 3.2 [30, 33, 48]. This quantity gives an indication of the conducted heat flux:

$$Q_e = \chi_e n_e \nabla_r T_e, \quad (3.3)$$

and therefore a measure of the global energy confinement time. It is observed that in areas where the magnetic field is stochastic, the collisionless stochastic transport model adequately describes the measured heat diffusivity. In PPCD, the magnetic field is not stochastic in some areas of the plasma, and non-stochastic transport may be dominant.

3.2 Microinstabilities

In optimized tokamak and stellarator devices, the dominant source of transport is now believed to be due to drift-wave driven microturbulence[14]. Drift waves arise due to the creation of diamagnetic drift currents \vec{J} that are required to satisfy radial force balance $(\vec{J} \times \vec{B})/c = \nabla p_e + \nabla p_i$,

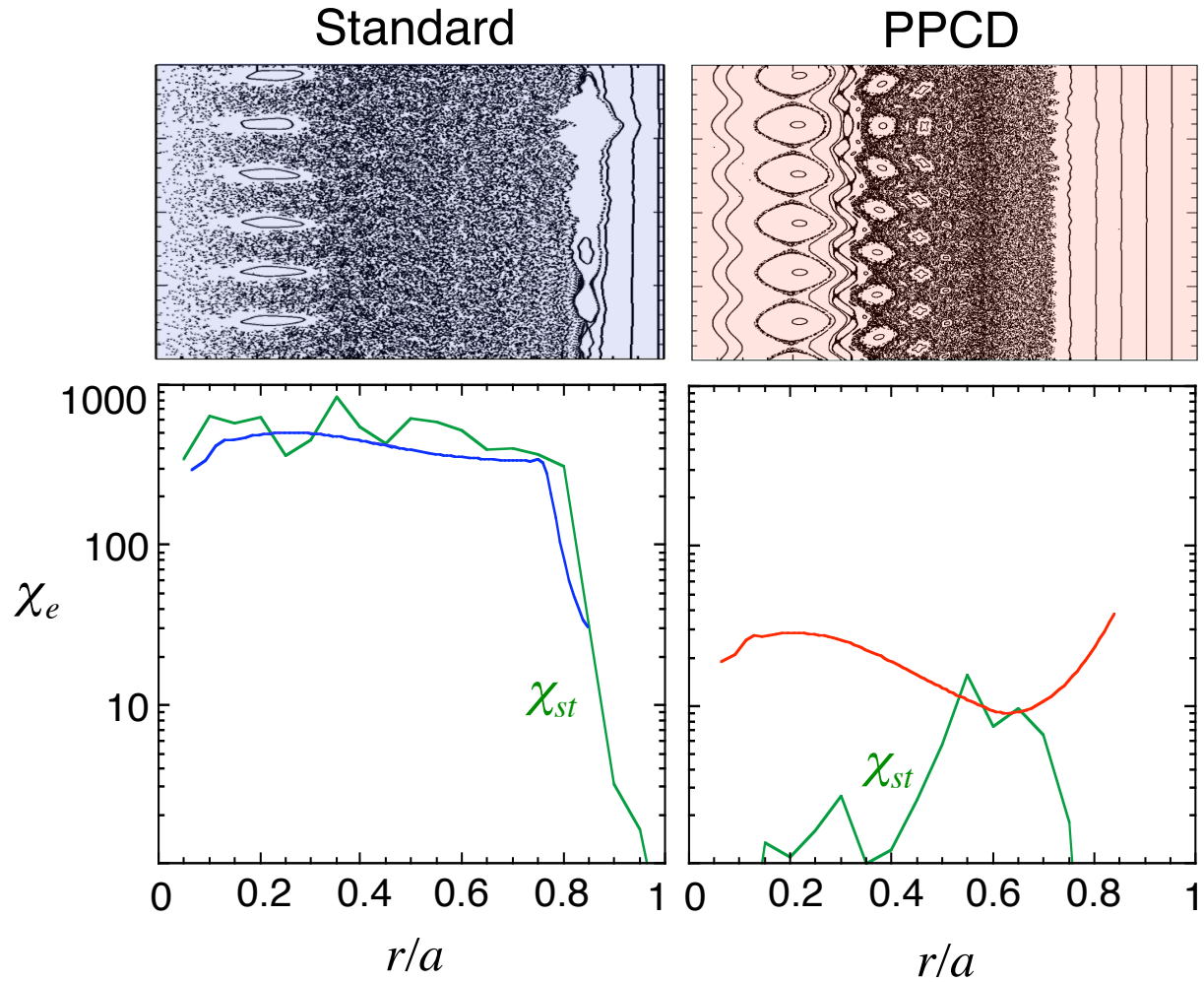


Figure 3.2 Heat transport conductivity χ_e compared to the stochastic heat transport conductivity in standard and PPCD plasmas. In areas of the plasma where the magnetic field is stochastic, the stochastic quantity adequately describes the heat transport. (Reproduced from Sarff, Ref. [33])

with \vec{B} being the background magnetic field, and p_e and p_i being the electron and ion pressures, respectively. The currents are associated with diamagnetic drift velocities $\vec{v}_{Dj} = (1/(q_j n_j B)) \nabla p_j$, for j being a label for a particle species with charge q_j , density n_j , and pressure p_j . Drift wave instabilities are driven by gradients in plasma pressure, temperature, or density and have frequencies on the order of the diamagnetic drift frequency $\omega_j^* = \vec{k} \bullet \vec{v}_{Dj}$. The essential physics for drift waves are presented in Figure 3.3. Gradients perpendicular to the background magnetic field enable the propagation of waves in the diamagnetic direction through the generation of $\vec{E} \times \vec{B}$ drift. Under certain circumstances, phase differences may arise between the various fluctuations that can generate a positive growth rate and lead to instability.

A variety of instabilities can be classified as drift waves, including ion temperature gradient (ITG) and electron temperature gradient (ETG) modes, the trapped electron mode (TEM), and the micro-tearing mode (MTM). These instabilities can be influenced by various characteristics of the plasma, including the plasma pressure, collisionality, and the magnetic geometry. More information on the specifics of these instabilities can be found in Horton [50]. The results of this thesis will focus primarily on density-gradient-driven TEM-like instabilities predicted to be unstable by gyrokinetic simulations in optimized PPCD plasma equilibria. Ion temperature gradient driven instabilities are predicted in other plasma equilibria, and will also be explored.

3.2.1 The trapped electron mode

The TEM is characterized by electrons that are magnetically trapped in the "low-field" side of tokamak devices [51, 52, 53, 54], in magnetic wells in stellarator devices [55, 56], or in the edge of improved confinement RFP discharges [48, 37, 57]. Trapped electron modes are driven by pressure gradients in the presence of magnetic curvature, and are classified into 2 categories: density-gradient driven and temperature gradient driven. The key parameters for studying TEMs are the normalized pressure gradients R_0/L_{n_e} and $R_0/L_{T_{e,i}}$, where R_0 is the major radius of the device, and $L_x = -x/\nabla x$ is the gradient scale length.

The development of TEM-type instabilities can lead to the generation of zonal flows [58], which are characterized as an azimuthally symmetric band-like shear flow, and are found both in

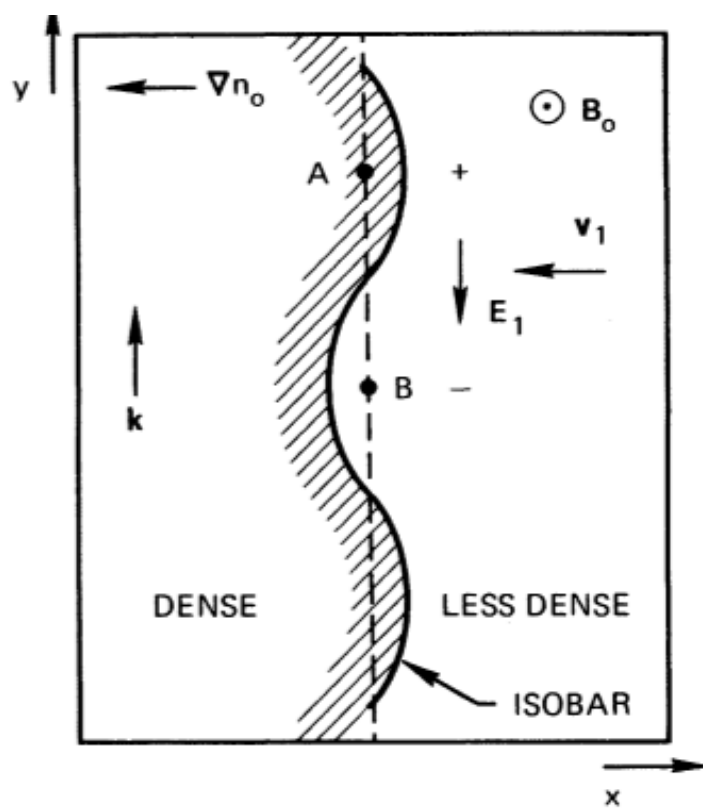


Figure 3.3 Physical mechanism for a drift wave. (Reproduced from Chen, Ref. [49])

lab plasmas and in nature. They are expected to be seen as an $n = 0$ flow driven by $n \neq 0$ drift waves. Zonal flows act to partially suppress drift wave turbulence, and can act as a transport barrier. Further description of drift wave driven zonal flows can be found in Diamond et al. [59] and Terry [60].

3.2.2 The ion temperature gradient driven mode

The ion temperature gradient (ITG) mode has been thoroughly explored in tokamaks, and arises from gradients in the ion temperature profile [61]. The ITG driven instability can have significant impact on high temperature burning plasmas. ITG turbulence may drive thermal conduction that carries heat from fusion reactions in the core to the edge of the plasma. Exploring ITG instabilities is important to fusion plasma research. In tokamaks, the saturation of ITG turbulence has been found to depend critically on turbulently driven zonal flows. ITG is a candidate for driving turbulent heat transport in tokamaks and stellarators [62]. ITG instabilities are classically driven by the electrostatic dynamics of passing ions. In the RFP, ITG instabilities have been predicted for PPCD plasma equilibria where the ion temperature gradient is comparable to or stronger than the density gradient [57].

3.2.3 The micro-tearing mode

Micro-tearing modes (MTMs) are electromagnetic modes characterized by rapid, small scale magnetic reconnection events. This can degrade local confinement significantly as particles are allowed to traverse radially. They are distinguished from magnetic tearing modes in the RFP by the scale of the magnetic tearing. Magnetic tearing modes in the RFP are characterized by the global scale of the event, while microtearing modes exist over small scales of the plasma. The MTM is driven by the electron temperature gradient, as opposed to the current gradient for the global tearing mode [63]. While these instabilities were originally predicted in some improved confinement RFP equilibria by Carmody, et. al [63] and potentially observed in the RFX-MOD device [64], they appear to be stable in improved confinement MST equilibria [57], and hence are less likely to arise.

3.3 Summary

Thermal transport is an incredibly important area of research in plasma physics, and must be understood to achieve a burning plasma. In the RFP, thermal transport in standard discharges are dominated by overlapping magnetic islands that create significant stochasticity in the magnetic field. By suppressing the stochasticity in the magnetic field, drift wave turbulence can become important to the transport characteristics of the plasma. There are several sources of drift wave turbulence that can have various characteristics. Exploring these possible drift waves in the RFP will include gyrokinetic simulations and experimental results.

Chapter 4

Overview of GENE simulations

Gyrokinetic simulations of improved confinement RFP plasmas, performed by Carmody et. al. [14] and Williams et. al. [57], show that drift wave instabilities are expected in these plasma equilibria. Comparing the gyrokinetic results presented in this chapter with the experimental results in the next chapter, the turbulence and transport characteristics of improved confinement RFP plasmas can be explored. The kinetic theory base and gyrokinetic simplifications will be explored in Section 4.1. Section 4.2 will discuss the implementation of gyrokinetic codes to the RFP geometry. Finally, Sections 4.3 and 4.4 will discuss the linear and nonlinear results of GENE simulations performed by Carmody and Williams.

4.1 Modeling

4.1.1 Kinetics

Ideally, all plasma dynamics could be described by the Newton-Maxwell system of equations. However, due to the incredibly large number of particles in a fusion plasma, it is incredibly unrealistic to track the position and momentum of each particle at all points in time. A statistical approach is significantly more tractable, describing the plasma by a set of distribution functions. In a hot, weakly coupled plasma, multi-particle correlations involving three or more particles can be neglected, and two particle interactions are reduced to a collision operator $C(f_{s'}, f_s)$ for a single particle distribution function $f_s(\vec{q}, \vec{p})$ in a six dimensional phase space where q and p are the position and momentum of a particle, respectively. An evolution equation of f_s is given by the

Boltzmann equation:

$$\frac{Df_s}{Dt} \equiv \frac{\partial f_s}{\partial t} + \{f_s, H_s\} = C(f_s', f_s), \quad (4.1)$$

where the Poisson bracket $\{f_s, H_s\}$ in coordinates \vec{q} and \vec{p} is defined as:

$$\{f_s, H_s\} = \frac{\partial f_s}{\partial q_i} \frac{\partial H_s}{\partial p_i} - \frac{\partial f_s}{\partial p_i} \frac{\partial H_s}{\partial q_i}, \quad (4.2)$$

and $H_s(\vec{q}, \vec{p})$ is the Hamiltonian of collisionless single particle motion,

$$H_s(\vec{q}, \vec{p}) = \frac{1}{2m_s} |\vec{p} - \frac{e_s}{c} \vec{A}|^2 + e_s \phi, \quad (4.3)$$

where e_s and m_s are the charge and mass of particle species s , c is the velocity of light, ϕ is the electrostatic potential, and \vec{A} is the vector potential for the magnetic field. Because collisions occur on time scales significantly slower than characteristic frequencies for many turbulent fluctuations such as some types of drift waves, a collisionless model is often used. Therefore, Equation 4.1 becomes:

$$\frac{Df_s}{Dt} \equiv \frac{\partial f_s}{\partial t} + \{f_s, H_s\} = 0. \quad (4.4)$$

By taking the velocity moments of the distribution function, the particle density n_s and current density j_s are found to be:

$$n_s = \int f_s d^3 p, \quad (4.5)$$

$$j_s = e_s \int v f_s d^3 p, \quad (4.6)$$

where $v = [p - (e_s/c) \vec{A}] / m_s$. The electromagnetic fields \vec{E} and \vec{B} are determined by substituting n_s and j_s into the Maxwell equations:

$$\nabla \times \vec{E} = -\frac{1}{c} \frac{\partial \vec{B}}{\partial t}, \quad (4.7)$$

$$\nabla \times \vec{B} = \frac{4\pi}{c} \sum_s j_s + \frac{1}{c} \frac{\partial \vec{E}}{\partial t}, \quad (4.8)$$

$$\nabla \cdot \vec{E} = 4\pi \sum_s e_s n_s, \quad (4.9)$$

$$\nabla \cdot \vec{B} = 0, \quad (4.10)$$

which give a basic description of a collisionless plasma [65].

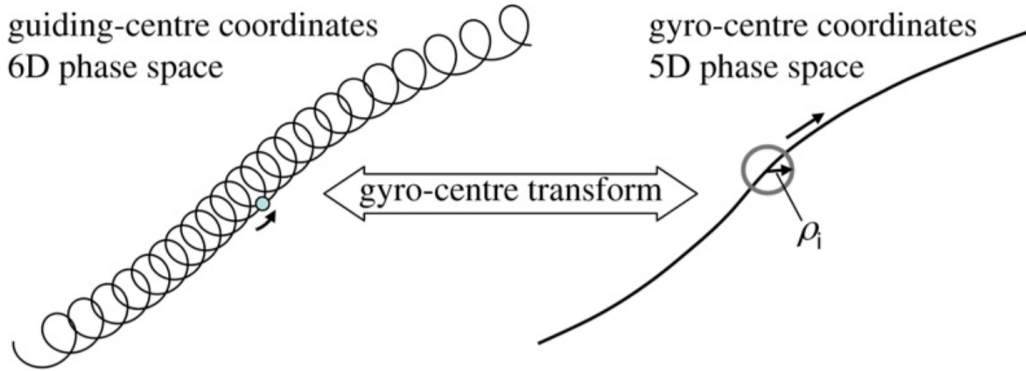


Figure 4.1 Gyrocenter approximation used in gyrokinetic codes. (Reproduced from Garbet et al., Ref. [77])

4.1.2 Gyrokinetics

While the Vlasov-Maxwell system reduces the complexity of the kinetic description of a plasma, it includes a very large range of spatial and temporal scales. To avoid simulating multiple hierarchies of scales, a nonlinear gyrokinetic model was developed by eliminating phenomena with frequency on the order of the cyclotron frequency ($\omega \gtrsim \Omega_s$) while keeping essential kinetic effects. This formulations consists of a guiding-center transform [66, 67, 68, 69] and a gyro-center transform [70, 71, 72, 73] based on Hamiltonian or Lagrangian formalism with the Lie perturbation theory [74, 75]. Further information on this formalism can be found in Garbett et. al. [65].

As shown in Figure 4.1, single particle motion in strong ambient magnetic fields consists of a fast periodic gyro-motion and a slower guiding-center motion. Low frequency perturbation satisfying a particular ordering, such that $\omega/\omega_c \ll 1$ and $r_c/R_0 \ll 1$ (where ω is the electromagnetic frequency of interest, ω_c is the gyro-frequency, r_c is the gyroradius, and R_0 is the major radius), primarily affect the guiding-center motion, and the magnetic moment $\mu = m_s v_\perp^2 / 2B_0$ becomes approximately adiabatically invariant. This allows a coordinate transformation to gyro-center coordinates, where μ is invariant and the gyro-phase ξ is averaged over [76].

The Euler-Lagrange equation in conjunction with a modified Lagrangian using the previous approximations provides equations for time derivatives of all the phase space coordinates. The

Vlasov equation contains these derivatives, and in the absence of collision can be written:

$$\frac{df}{dt} = \frac{\partial f}{\partial t} + \dot{\vec{X}} \cdot \nabla f + v_{\parallel} \frac{\partial f}{\partial v_{\parallel}} + \dot{\mu} \frac{\partial f}{\partial \mu} = 0, \quad (4.11)$$

where \vec{X} is the gyro-center position, v_{\parallel} is the parallel velocity, and a dot over a variable represents the time derivative of that variable ($\dot{x} \equiv \partial x / \partial t$). This equation states that the phase space volume of a particle distribution function f is conserved. Applying the drift velocity definitions:

$$\vec{v}_{\chi} = -\frac{c}{B_0^2} \nabla \chi_1 \times \vec{B}_0, \quad (4.12)$$

$$\vec{v}_{\nabla B} = \frac{\mu}{m\Omega} \vec{b}_0 \times \nabla \vec{B}_0, \quad (4.13)$$

$$\vec{v}_c = \frac{v_{\parallel}^2}{\Omega} (\nabla \times \vec{b}_0)_{\perp}, \quad (4.14)$$

the modified potential:

$$\chi_1 = \bar{\phi}_1 - \frac{v_{\parallel}}{c} \bar{A}_{1\parallel} + \frac{1}{q} \mu \bar{B}_{1\parallel}, \quad (4.15)$$

and assuming that the perturbed field is much smaller in scale than the equilibrium field, the time derivatives for the relevant variables is found to be:

$$\dot{\vec{X}} = v_{\parallel} \vec{b}_0 + \frac{B_0}{B_{0\parallel}^*} (\vec{v}_{\chi} + \vec{v}_{\nabla B} + \vec{v}_c), \quad (4.16)$$

$$\dot{v}_{\parallel} = \left(\frac{\vec{b}_0}{m} + \frac{B_0}{m v_{\parallel} B_{0\parallel}^*} (\vec{v}_{\chi} + \vec{v}_{\nabla B} + \vec{v}_c) \right) \cdot \left(-q \nabla \bar{\Phi}_1 - \frac{q}{c} \vec{b}_0 \dot{\bar{A}}_{1\parallel} - \mu \nabla (B_0 + \bar{B}_{1\parallel}) \right), \quad (4.17)$$

$$\dot{\mu} = 0, \quad (4.18)$$

which, when inserted into the Vlasov equation from before, leads to:

$$\frac{\partial f}{\partial t} + \left(v_{\parallel} \vec{b}_0 + \frac{B_0}{B_{0\parallel}^*} (\vec{v}_{\chi} + \vec{v}_{\nabla B} + \vec{v}_c) \right) \cdot \left(\nabla f + \frac{1}{m v_{\parallel}} \left(-q \nabla \bar{\Phi}_1 - \frac{q}{c} \vec{b}_0 \dot{\bar{A}}_{1\parallel} - \mu \nabla (B_0 + \bar{B}_{1\parallel}) \right) \right) \frac{\partial f}{\partial v_{\parallel}}. \quad (4.19)$$

Equation 4.19 can be normalized and numerically solved with certain codes, but it is convenient to continue with a perturbed part of the distribution function $f \Rightarrow f_0 + f_1$, where $\frac{f_1}{f_0} \ll 0$. Introducing a modified distribution function:

$$g_1 = f_1 - \frac{q}{m c} \bar{A}_{\parallel} \frac{\partial f_0}{\partial v_{\parallel}}, \quad (4.20)$$

and the derived quantity

$$G_1 = g_1 - \frac{q}{mv_{\parallel}} \chi_1 \frac{\partial f_0}{\partial v_{\parallel}} \quad (4.21)$$

the perturbed Vlasov equation becomes:

$$\begin{aligned} \frac{\partial g_1}{\partial t} + \frac{B_0}{B_{0\parallel}^*} \vec{v}_{\chi} \cdot (\nabla f_0 - \frac{1}{mv_{\parallel}} \mu \nabla B_0 \frac{\partial f_0}{\partial v_{\parallel}}) + \\ \frac{B_0}{B_{0\parallel}^*} (\vec{v}_{\chi} + \vec{v}_{\nabla B} + \vec{v}_c) \cdot \nabla G_1 + v_{\parallel} \vec{b}_0 \cdot \nabla G_1 \\ - (\frac{1}{m} \vec{b}_1 + \frac{B_0}{mv_{\parallel} B_{0\parallel}^*} \vec{v}_c) \cdot \\ (q \nabla \bar{\Phi}_1 + \frac{q}{c} \vec{b}_0 \dot{A}_{1\parallel} + \mu \nabla (B_0 + \bar{B}_{1\parallel})) \frac{\partial f_1}{\partial v_{\parallel}} \end{aligned} \quad (4.22)$$

Similarly, the gyrokinetic field equations can be derived from Maxwell's equations. Skipping some steps, the field equations can be evaluated to:

$$\sum_j q_j (1 - \Gamma_1(b_j)) \frac{q_j \Phi}{T_{j0}} = \sum_j q_j ((\Gamma_0(b_j) - \Gamma_1(b_j)) \frac{B_{\parallel}}{B_0} + \frac{2\pi B_0}{m_j n_{j0}} \int J_0(\lambda_j) f_j dv_{\parallel} d\mu) \quad (4.23)$$

$$(1 + \sum_j 4b_j \beta_j (\Gamma_0(b_j) - \Gamma_1(b_j))) \frac{B_{\parallel}}{b_0} = - \sum_j 2\beta_j (\frac{B_0}{n_{j0} T_{j0}} \int \mu I_1(\lambda_j) f_j d^3v + \frac{q_j \Phi}{T_{j0}} (\Gamma_0(b_j) - \Gamma_1(b_j))) \quad (4.24)$$

$$\nabla_{\perp}^2 A_{\parallel} = - \frac{8\pi^2 B_0}{c} \sum_j \frac{q_j}{m_j} \int v_{\parallel} J_0(\lambda_j) f_j dv_{\parallel} d\mu \quad (4.25)$$

It is notable that the field equations for Φ and B_{\parallel} are coupled. For small β_j , the parallel magnetic fluctuations are negligible, but in higher β_j scenarios, B_{\parallel} may become significant. Together with the Vlasov equation, the field equations constitute a set of equations that can advance the distribution function in time, providing a physical description of the evolution of the plasmas [76].

While a full plasma system can theoretically be simulated using these equations, this would require significant computational effort, and it is therefore more convenient to reduce the simulated region of the plasma to flux tubes. This limits the gyrokinetic framework to local events, but retains most of the physical effects. More information on flux tube geometry can be found in the references [78, 79, 76]. A full derivation of the gyrokinetic equations, with many intermediate steps is given

in References [76, 63]. Here, some of the most important steps and results from Carmody and William's work has been summarized.

4.2 Gyrokinetic modeling in the RFP

Most gyrokinetic codes (e.g. GENE or GYRO) were originally produced for the tokamak geometry, such that implementation of the code to the RFP geometry requires some important considerations. The code is formulated for toroidal flux, which increases monotonically for a tokamak, but can be multivalued for an RFP due to reversal of the toroidal field at the reversal surface. Several other tokamak assumptions, some subtle, are built into gyrokinetic codes, such as definitions for parallel wavenumber k_{\parallel} or magnetic shear \hat{s} . Therefore, an RFP specific equilibrium is required [80] to adequately explore RFP equilibria at large r/a , where the pressure gradients are largest and drift wave turbulence can be important.

To adapt a gyrokinetic code to the RFP, Carmody et al. developed several equilibrium models [63]. By using the GENE code, which does not rely on tokamak assumptions in the geometry implementation, a wide range of magnetic field equilibria were capable of being tested. GENE contains a circular equilibrium, which can be modified using additional radial dependence into an adjusted circular model (ACM). This is done by replacing the Bessel function $J_0(2\Theta r/a)$ with a function $g(r) = qf(r)$, where q is the safety factor and $f(r)$ is a sixth order polynomial determined to fit the experimental field. With some derivation, the model for the magnetic field becomes:

$$\vec{B} = \frac{B_0 R_0}{R} q f(\epsilon = r/R_0) \left(\vec{e}_{\phi} + \frac{r}{R_0 \bar{q}} \vec{e}_{\theta} \right), \quad (4.26)$$

where B has the magnitude

$$B = \frac{B_0 R_0}{R} |q| f(\epsilon) \sqrt{1 + (\epsilon/\bar{q})^2}. \quad (4.27)$$

This fit has been show to be capable of matching the experimental fields well, even in very high reversal discharges [63].

4.3 Linear GENE results

Linear gyrokinetic studies were performed using the GENE code [17], with reconstructions of experimental profiles taken from an ensemble of 200 kA PPCD plasmas discussed in Section 5.2. Localized flux-tube simulations were performed with effective minor radial extent, $\Delta r = 10\rho_s(10\text{--}20\text{cm})$. Consistent with previous analysis [14], instability is present in the wavenumber range $k_y\rho_s = 0.1 - 1.2$ with frequencies in the electron diamagnetic direction. Trapped electron modes are destabilized by the strong density gradient, in the region $r/a \geq 0.7$, as seen in Figure 4.2, where the measured fluctuations are maximum (see Figure 5.5), which is outside the toroidal field reversal surface. The computed linear growth rates at $r/a = 0.8$ are shown in Figure 4.3 versus the inverse local normalized density gradient scale length, $R_0/L_n = -\frac{R_0}{n_0} \frac{\partial n_0}{\partial r}$, which is a variable parameter in the GENE modeling describing the instability drive strength. The growth rates are normalized to a characteristic sound speed crossing time, R_0/c_s . A critical inverse normalized density gradient scale length threshold for linear instability, $R_0/L_n \approx 20$, is observed. This critical gradient required for TEM turbulence is significantly larger than the critical gradient for TEM turbulence in Tokamaks, which only require a critical gradient $R/L_{Te} \sim 6$ [81, 82, 83, 84]. Separating the contributions of passing and trapped particles shows the instability to be driven by trapped particles. Continuous growth rates and frequencies with wavenumbers and gradient scale lengths indicate that a single instability dominates linear growth. The turbulence generated by this instability is particularly important in toroidal fusion plasmas, and the behavior here is indicative of the case studies performed by Carmody in Reference [14] in key aspects such as the impact of residual long-wavelength magnetic fluctuations on zonal flows in nonlinearly saturated turbulence.

These growth rate calculations were repeated at several radial locations from a reconstruction of an ensemble of 200 kA PPCD plasmas, calculated by MSTFit [85]. The growth rates, shown in Figure 4.4, show that the peak growth rates are located in the edge of the plasma at $r/a \approx 0.84$, where equilibrium gradients are strongest, at a normalized wavenumber of $k_y\rho_s \approx 0.5$. In the interior of the plasma, at $r/a \approx 0.56$, where the gradients are weak and there is little free energy

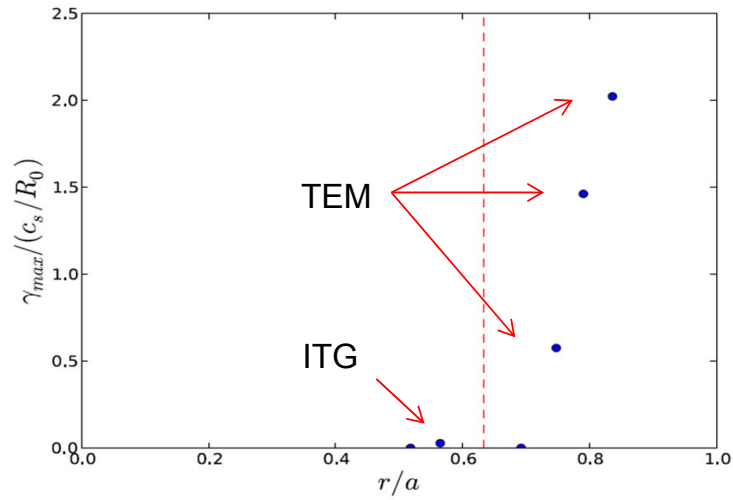


Figure 4.2 Linear growth rates at several radial locations as computed in GENE, given a 200 kA PPCD equilibrium. (Reproduced from Carmody et al., Ref. [14])

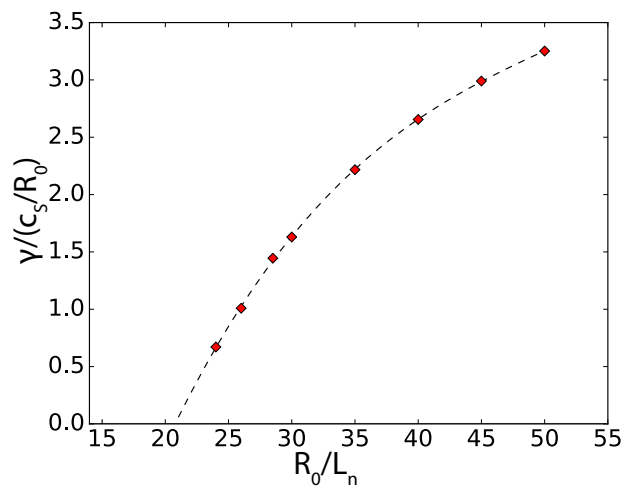


Figure 4.3 Linear growth rates for TEM at $r/a = 0.8$ versus the inverse normalized density gradient scale length as computed in GENE. (Reproduced from Williams et al., Ref. [57])

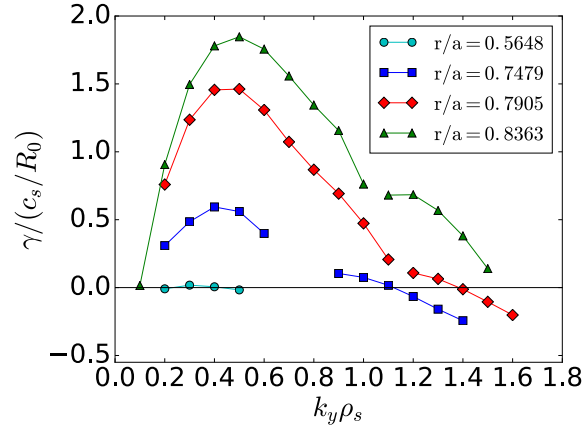


Figure 4.4 Linear growth rates for TEM at several radial locations versus the normalized wavenumber as computed in GENE. (Reproduced from Williams et al., Ref. [57])

available for instabilities, the growth rates are quite low, as expected. The scaling of this instability with the inverse normalized density gradient scale length and the location of the peak growth rates are indicative of TEM-type turbulence.

By adjusting the relative strength of the density gradient scale length and the ion temperature gradient scale length, defined as $\eta \equiv L_n/L_{T_i}$, the drive of TEM and ITG instabilities was explored. If the normalized ion temperature gradient scale length exceeds a particular threshold, namely $\eta \approx 1.2 - 1.4$, then ITG was found to be the fastest growing mode. If η did not exceed this threshold, then TEM was found to be the fastest growing mode. At the border of this threshold, a hybrid (combination of multiple present modes) mode was found to be excited [14]. In principle, this phenomena can be explored experimentally by looking at several plasma equilibria where the relative strength of the gradients changes, such as for crash-heated PPCD where the ion temperature gradient can be much larger, or for “moderate-confinement” PPCD, where the density gradient is weaker.

Due to their inherent trapped-particle nature, TEMs are localized to the low-field side of toroidal confinement devices. This behavior has been confirmed in linear simulations, in which the TEM eigenmode is plotted against a field-line line following coordinate θ , which is primarily

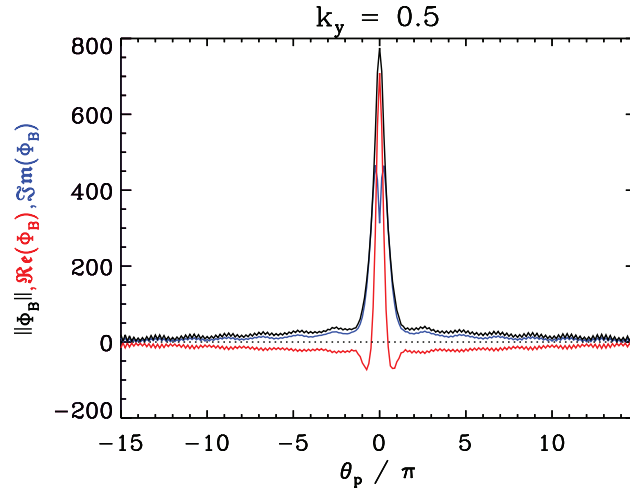


Figure 4.5 Structure of the TEM in the RFP. The TEM has ballooning structure in Φ across a field aligned coordinate θ , which is dominantly poloidal in the region of interest. (courtesy Zach Williams)

poloidal in the region of interest. As seen in Figure 4.5, the mode structure peaks at $\theta = 0$ (corresponding to the outboard midplane), and falls off rapidly towards the inboard side. A perturbation with this structure is a “ballooning” mode [86].

4.4 Nonlinear GENE results

Turbulence and transport in PPCD discharges were modeled using nonlinear flux-tube GENE simulations. Initial calculations based on PPCD equilibria produced negligible transport, indicated by the dashed line in Figure 4.6, with electron heat transport conductivity on the order of $\chi_e \sim 10^{-4} \text{ m}^2/\text{s}$ for MST relevant parameters. This is due to very strong zonal flows, seen in Figure 4.7(a), that are nonlinearly generated, lowering the saturation level for the instability. The impact of the zonal flow can be seen in Figure 4.8 in the purple triangles, which shows a large upshift in the critical gradient required for TEM transport relative to the threshold of the linear instability. This upshift is known as the Dimits shift [87]. The zonal flow, acting as a regulator of turbulence, increases the pressure gradient required to produce TEM turbulence.

Because of the large discrepancy between the GENE calculated [57] and experimentally measured [30] values of the electron heat conductivity χ_e in the area of interest, it was posited that

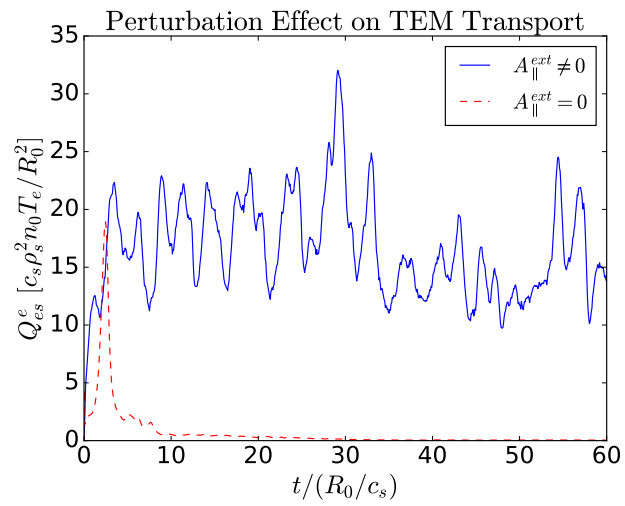


Figure 4.6 Heat transport in simulated 200 kA PPCD plasmas with (*blue*) and without (*red*) an enforced magnetic perturbation on the scale of residual global magnetic tearing. (Reproduced from Williams et al., Ref. [57])

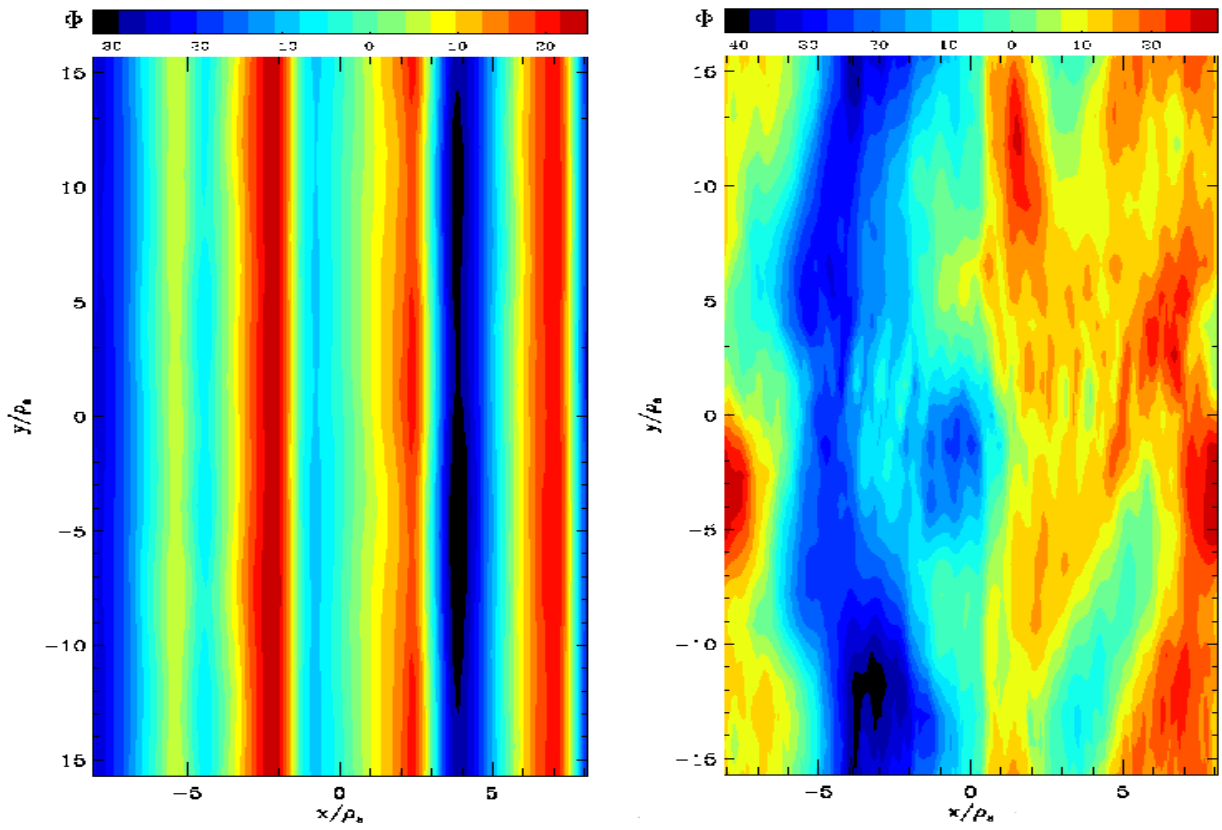


Figure 4.7 Electrostatic potential with and without enforced residual magnetic fluctuations. Without the ad hoc magnetic perturbations, zonal flows form sheets in the electrostatic potential that act as a transport barrier. With the magnetic perturbation, the zonal flows are “shorted out”, and become broader. (Reproduced from Williams et al., Ref. [57])

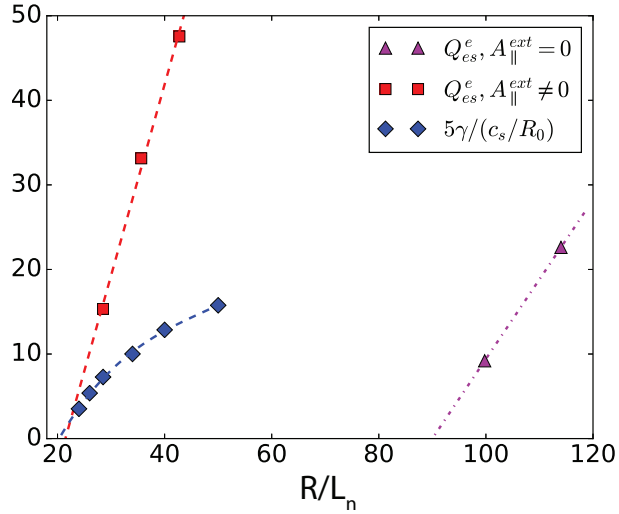


Figure 4.8 Linear growth rates (*blue*), nonlinear heat flux without an external B_r (*purple*), and nonlinear heat flux with an external B_r (*red*) for TEM at $r/a = 0.8$ versus the inverse normalized density gradient scale length as computed in GENE. (Reproduced from Williams et al., Ref. [57])

the simulation may be missing some physics. Namely, the presence of residual magnetic tearing fluctuations were not considered in the simulation. These residual magnetic fluctuations, discussed in Section 1.2, were found to have an important impact on TEM turbulence. In order to approximate these tearing fluctuations without having to model the entire plasma volume, an ad-hoc, tearing-parity, constant-in-time, parallel vector potential A_{\parallel} perturbation was implemented in the simulation volume. The inclusion of this perturbation degrades the zonal flow activity, seen in Figure 4.7(b). A radial magnetic perturbation, modeled after the ad-hoc A_{\parallel} in Figure 4.9 in the x direction, allows electron streaming along field lines to travel to different flux surfaces, effectively shorting out the zonal flows. The impact of the zonal flow degradation can be seen in the Dimits shift in Figure 4.8 for the $A_{\parallel} \neq 0$ case, where the critical gradient for TEM turbulence is reduced to a linear-like level. The zonal flow degradation has a strong effect on the electrostatic heat flux Q_{es}^e , seen in Figure 4.6 in the $A_{\parallel} \neq 0$ case, which increases to levels comparable to the experiment. The calculated diffusivity ($\chi_e \sim 10 \text{ m}^2/\text{s}$) comes within 30% of the experimental value [30, 57].

Simulations for “medium-confinement” 200 kA PPCD discharges, which will be discussed experimentally in Subsection 5.3.3, tend to have stronger temperature gradients and weaker density

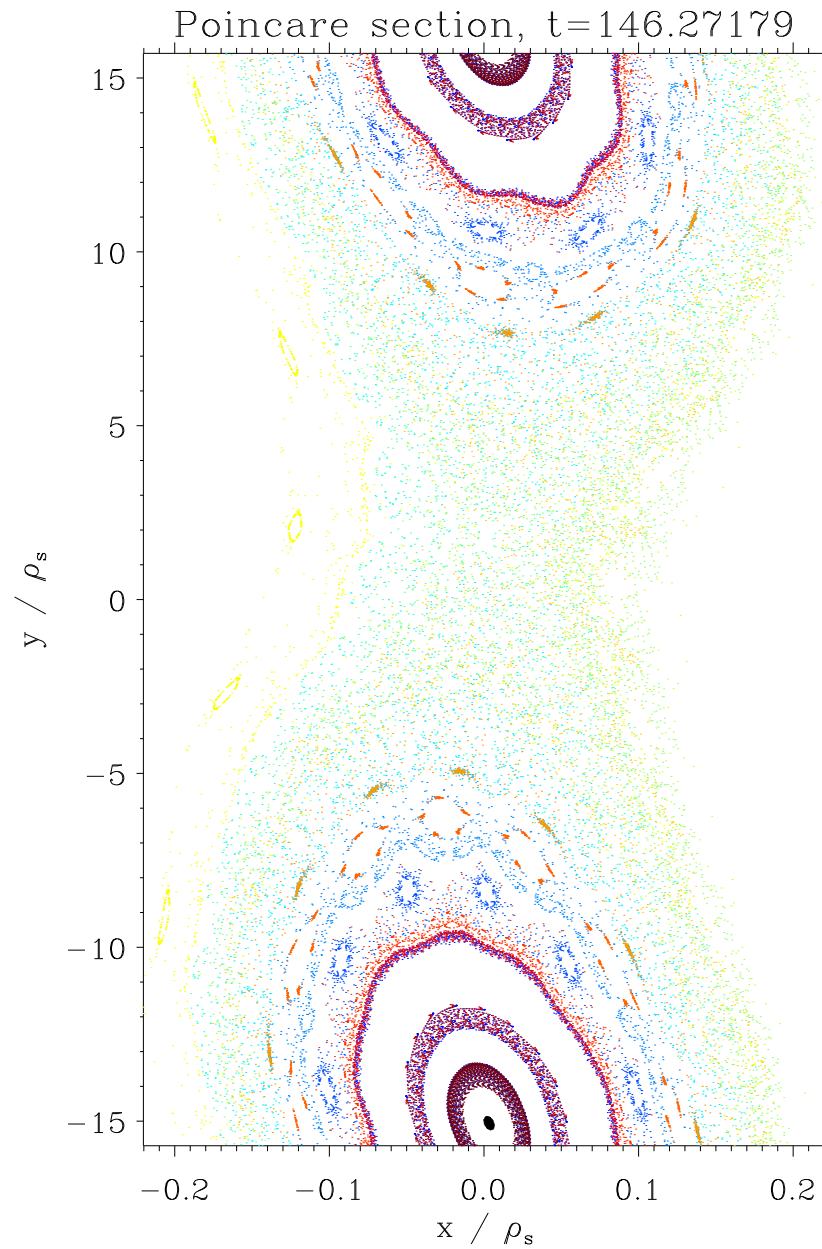


Figure 4.9 Puncture plot of magnetic fluctuations outside the reversal surface, as calculated by GENE. Overlapping magnetic islands can form outside the reversal surface, allowing for rapid radial transport. (courtesy Zach Williams)

gradients, have also been done and resulted in an equilibrium that is expected to be unstable to ITG turbulence. For this discharge equilibrium, calculated transport properties were on the same order as experimental transport without the inclusion of residual magnetic tearing fluctuations. When the magnetic fluctuations were included, the transport increased a little, but were less impactful than in the TEM dominated discharge. While transport in the TEM dominated equilibrium is increased by orders of magnitude by the inclusion of a tearing perturbation, the transport in the ITG dominated plasma equilibrium only changes by approximately a factor of two for an identical tearing perturbation. The ITG dominated discharge also only shows a very small Dimits shift, revealing a very different role of zonal flow saturation in the two regimes. This difference in the two regimes is quite interesting, and a topic of current investigation [57].

4.5 Summary

The gyrokinetic code GENE has been used to simulate RFP plasmas using several MST equilibria from MSTfit. Linear simulations have predicted unstable density gradient driven TEM fluctuations in 200 kA PPCD equilibria. This instability has critical normalized inverse density gradient scale lengths on the order of $R_0/L_n \approx 20$. Simulations on other PPCD equilibria have predicted that the identity of the fastest growing mode present in the plasma depends on the relative strength of the density gradient scale length and the ion temperature gradient scale length, with stronger inverse ion temperature gradient scale lengths driving an ITG instability. Initial nonlinear GENE simulations of the 200 kA PPCD plasmas equilibria predicted strong zonal flows driven by TEM turbulence, limiting transport properties significantly. This was due to absence in the simulations of magnetic fluctuations still present in PPCD plasmas. More precisely, GENE does not operate with any current gradients present in the plasma, which is the free energy source for magnetic tearing mode perturbations. The addition of ad hoc magnetic fluctuations resulted in disruption of the zonal flows, increasing transport to levels comparable to those seen experimentally. Further cooperation between the GENE group and the MST experimental team may provide opportunities for validation of the GENE code in the RFP geometry.

Chapter 5

Electron Density Fluctuations in RFP Plasmas

Measuring density fluctuations is an integral part of measuring thermal transport characteristics. Using the FIR interferometer/polarimeter system described in Chapter 2, line-integrated density fluctuations can be measured. Additionally, the FIR system can measure the line-integrated equilibrium density, and by using an Abel inversion, the equilibrium density along the mid-plane of the plasma. By using the toroidal chord separation, wavenumber information can be measured via the density fluctuation power spectrum, as described in Appendix A. Measuring the density fluctuations in several plasma equilibria can give a glimpse into the thermal transport characteristics of these plasmas, but will not reveal the whole picture, due to the lack of velocity fluctuation measurements, whose phase relative to the density and temperature fluctuations is also important to the particle and thermal fluxes.

This chapter will describe density fluctuations in standard plasmas in Section 5.1 and 200 kA PPCD plasmas in Section 5.2, as well as the dependence of high frequency density fluctuations on the electron density gradient. In Section 5.2.2, the wavenumber associated with high frequency density fluctuations will be explored. Section 5.2.3 will discuss residual magnetic perturbations present in 200 kA PPCD plasmas both inside and outside the reversal surface. Other plasma equilibria will be discussed in Section 5.3, including 400 kA PPCD plasmas, crash-heated 500 kA plasmas, and “medium-confinement” 200 kA PPCD plasmas. Aliasing of the wavenumber spectrum in these plasma equilibria helped motivate the recent FIR mixer upgrade, and preliminary data from these mixers will be presented in Section 5.4.

5.1 Density fluctuations in standard plasmas

A considerable amount of research has been done on density fluctuations in standard RFP plasma operation, particularly in regard to the global magnetic tearing mode [35, 88]. In a standard sawtooth plasma discharge, the density fluctuation amplitude can range from 15 – 40% of the equilibrium value from the edge to the core, depending on the time relative to the sawtooth crash. The evolution of the density fluctuation power spectrum for an ensemble of 173 sawtooth crashes in 200 kA standard plasmas is shown in Fig. 5.1. From the figure it is seen that the density fluctuations are initially very low frequency, and as the sawtooth crash occurs, there is a broadening of the density fluctuation power spectrum to higher frequencies, followed by a decrease of broadband density fluctuation power back to the lower frequency scales. The increase in relative density fluctuation power is strongest in the edge of the plasma, as seen in Figure 5.1(c), which shows the density fluctuation power spectrum measured at an impact parameter of $x \equiv R - R_0 = 0.43$ m. The fluctuation power is up to an order of magnitude larger in the edge of the plasma than in the core of the plasma (note the difference in scales between plots), as seen in Figure 5.1(a), which is measured at $x = 0.06$ m.

Standard discharges have a large number of magnetic tearing modes influencing the plasma. This can be seen in the frequency-wavenumber power spectrum, as shown in Figure 5.2, which is taken for an ensemble of 200 kA standard plasmas from edge FIR chords. The coherent fluctuations are low frequency ($\lesssim 20$ kHz), and broad in wavenumber, spanning from approximately -0.1 cm^{-1} to 0.05 cm^{-1} . Higher frequency density fluctuations (> 20 kHz) are incoherent in these plasmas, indicative of a cascade of energy from low frequency to higher frequencies, seen in the broad tearing-dominated curve of Figure 5.3. These broadband density fluctuations are strongly correlated with tearing mode dynamics, including nonlinear three-wave interactions that energize stable modes and generate broadband turbulence [89].

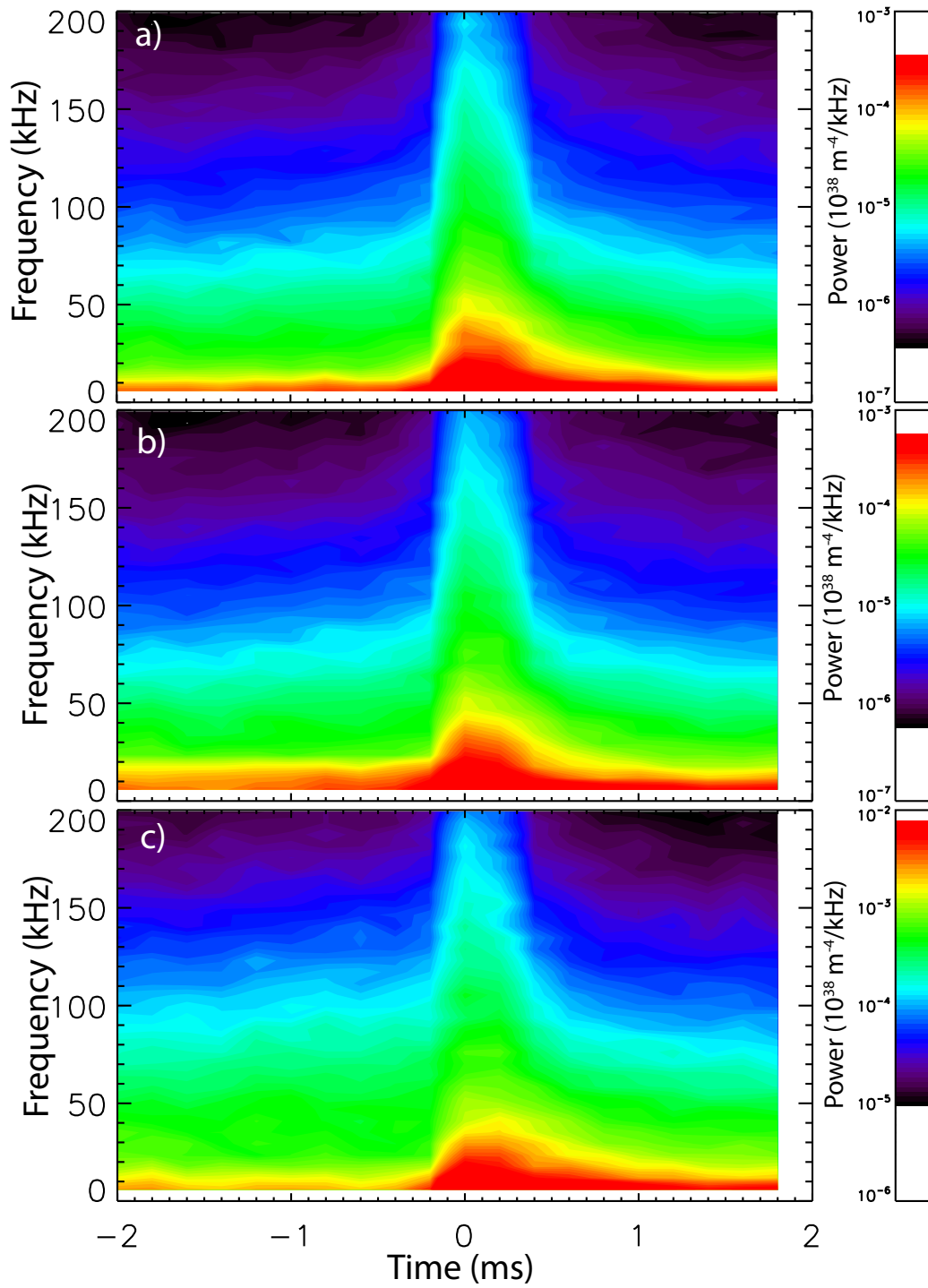


Figure 5.1 Density fluctuation power spectrum as a function of time over an ensemble of 173 sawtooth crashes at 3 impact parameters: $x = 0.06$ m (a), $x = 0.21$ m (b), and $x = 0.43$ m (c)

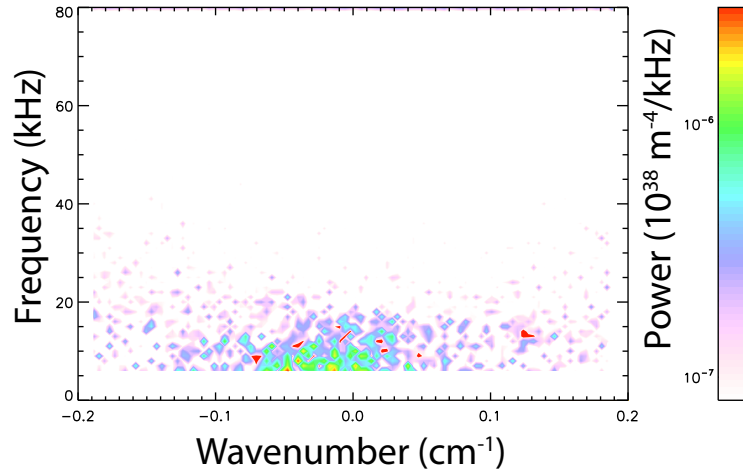


Figure 5.2 Frequency-wavenumber power spectrum for the density fluctuations in the edge of standard plasmas for an ensemble of 173 sawteeth in 200 kA standard plasmas, taken 1 ms after the sawtooth crash.

5.2 Description of TEM-like density fluctuations in 200 kA PPCD plasmas

5.2.1 Equilibrium and fluctuating electron density characteristics

By suppressing the tearing modes with PPCD, the stable tearing modes are no longer energized, and broadband turbulence is suppressed. Therefore, new modes may emerge from the plasma equilibrium, or may be driven unstable by the larger pressure gradients in these plasmas. By exploring these new instabilities, the characteristics of these plasmas can be described.

Using the FIR interferometer, the time-dependent electron density fluctuation power spectrum, as well as the equilibrium density and density gradient can be measured and used to describe instabilities in the electron density present in these plasmas. Figure 5.3 shows ensemble-averaged frequency power spectra for line-integrated electron density fluctuations measured in 200 kA tearing-dominated and improved-confinement plasma conditions. For both regimes, the data was measured in the edge of the plasma at impact parameter of $x = 0.43$ m ($r/a = 0.86$) relative to the geometric axis, R_0 . The power spectrum for tearing-dominated conditions is for 1 ms time slices taken before PPCD is active, $t_{start} = 9.5 - 10.5$ ms, and the spectrum for PPCD improved confinement conditions is for 1 ms time slices near the end of the inductive control phase when the density and temperature attain their maximum values, $t_{end} \approx 18 - 22$ ms. The typical frequency range for the dominant $m = 1$, $n \gtrsim 2R_0/a \sim 6$ tearing modes in the standard RFP spectrum is $f \approx 10 - 30$ kHz, where n is the toroidal mode number. As anticipated, the density fluctuations are reduced at most frequencies with PPCD, however, Figure 5.3 shows an emergent spectral peak appearing at frequency $f \sim 50$ kHz. This fluctuation is found to have characteristics comparable to the TEM instability described computationally in Chapter 4.

By looking at the density fluctuation power as PPCD evolves, structures in the electron density fluctuations may become easier to identify with regard to the equilibrium evolution. A spectrogram for the evolution of the line-integrated density fluctuation power at $x = 0.43$ m for an ensemble-average of 142 PPCD plasmas is shown in Figure 5.4(a). The PPCD programming is initiated at $t = 10$ ms, which is about the time of peak I_p following plasma formation at $t = 0$ ms. At 10 ms the dominant density fluctuations are associated with tearing fluctuations, i.e., the ‘tearing dominated’

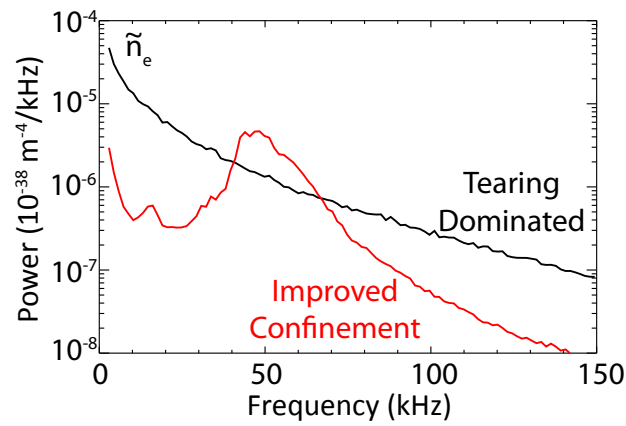


Figure 5.3 Frequency power spectra for line-integrated electron density fluctuations in 200 kA Standard (*black*) and PPCD (*red*) plasma conditions. Density fluctuations are suppressed during PPCD, and a new spectral feature emerges. (Reproduced from Duff, et. al, Ref. [37])

spectrum in Figure 5.3. As PPCD sets in, tearing fluctuations subside, and a new spectral peak emerges at higher frequencies. These emergent density fluctuations are observed in improved confinement discharges over MST's full range of plasma currents, but the frequency spectral width of the new peak is narrowest for 200 kA PPCD plasmas. Maximum plasma pressure is obtained at the end of the PPCD control phase [10], which is followed by a return to tearing-dominated conditions at $t \gtrsim 22$ ms.

The amplitude of the emergent density fluctuations is peaked in the outboard region of the plasma where the gradient in the equilibrium (flux-surface-averaged) density is the strongest. Figure 5.5 shows the ensemble-averaged amplitude of the line-integrated density fluctuations, $\langle \tilde{n}_e \rangle_x$, for each interferometer chord, R_i , integrated over the frequency band 40 – 65 kHz to isolate the emergent fluctuations. Angle brackets $\langle \rangle$ denote an ensemble average. The ensemble average of the Abel-inverted density profiles, $\langle n_e(r) \rangle$, at 20 ms mapped to the mid-plane ($Z = 0$) is also plotted in Figure 5.5. The fluctuation power is strongest in the outboard side of the plasma, which is consistent with a ballooning parity mode, as described in Section 4.3, and as seen in Figure 4.5. The time evolution of the density gradient, $\langle |\nabla n_e(r, t)| \rangle$, is plotted in Figure 5.4(b) for the outer region of the plasma. The density gradient is calculated from an Abel inversion of the line-integrated density profile taken from the FIR diagnostic. The emergence of the density fluctuation, shown in Figure 5.4(a), coincides with the sharp increase in $|\nabla n_e|$ during PPCD, shown in Figure 5.4(b).

The emergent density fluctuations exhibit a clear density-gradient threshold behavior, as shown in Figure 5.6. The fluctuation amplitude varies shot-to-shot, depending on the degree of tearing suppression. The shot ensemble is binned according to the magnitude of the mean density gradient measured in each plasma. An inverse normalized gradient scale length characteristic of the strong-gradient region, $R_0 \langle |\nabla n_e|_{0.8} \rangle / \langle n_e \rangle_{0.8}$ is calculated for each bin, where $|\nabla n_e|_{0.8}$ is the magnitude of the density gradient at $r/a = 0.8$, and n_e is the local density calculated from an Abel inversion of the FIR measured equilibrium density profile. Note that the local density gradient scale length, $L_n \equiv n_e(r) / |\nabla n_e|$, rapidly varies because the width of the strong-gradient region is comparable to L_n . The power in the emergent fluctuations, $\langle \tilde{n}_e^2 \rangle$, increases when the gradient exceeds the threshold $R_0 \langle |\nabla n_e|_{0.8} \rangle / \langle n_e \rangle_{0.8} \geq 18$, as seen in Figure 5.6. The time evolution of $R_0 \langle |\nabla n_e|_{0.8} \rangle / \langle n_e \rangle_{0.8}$

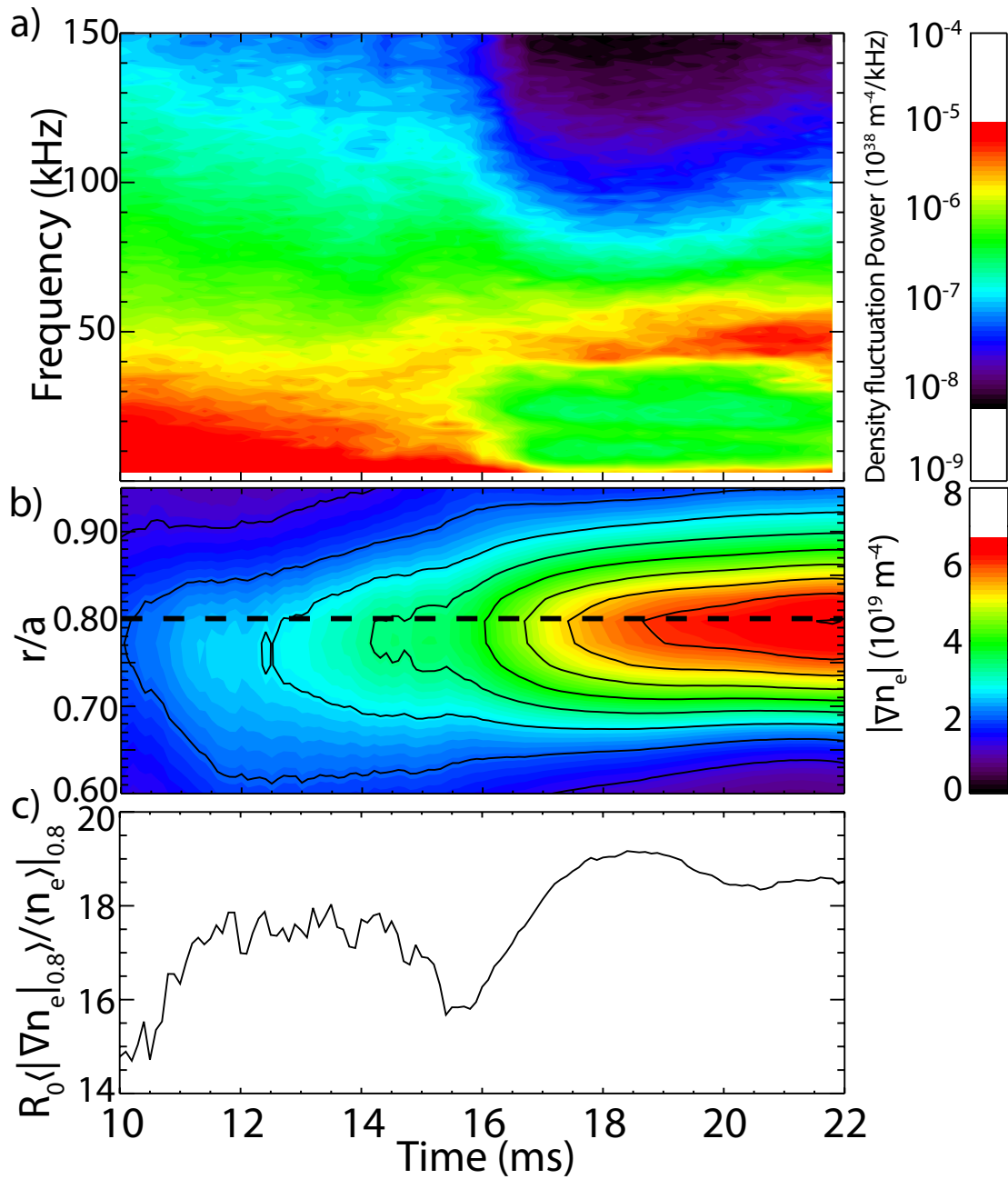


Figure 5.4 Evolution of (a) the line-integrated electron density fluctuation power at $x = 0.43 \text{ m}$ and (b) the equilibrium density gradient for an ensemble of PPCD plasmas taken from an Abel inversion of the FIR measured line-averaged density profile. The evolution of the inverse normalized density gradient scale length, $R_0 \langle |\nabla n_e|_{0.8} \rangle / \langle n_e \rangle_{0.8}$, for radius $r/a = 0.8$ is shown in (c). (Reproduced from Duff, et. al, Ref. [37])

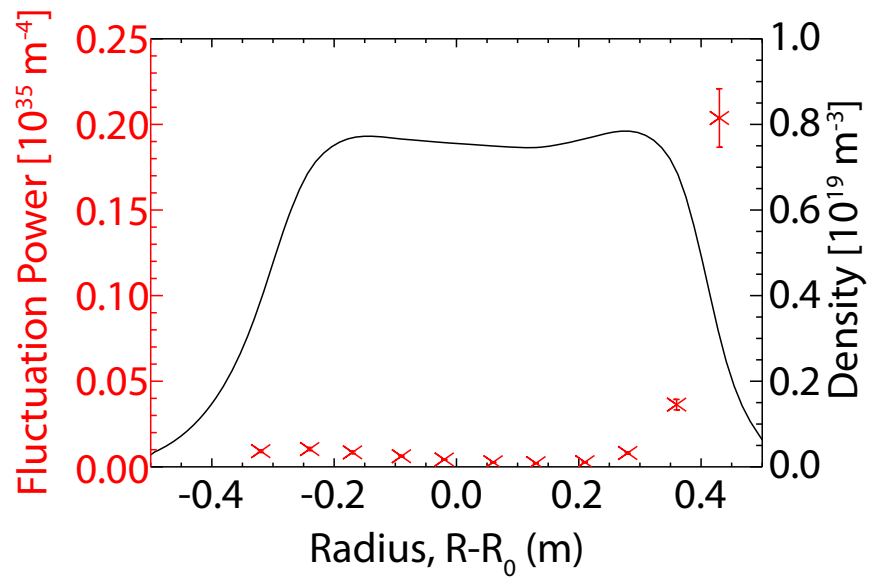


Figure 5.5 Ensemble-average of Abel-inverted density profiles on mid-plane at 20 ms (*black*) and ensemble-averaged amplitude of line-integrated density fluctuations frequency integrated from 40-65 kHz (*red*). (Reproduced from Duff et. al, Ref. [37])

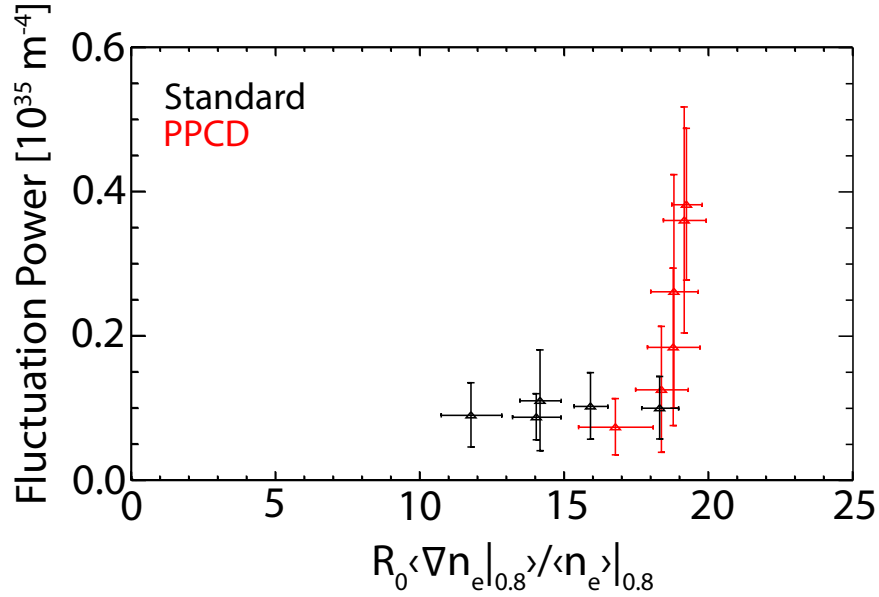


Figure 5.6 Line-integrated density fluctuation power, $\langle \tilde{n}_e^2 \rangle$, (40-60 kHz) measured at impact parameter $x = 0.43$ m versus $R_0 \langle |\nabla n_e|_{0.8} \rangle / \langle n_e \rangle_{0.8}$. (Reproduced from Duff, et. al, Ref. [37])

(averaged over the full ensemble) is plotted in Fig. 5.4(c), which shows the gradient scale length increases by $\sim 20\%$ as PPCD activates. Similar analysis for the electron temperature gradient, $|\nabla T_e|$, does not exhibit clear critical-gradient behavior, although the Thomson scattering measurements in the outer region of MST plasmas presently have relatively large uncertainty due to stray laser light issues. Efforts to improve Thomson scattering are underway. Ion temperature measurements were not available for these plasmas, but the ion temperature profile is typically assumed to be some fraction of the electron temperature profile.

5.2.2 Wavenumber analysis

The toroidal wavelength of the fluctuations is determined by the phase shift between measurements along the two outboard-most interferometer chords that are separated 5° toroidally ($R_0 \Delta\varphi = 13$ cm). An in-depth description of the method for this calculation is outlined in Appendix A. These chords are tangent to magnetic surfaces that have safety factor $q \Rightarrow 0$ and are therefore most sensitive to fluctuations with $ak_\theta \approx ak_\parallel \lesssim 1$. The two-point-correlation frequency-wavenumber power spectrum at $t = 20$ ms is shown in Figure 5.7. In the $f \approx 50$ kHz range where

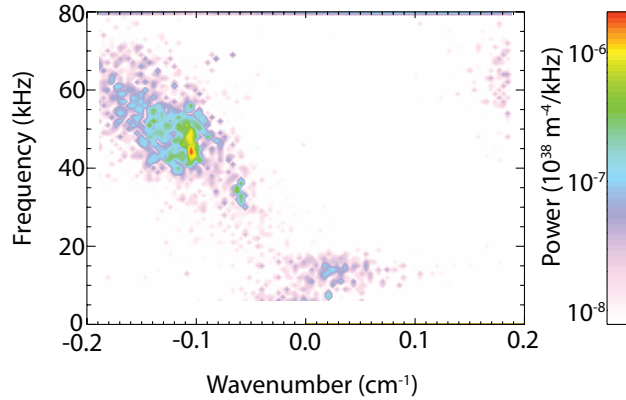


Figure 5.7 Frequency-wavenumber power spectrum of the line-integrated electron density fluctuations between FIR chords at $x = 0.36, 0.43$ m at 20 ms. Positive (negative) wavenumber corresponds to wave propagation in the ion (electron) diamagnetic drift direction. (Reproduced from Duff, et. al, Ref. [37])

the emergent fluctuations are largest, the toroidal wavenumbers range from $k_\varphi \approx -0.1 \text{ cm}^{-1}$ to $k_\varphi \approx -0.2 \text{ cm}^{-1}$, where the minus sign corresponds to wave propagation in the electron diamagnetic drift direction. This is opposite the direction of propagation of the residual $f \sim 15$ kHz core-resonant tearing modes, $k_\varphi \approx 0.04 \text{ cm}^{-1}$ ($n \approx 6$), which acquire finite frequency from plasma flow. The density fluctuations associated with residual tearing modes are still resolved in Figure 5.7. By fitting a line to the weighted mean of the $S(k, \omega)$ plot, shown in Figure 5.8, the group velocity v_{gr} is found to range from ~ -2 km/s to ~ -4 km/s, depending on the maximum and minimum wavenumber used for the fit. The expected drift velocity, $v_e^* = T_{e,0} \nabla n_e / (e|B|n_e)$ for the relevant plasma equilibrium is ~ 10 km/s, which gives some indication of what the Doppler shift may be. The toroidal plasma flow is small near $r/a = 0.8$ [90, 91], so the Doppler shift of the emergent fluctuations is small and, if nonzero, likely to also be in the ion drift direction.

While it is assumed the largest component of the wavenumber is toroidal, the FIR chords used for the measurement do have a radial separation. The same phase shift analysis for the wavenumber can be used between adjacent chords at the same toroidal angle for a spectrum dominated by the radial and poloidal wavenumbers, or the extreme inboard and outboard chords for a primarily poloidally dominated spectrum. For these plasma equilibria, chords with zero toroidal separation

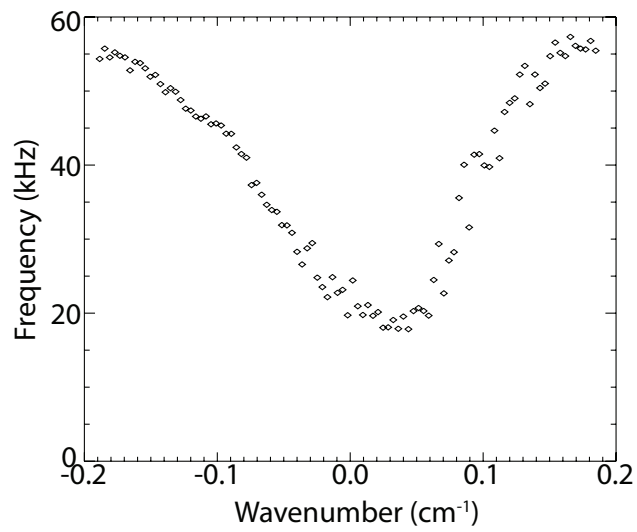


Figure 5.8 Weighted mean of the spectral power for each available wavenumber. For the spectral power between wavenumbers ~ -0.15 to ~ -0.05 cm^{-1} , a linear fit can be used to estimate the group velocity of the emergent density fluctuation.

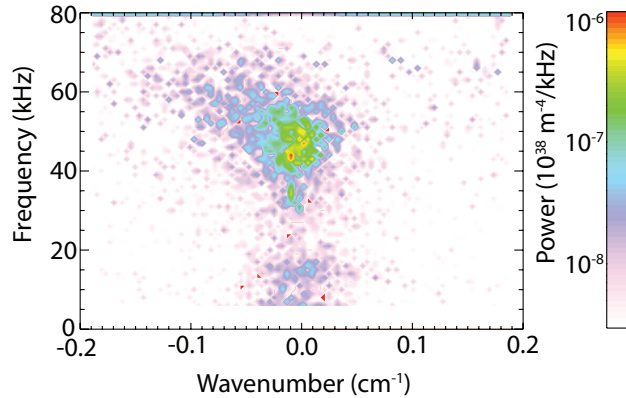


Figure 5.9 Frequency-wavenumber power spectrum of the line-integrated electron density fluctuations at between FIR chords at $x = 0.28, 0.43$ m at 20 ms.

show very high coherence for the emergent fluctuation, but a wavenumber of $k \ll 1 \text{ cm}^{-1}$ as seen in Figure 5.9, indicating the radial wavenumber is small.

5.2.3 Residual magnetic fluctuations

Residual magnetic fluctuations can potentially have very important transport implications in PPCD plasmas. The nonlinear gyrokinetic simulations discussed in Section 4.4 have shown that magnetic perturbations can degrade zonal flows, reducing confinement. Using a demodulation technique developed by Fimognari [38], residual magnetic fluctuation power can be estimated. For each MST shot, a spatial Fourier decomposition is routinely performed using the 16 coil poloidal array and 64 B_T coil toroidal array. These signals have large fluctuations on top of the slowly varying component, due to the presence of both stationary and rotating components of the modes. Decomposition of the toroidal array signals separates out positive, negative, and zero frequency components corresponding to magnetic fluctuations having phase velocity in the positive or negative toroidal direction or remaining stationary. This process uses temporal FFT analysis of the mode amplitudes to determine the sign of the frequency, as discussed in reference [38]. Modes resonant in the core are negative frequency (ion diamagnetic direction), but there is evidence for toroidal flow reversed in the extreme edge of standard RFP plasmas, as noted in [38]. In deeply reversed plasmas, such as PPCD discharges discussed here, modes with moderate toroidal mode

number, $|n| \sim 10$, can be resonant both in the core and the extreme edge. We use the demodulation method to isolate both positive and negative phase velocities to help reveal this possibility. In the region of the plasma where the TEM instability is observed, the plasma velocity is small, but it could be counter to the core plasma flow. While the magnetic fluctuation resonant at $r/a \approx 0.8$ is not precisely determined, this method still provides an estimate of the magnetic fluctuations for use in calculating the stochastic electron heat conductivity.

As noted in Section 1.2, and seen in Figure 1.5, during PPCD the amplitude of the magnetic tearing modes is suppressed significantly, but they do not disappear completely. In particular, the $n = 6 - 8$ modes have sizable amplitude. The magnetic fluctuation spectra for an ensemble of 200 kA PPCD plasmas were separated via the demodulation code, as seen in Figure 5.10 for positive frequency modes, and Figure 5.11 for negative frequency modes. In negative frequency, the poloidal and toroidal magnetic fluctuation spectrum is peaked at the $n = 6$ mode, and falls off significantly for all other modes. The magnetic fluctuation amplitude associated with these modes is quite low, peaked at $\sim 1 - 2$ G for the $n = 6$ mode, and dropping to < 0.2 G for broadband toroidal modes. For the positive frequency modes, Figure 5.11 shows a broader, lower amplitude magnetic fluctuation spectrum. The peak for the magnetic amplitude spectrum is at $n = 1$ for the poloidal fluctuations, and at $n = 2$ for the toroidal fluctuations. There is also a double peak feature, with the $n = 8 - 10$ fluctuation being the secondary peak for both the poloidal and toroidal directions. The amplitude for the magnetic fluctuation modes is still quite low, being < 0.45 G for all modes in the poloidal direction, and < 1.2 G in the toroidal direction. The higher mode number fluctuations drop off more slowly than for negative frequency, with the closely spaced mode numbers having comparable amplitudes. Therefore, the magnetic fluctuations in the edge of the plasma, where the TEM-like instability is measured, can be quite complex, with many closely spaced, comparable amplitude magnetic modes, which may result in significant overlap of magnetic islands and significant magnetic stochasticity.

The $f < 0$ magnetic measurements in these plasmas are quite important both to the experimental results, and the nonlinear GENE results, as discussed in Section 4.4. The toroidal magnetic fluctuations can be used to estimate the radial magnetic fluctuations, and therefore the stochastic

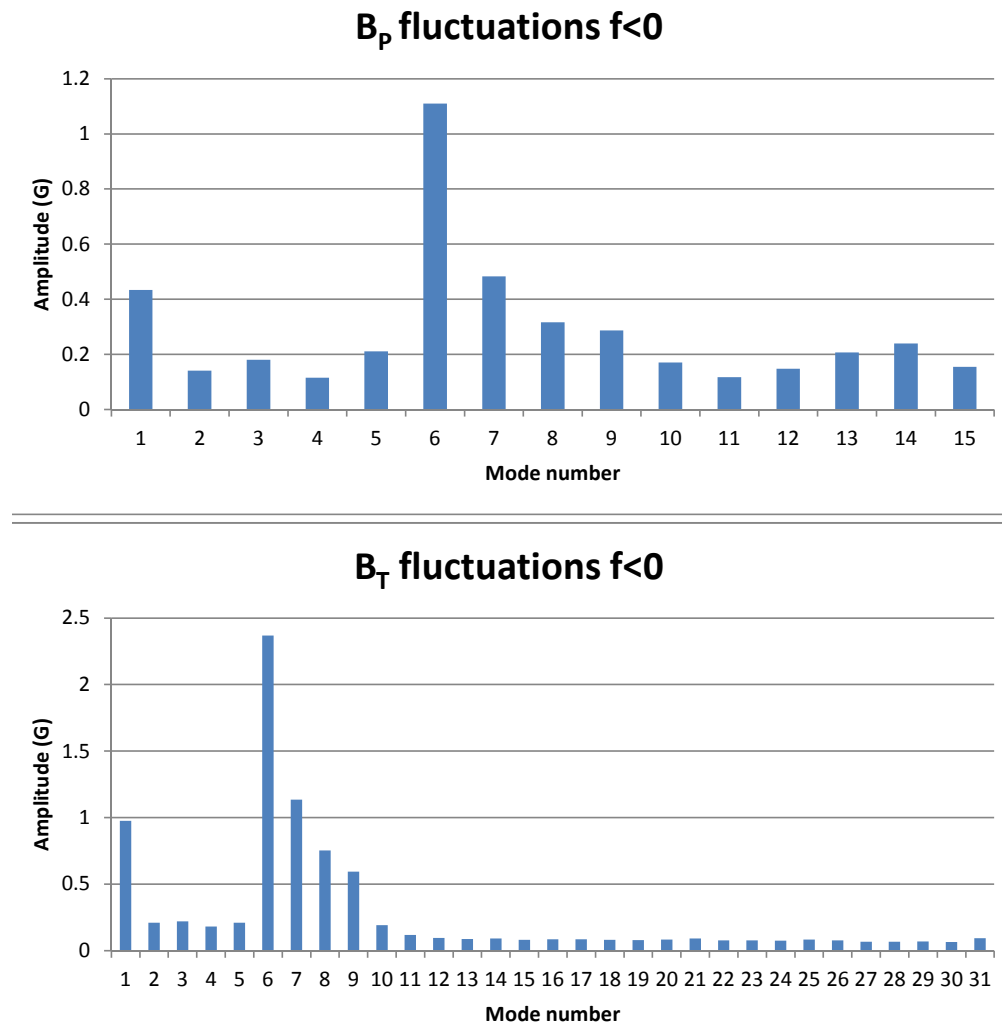


Figure 5.10 Mode amplitude for demodulated magnetic spectrum in the poloidal ($1 \leq n \leq 15$) and toroidal ($1 \leq n \leq 31$) directions for fluctuations resonant inside the reversal surface for an ensemble of 142 comparable 200 kA PPCD plasma discharges. During PPCD, the magnetic fluctuations are suppressed, and the $n=6$ mode dominates both spectra.

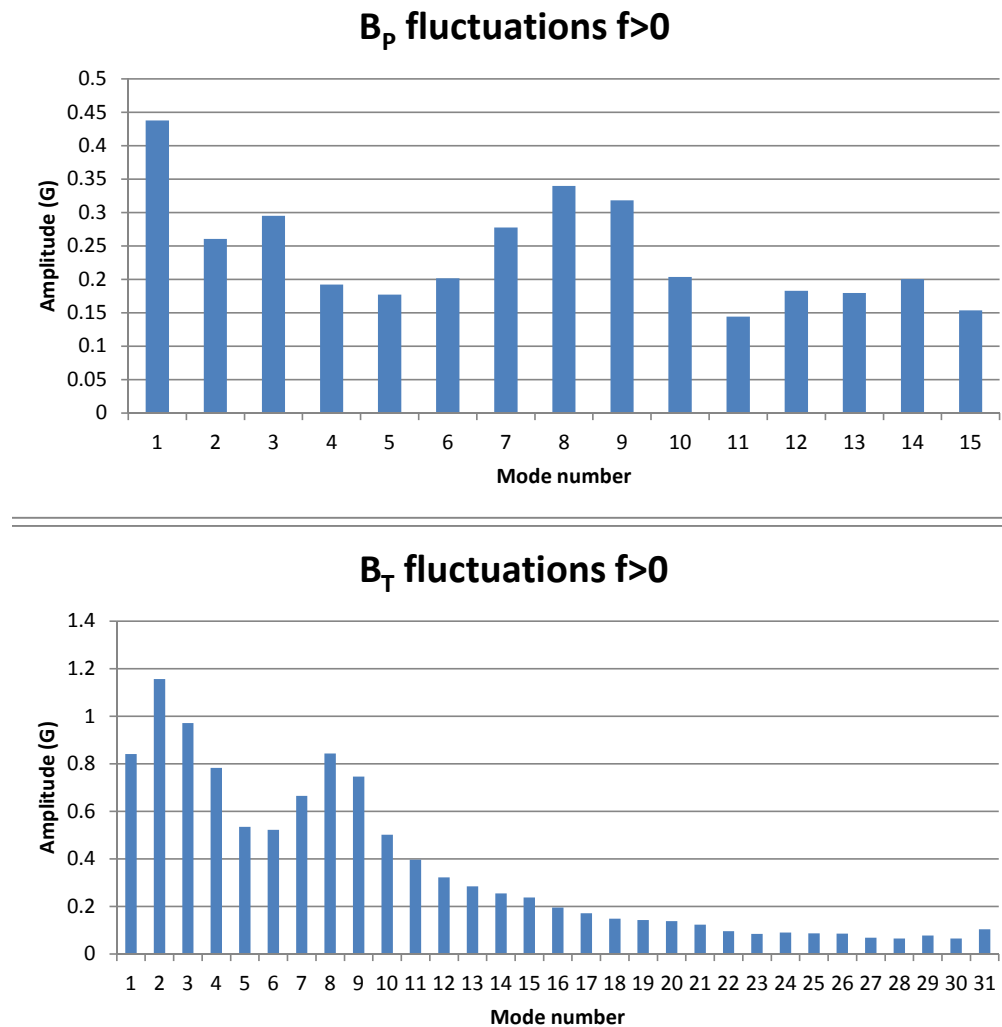


Figure 5.11 Mode amplitude for demodulated magnetic spectrum in the poloidal ($1 \leq n \leq 15$) and toroidal ($1 \leq n \leq 31$) directions for fluctuations resonant outside the reversal surface for an ensemble of 142 comparable 200 kA PPCD plasma discharges. The spectrum has a local peak at $n=8$, and is dominated by low n modes.

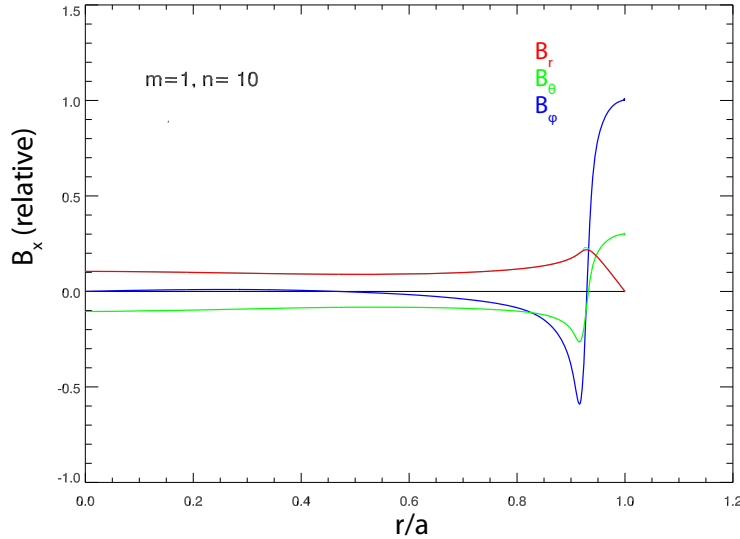


Figure 5.12 Profiles for the linear magnetic fluctuation eigenfunctions associated with the $m = 1, n = 10$ tearing mode, evaluated using RESTER. (Courtesy John Sarff)

electron heat conductivity, described in Section 3.1.1. This is done using profiles for B_ϕ , B_θ , and B_r for a given set of mode numbers calculated using RESTER [92], an example of which is given in Figure 5.12 for the $n = 10$ mode. RESTER is a linear stability code that determines which modes access free energy from the equilibrium field configuration, and is described by Sovinec in Ref. [92]. The RMS amplitude of B_ϕ for modes $m = 1, n = 8 - 12$ implies B_r is about ~ 0.7 G, while $|B| \sim 1000$ G, $L_{ac} \sim 1$ m, and $v_{th} = \sqrt{T_e/m} \sim 2000$ km/s. Using Equation 3.2, this results in a stochastic electron heat conductivity $\chi_{st,e} = v_T L_{ac} \frac{\langle \bar{b}_r \rangle^2}{B_0^2} \sim 1$ m²/s. Hence, the stochastic heat transport in the edge of the plasma is significantly lower than the measured heat transport [30], implying that there is another mechanism for the heat transport. GENE analysis discussed in Section 4.4 predicts that TEM turbulence could be responsible for much of the electron heat conductivity $\chi_e \approx 10$ m²/s in the region of interest.

5.3 Other plasma equilibria

High frequency fluctuations have been explored in several different plasma equilibria. The strongest control over the PPCD equilibrium is with the plasma current, so higher current plasmas

were explored, at 400 (Subsection 5.3.1) and 500 kA (Subsection 5.3.2). Additionally, “medium-confinement” 200 kA PPCD plasmas, where the tearing mode is not well suppressed, were explored in Subsection 5.3.3.

5.3.1 400kA PPCD plasmas

400 kA PPCD plasmas have been extensively studied for microturbulence. By increasing the plasma current, the equilibrium changes, potentially changing the characteristics of any observed microturbulence. In Figure 5.13(a), it is observed that the total density fluctuation power decreases as PPCD turns on from 10 to ~ 15 ms. Similarly to 200 kA PPCD plasma equilibria, a higher frequency density fluctuation emerges. This emergent fluctuation is higher frequency than the emergent fluctuations in 200 kA plasmas, at ~ 100 kHz in 400 kA discharges, versus ~ 50 kHz from the 200 kA discharges discussed previously. The 400 kA emergent fluctuation is also lower power than at lower current, and decreases in frequency as PPCD evolves, from ~ 100 kHz at ~ 16 ms down to ~ 50 kHz at ~ 20 ms. This down-shift in frequency may indicate that plasma velocity plays a more important role in these plasmas than in the lower current equilibrium. In Figure 5.13(b), the density gradient was found from inverted density profiles for these plasmas. The density gradient is lower magnitude than in the lower current equilibrium, but still significantly larger than in standard plasmas. The experimental proxy for the normalized inverse density gradient length, $R_0 \langle |\nabla n_e|_{0.75} \rangle / \langle \bar{n}_e \rangle_{0.75}$, is plotted in Figure 5.13(c). The normalized inverse density gradient scale length increases during PPCD by $\sim 75\%$, a significant increase over the course of PPCD. By integrating the fluctuation over a frequency range including the spectral feature, as seen in Figure 5.14, some information about the radial structure of the instability is revealed. This profile, measured near the end of the PPCD cycle, shows that the instability has drifted slightly towards the core of the plasma, peaking in power closer to the chord located at an impact parameter of $x = 36$ cm, as opposed to the 200 kA plasma case, where the instability peaked in the outboard edge of the plasma.

The spectral information in the spatial domain for this plasma equilibrium is more difficult to measure than in the lower current case. The wavenumber-frequency power spectrum shown in

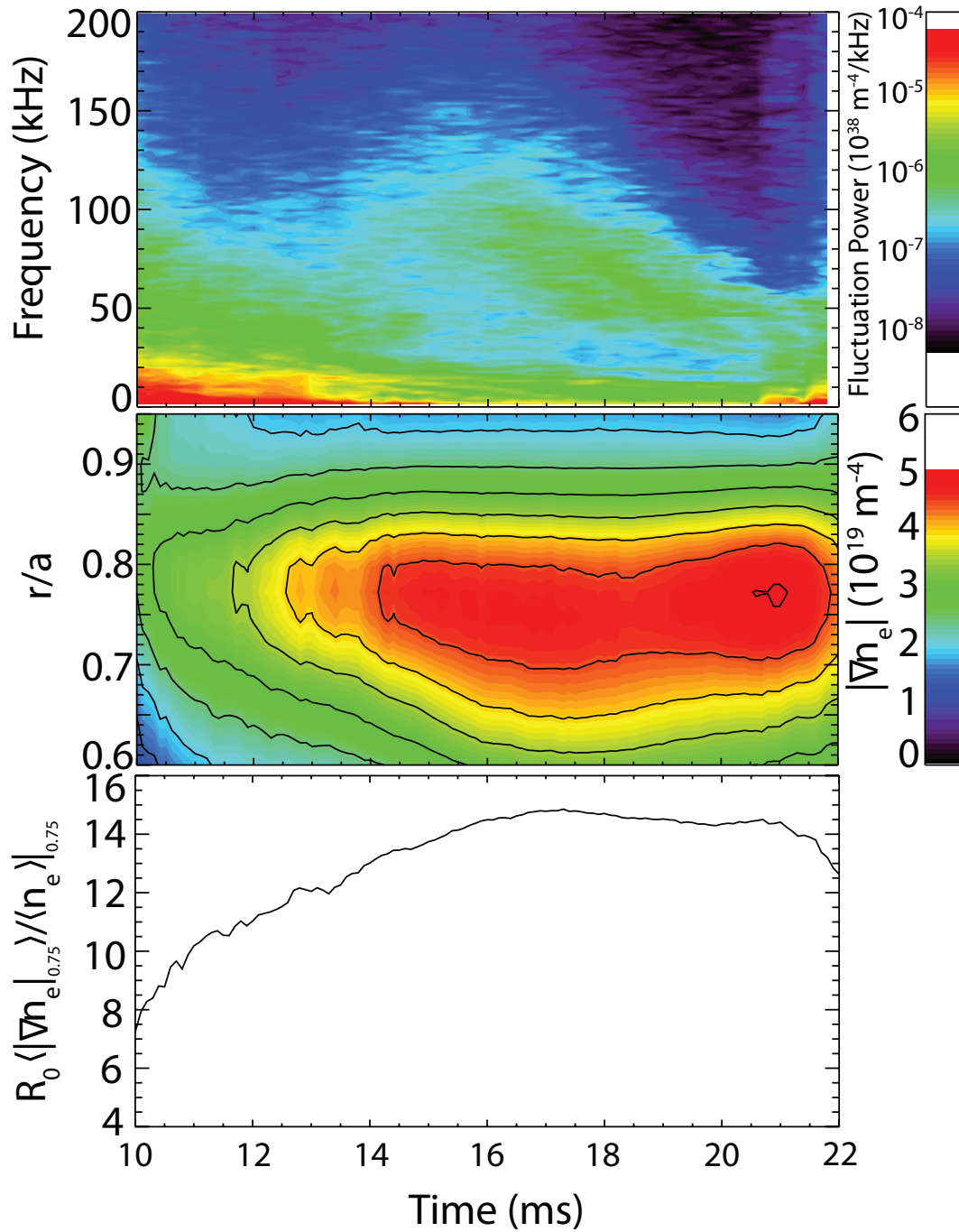


Figure 5.13 Evolution of (a) the line-integrated electron density fluctuation power at $x = 0.36 \text{ m}$ and (b) the equilibrium density gradient for an ensemble of 400 kA PPCD plasmas. The evolution of the inverse normalized density gradient scale length, $R_0 \langle |\nabla n_e|_{0.75} \rangle / \langle \bar{n}_e \rangle_{0.75}$, for radius $r/a = 0.75$ is shown in (c).

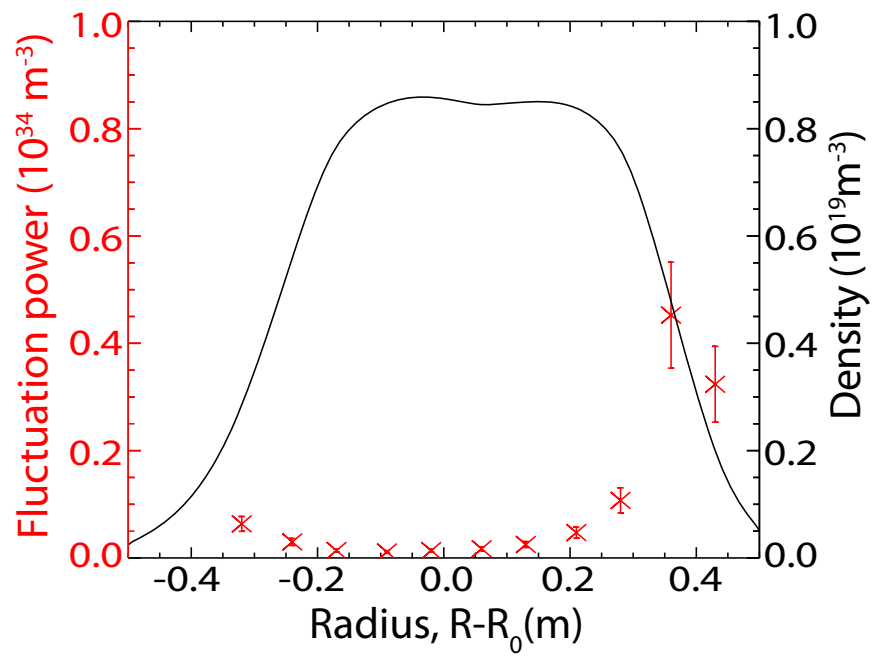


Figure 5.14 Ensemble-average of Abel-inverted density profiles on mid-plane at 20 ms (*black*) and ensemble-averaged amplitude of line-integrated density fluctuations frequency integrated from 65-100 kHz (*red*).

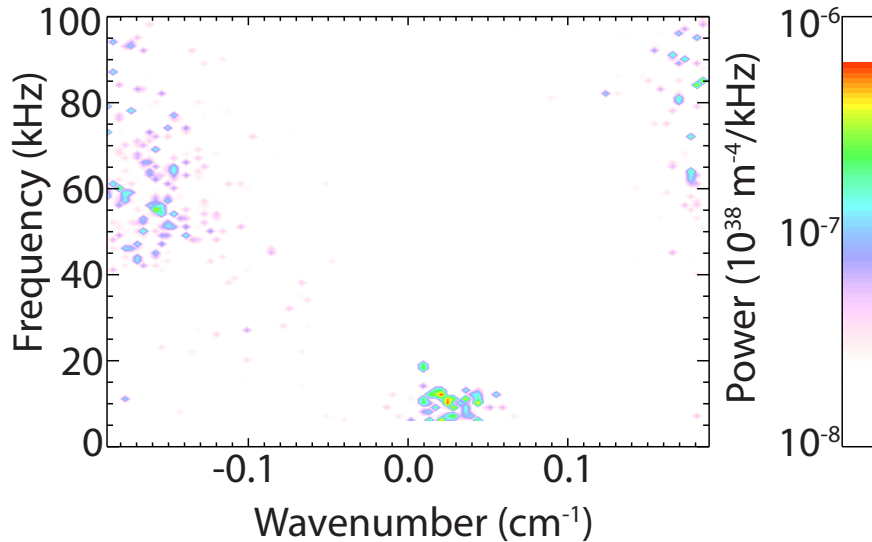


Figure 5.15 Frequency-wavenumber power spectrum of the line-integrated electron density fluctuations at $x = 0.36, 0.43$ m during PPCD in 400 kA plasmas. Positive (negative) wavenumber corresponds to wave propagation in the ion (electron) diamagnetic drift direction.

Figure 5.15 shows that the residual magnetic tearing modes are still present during the PPCD cycle. Additionally, the spectral feature at ~ 50 kHz is quite broad and low power, and is quite close to the Nyquist limit of the measurement. This implies that the spectral feature is aliasing onto lower wavenumbers measured by the FIR, and that the peak wavenumber for these discharges is too large to be measured with this technique. Theoretically, the FIR mixer upgrade will be able to measure the spectral feature, having a wavenumber limit of ~ 2 cm^{-1} . Other diagnostics may also be able to access this wavenumber range, such as the IDS-II system.

5.3.2 Crash-heated 500kA PPCD

High current crash heated PPCD plasmas are some of the highest temperature plasmas made in the MST. Studies on these plasmas have shown that the ion temperature increases significantly, and decays more slowly than in standard plasma operation [10]. The subsequent increases in the thermal gradients, namely the ion temperature gradient, may indicate that ion-temperature-gradient-like turbulence may become important. The frequency-wavenumber power spectrum shown in Figure 5.16 shows that the FIR cannot adequately describe the fluctuations in these plasmas. While

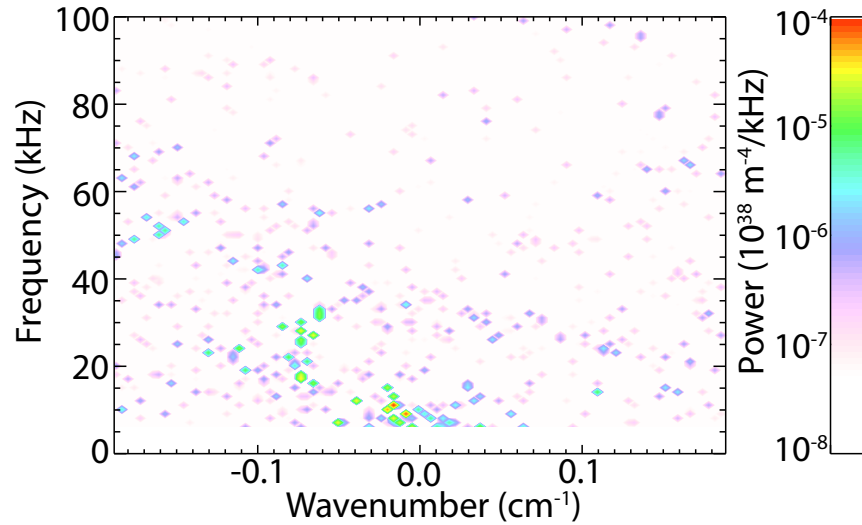


Figure 5.16 Frequency-wavenumber power spectrum of the line-integrated electron density fluctuations at $x = 0.36$ m during PPCD in 500 kA crash heated plasmas. Positive (negative) wavenumber corresponds to wave propagation in the ion (electron) diamagnetic drift direction.

the global tearing mode appears to be well defined, with low wavenumber and low frequency, as seen in other plasma equilibria, the higher frequency fluctuations are spread across a large number of wavenumbers, indicating the density fluctuations are highly aliased, and outside the diagnostic viewing parameters.

5.3.3 Medium-confinement 200kA PPCD

Occasionally, the PPCD cycle does not control the global magnetic tearing modes as well, and a sawtooth crash occurs several milliseconds into the PPCD cycle. Typically, these plasmas are discarded from ensembles and ignored, but some interesting phenomena have been observed by collecting these types of shots. These shots can have significantly different equilibrium profiles than the best 200 kA PPCD plasmas used previously, including having a comparable electron density gradient and ion temperature gradient, such that $\eta_i \sim 1$. Based on previous gyrokinetic simulations, this adjustment to the equilibrium suggests an ITG-like instability may become relevant, while the TEM-like instability may become less important, or disappear.

The density equilibrium in these plasmas can change significantly from shot to shot, as can the density fluctuation spectrum. In the edge of the plasma, where the gradients are strongest and drift waves are expected, there is again an emergent fluctuation, seen in Figure 5.17. In these plasmas, sawtooth crashes will typically occur early in the PPCD cycle, between 10–16 ms, seen as bursts of large density fluctuations throughout the frequency spectrum. From 18–20 ms, it appears that two separate spectral features emerge, with one peaking at ~ 30 kHz, and a higher frequency one between ~ 40 – 60 kHz. These may potentially correspond to separate drift wave instabilities, with the likely candidates for the fastest growing mode being ITG and TEM instabilities.

By looking at two spatially separated chords, as before, the wavenumber of these spectral features can be explored. The lower frequency emergent fluctuation, seen in Figure 5.18, peaks at a relatively low wavenumber, ~ 0.06 cm^{-1} in the electron diamagnetic drift direction, while the higher frequency emergent fluctuation is comparatively broad in both frequency and wavenumber, peaking at ~ 0.09 – 0.11 cm^{-1} . The two fluctuations appear to be propagating in the electron drift direction. It appears that, based on this data, these plasmas are unstable to a complicated version of TEM turbulence. There is no experimental evidence for the GENE predicted ITG turbulence. Regardless, due to the large variation between plasma discharges in this data set, this type of equilibrium is quite difficult to study in detail.

5.4 Measurement with the upgraded FIR system

Using the new planar-diode mixers in an array setup, referenced in Section 2.4, and as seen in Figure 5.19, significantly higher wavenumbers may potentially be measured, up to $\sim 1 - 2$ cm^{-1} , nearly a full order of magnitude higher than possible using toroidally separated chords. Experiments were done to explore this detector setup, with both toroidal and radial separation of the mixers. Initial setup had the mixers attached to each other directly, with the mixer inputs separated by ~ 1 cm. Data was taken in 200 kA PPCD plasmas, with the mixers displaced toroidally for one set of shots, and radially for another set of shots. In order to take radial separation data, a quarter wave plate was placed in front of the mixers to correct the laser polarization. The mixer array was found to be ineffective for phase difference, so a 1 cm spacer was introduced between

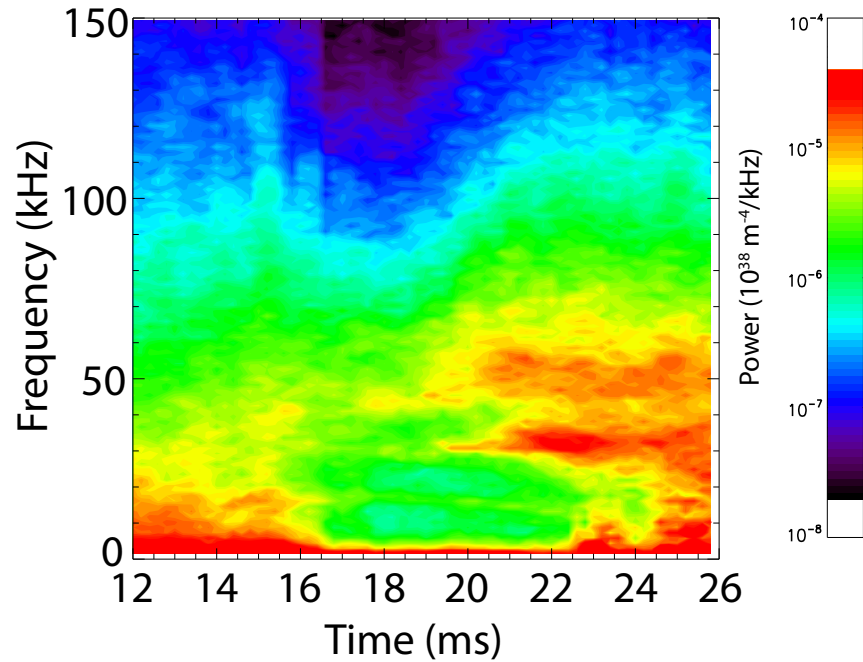


Figure 5.17 Density fluctuation power spectrum for an ensemble of medium confinement 200 kA PPCD plasmas. A second emergent fluctuation appears in this plasma equilibrium, implying the presence of a second, sub-dominant drift wave instability.

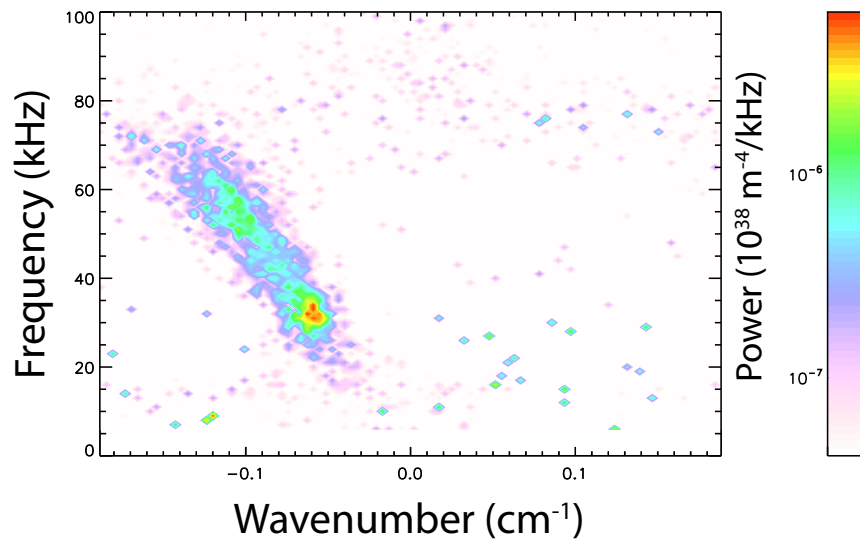


Figure 5.18 Frequency-wavenumber power spectrum of the line-integrated electron density fluctuations at $x = 0.36, 43$ m during PPCD in medium confinement 200 kA PPCD plasmas at $t = 20 - 21$ ms. Positive (negative) wavenumber corresponds to wave propagation in the ion (electron) diamagnetic drift direction.



Figure 5.19 Photograph of planar diode mixer in mixer tube (left) and two mixer array for high wavenumber measurement experiments (right).

the mixers, and apertures of various sizes were introduced in the beam line. The arrayed mixers saw effectively identical signals, as seen in Figure 5.20, limiting the usefulness of this setup. This setup may not adequately distinguish spatially separated plasma volumes due to the acceptance angle of the planar-diode mixers of 5° , which may cause the line-of-sight for the mixers to overlap. The apertures inserted to reduce the line-of-sight overlap reduced the laser power seen by the mixers by over an order of magnitude, requiring the use of the pre-amplifiers, which are removed for normal use with the planar-diode mixers. The noise introduced by the pre-amplifiers may have masked any small-scale phase differences in the mixer array. These problems may be addressed by using an array of 1 cm diameter focusing lenses for each mixer in the array, which would act as an aperture and increase the laser power seen by each mixer. A setup like this may be used in the future to measure high wavenumber fluctuations.

5.5 Summary

The FIR interferometer-polarimeter system has been used to explore relatively high frequency, high wavenumber density fluctuations in improved confinement RFP plasmas. In low current

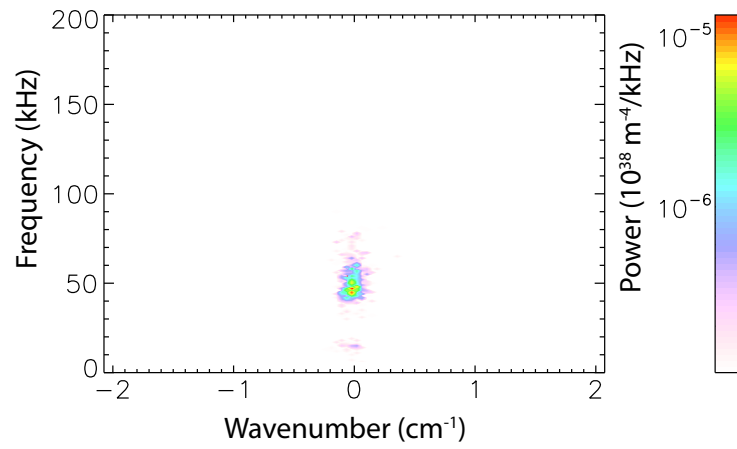


Figure 5.20 Frequency-wavenumber power spectrum of the line-integrated electron density fluctuations for high wavenumber measurement, with both mixers located at an impact parameter of $x = 0.43$ m.

(200 kA) PPCD discharges, the highest power density fluctuations are associated with a ~ 50 kHz, $\sim 0.1 \text{ cm}^{-1}$ spectral feature which propagates in the electron diamagnetic drift direction. This spectral feature has been found to depend strongly on the density gradient in the edge of the plasma, and has a critical density gradient of $R_0 \langle |\nabla n_e|_{0.8} \rangle / \langle n_e \rangle_{0.8} \approx 18$ below which the spectral feature does not appear. The spectral feature is localized in the outboard edge of the plasma, consistent with a ballooning structure. Predicted stochastic electron heat conductivity $\chi_{st,e}$ was calculated in the plasma region of interest, and was found to be quite small ($\chi_{st,e} \sim 1 \text{ m}^2/\text{s}$), implying some other method for heat transport in these plasmas, such as the presence of electrostatic drift wave turbulence. This spectral feature compares favorably to a TEM predicted by GENE simulations of these plasma equilibrium.

In “medium-confinement” 200 kA PPCD plasmas, a second, co-dominant fluctuation appears. In GENE simulations of this plasma equilibrium, ITG turbulence was found to be the dominant instability. Experimentally, this does not appear to be the case, given the direction of propagation of the observed density fluctuation, and the observed turbulence may still be TEM-like.

In higher current discharges, the spectral feature appears to increase in wavenumber, outside the range of the FIR system’s capabilities. Upgrades to the FIR mixers, including employing an array of mixers in the same chord, were not successful in resolving the wavenumber spectrum of the instability in these plasmas. Producing a description of the turbulence characteristics of these plasmas may prove to be a fruitful area of future research.

Chapter 6

Summary and Future Work

THE MST FIR interferometer-polarimeter system has been upgraded with new planar-diode mixers, and has been used to measure density fluctuations consistent with the trapped-electron-mode instability in improved confinement RFP plasmas. This is the first description of these fluctuations in this plasma configuration. The measured density fluctuations are consistent with predictions made by the gyrokinetic code GENE. The experimental role of these instabilities in particle transport is as yet unknown due to the measurement of plasma velocity fluctuations being unavailable, so the density fluctuations cannot be correlated with the velocity fluctuations.

6.1 Density fluctuations

The FIR system was used to compare the density fluctuation spectra in standard and improved confinement plasmas, to infer the relative thermal transport in the two regimes. Density fluctuations are significantly suppressed in improved confinement plasmas, which is expected for the significantly lower transport in this regime. However, there is a peak in the improved confinement density fluctuation spectra at higher frequencies, on the order of 50 kHz. These higher frequency density fluctuations are not observed in standard plasmas by the FIR system, and are expected to be associated with drift wave instabilities. The higher frequency density fluctuations were correlated to the density gradient, and had electron diamagnetic drift direction propagation. In 200 kA PPCD plasmas, the emergent density fluctuations scaled with a normalized density gradient parameter, $R_0 \langle |\nabla n_e|_{0.8} \rangle / \langle n_e \rangle_{0.8}$, and had a critical normalized density gradient, $R_0 \langle |\nabla n_e|_{0.8} \rangle / \langle n_e \rangle_{0.8} \approx 18$. The spectral power as a function of the wavenumber and frequency was found, and the density

fluctuation peaked at $f \approx 50$ kHz and $k \approx 0.1$ cm⁻¹ in the electron diamagnetic direction. The density fluctuations were localized in the outboard edge of the plasma, where the density and temperature gradients are largest and indicative of a ballooning type structure of the turbulence. No scaling with the electron temperature gradient was observed in these 200 kA PPCD plasmas.

While similar emergent density fluctuations structures were observed in higher current 400 kA PPCD plasmas, they proved to be difficult for the current FIR diagnostic system to resolve in wavenumber. The density fluctuations in these plasmas were broader in frequency, ranging from ~ 40 kHz to ~ 150 kHz, and significantly lower power. The density fluctuation power peaked further away from the wall, at $r/a \approx 0.75$, consistent with a density gradient driven instability, given the location of the peak density gradient in these plasmas was also further from the wall. The wavenumber of the density fluctuation was unresolvable with the current FIR system, showing significant aliasing in the spectral power, indicating a peak wavenumber ≥ 0.2 cm⁻¹.

6.2 GENE Comparison

The GENE code has been used to simulate the unstable mode spectrum for several improved confinement RFP equilibria. These simulations made several predictions about these plasmas regarding the fastest growing instability and the drive for any instability. There were also predictions made regarding peak wavenumber, frequency, and required gradients for such drift waves. Initial simulations predicted a very large zonal flow that inhibited transport to very low levels. These zonal flows were found to be disrupted by residual magnetic fluctuations caused by the incomplete suppression of the global tearing mode present in RFP plasmas. In simulations of 200 kA PPCD plasmas, TEM microturbulence was found to be the dominant instability. The TEM was found to be primarily driven by the density gradient, and exhibited a critical density gradient, below which the mode was stable. The relative agreement between the GENE simulation predictions and the experimental FIR data suggest that there exists a TEM in the outboard edge of 200 kA PPCD plasmas which may influence transport [57].

6.3 FIR upgrades

The FIR has been upgraded with new planar-diode mixers, which were compared to the old corner-cube mixers. The new mixers have a significantly lower noise floor, and significantly more sensitivity [45]. This allowed for experiments with no focusing lens in an attempt to increase the spatial sensitivity of the system. Initial testing for high wavenumber fluctuations was unsuccessful, likely due to overlap of the angle of acceptance of the mixer array resulting in a lack of phase separation. This measurement could potentially be improved by including an array of lenses for the mixer array, further differentiating the plasma volume sampled by each mixer.

6.4 Conclusions

In summary, density fluctuations with characteristics consistent with density-gradient-driven trapped electron modes emerge in reduced-tearing MST RFP plasmas. The fluctuations exhibit a critical-gradient threshold, propagate in the electron diamagnetic drift direction, and have perpendicular wavelengths expected for TEMs. These features are consistent with gyrokinetic modeling based on measured plasma equilibria. Critical gradient behavior is characteristic of microturbulence that regulates heat and particle transport, for example the ‘stiffness’ observed in core temperature profiles of tokamak plasmas [77, 93, 94]. While the critical gradient behavior in Figure 5.6 suggests the same may apply for PPCD’s reduced-tearing conditions, experimentally it is difficult to separate TEM-induced transport from that due to residual tearing and stochastic transport. Future measurements may be able to make this distinction in MST plasmas, e.g., using insertable probes. Nonlinear modeling with GENE predicts very low transport levels in the absence of tearing fluctuations. When residual tearing is included, their disruptive effect on zonal flows leads to higher turbulent saturation levels and fluxes comparable with the power-balance measured heat conductivity in PPCD plasmas, $\chi_e \sim 5 - 10 \text{ m}^2/\text{s}$, compared to a stochastic heat conductivity predicted to be $\chi_{st,e} \sim 1 \text{ m}^2/\text{s}$. It is therefore likely that TEM microturbulence plays a significant role in regulating transport in the edge region of reduced-tearing RFP plasmas. The gyrokinetic

modeling predictions for large critical gradients and strong zonal flows shows that the RFP configuration has tokamak-level turbulent transport with partial suppression of tearing modes, and transport could be even smaller than that of tokamak plasmas if more thorough tearing reduction were achieved experimentally.

6.5 Future Work

The work in this thesis can be expanded in several ways. The recent FIR mixer upgrade, while increasing bandwidth and signal-to-noise ratio, has an as-yet not fully explored design space. Additionally, the level of transport in improved confinement plasmas due to drift wave turbulence was not measured.

While some experiments were done to explore high wavenumber measurements, they proved relatively fruitless at the time, likely due to overlap of the mixer viewing angle. This may be alleviated by designing an optical system such that the mixers in a high wavenumber setup have individual, more distinct optical paths. This could be accomplished by having an array of lenses for the mixer array, decreasing the need for apertures that significantly decrease signal power, and potentially decreasing the overlap of the optical paths.

While the density fluctuation power in 200 kA PPCD plasmas appears to be largely attributed to trapped-electron mode turbulence, this may not be the case in other plasma equilibria. In higher current 400 kA PPCD plasmas, for example, there may be a combination of trapped-electron mode and ion-temperature gradient mode instability. There is also evidence of some drift wave turbulence in the extreme edge of standard plasma equilibria [95]. These plasma equilibria need to be explored further experimentally to attribute the thermal transport to any unstable modes.

Some of the first measurements on the MST were to characterize transport in the edge of the plasma [96]. These experiments could be repeated in low current PPCD discharges in an attempt to characterize the particle and heat transport associated with the electrostatic drift wave turbulence described in this thesis.

The effects of magnetic perturbations on zonal flows is an interesting area of research, but difficult to study in RFP plasmas, where magnetic perturbations cannot currently be completely

suppressed. However, in a tokamak plasma where magnetic turbulence is small, the effects of externally applied resonant magnetic perturbations on zonal flows could be studied.

LIST OF REFERENCES

- [1] P. C. Liewer, “Measurements of microturbulence in tokamaks and comparisons with theories of turbulence and anomalous transport,” *Nucl. Fusion*, vol. 25, p. 543, May 1985.
- [2] A. J. Wootton, B. A. Carreras, H. Matsumoto, K. McGuire, W. A. Peebles, C. P. Ritz, P. W. Terry, and S. J. Zweben, “Fluctuations and anomalous transport in tokamaks,” *Physics of Fluids B: Plasma Physics (1989-1993)*, vol. 2, pp. 2879–2903, Dec. 1990.
- [3] A. B. Rechester and M. N. Rosenbluth, “Electron heat transport in a tokamak with destroyed magnetic surfaces,” *Phys. Rev. Lett.*, vol. 40, pp. 38–41, 1978.
- [4] T. M. Biewer, J. K. Anderson, G. Fiksel, B. Hudson, J. C. Wright, S. C. Prager, C. B. Forest, W. Ding, and S. D. Terry, “Electron heat transport in the mst reversed-field pinch with destroyed magnetic surfaces,” *Phys. Rev. Lett.*, vol. 91, p. 045004, 2003.
- [5] W. X. Ding, D. L. Brower, G. Fiksel, D. J. Den Hartog, S. C. Prager, and J. S. Sarff, “Magnetic-Fluctuation-Induced Particle Transport and Density Relaxation in a High-Temperature Plasma,” *Phys. Rev. Lett.*, vol. 103, p. 025001, July 2009.
- [6] J. A. Reusch, J. K. Anderson, D. J. Den Hartog, F. Ebrahimi, D. D. Schnack, H. D. Stephens, and C. B. Forest, “Experimental evidence for a reduction in electron thermal diffusion due to trapped particles,” *Phys. Rev. Lett.*, vol. 107, p. 155002, 2011.
- [7] M. J. Pueschel, M. Kammerer, and F. Jenko, “Gyrokinetic turbulence simulations at high plasma beta,” *Physics of Plasmas (1994-present)*, vol. 15, p. 102310, Oct. 2008.
- [8] B. E. Chapman, J. K. Anderson, T. M. Biewer, D. L. Brower, S. Castillo, P. K. Chattopadhyay, C.-S. Chiang, D. Craig, D. J. Den Hartog, G. Fiksel, P. W. Fontana, C. B. Forest, S. Gerhardt, A. K. Hansen, D. Holly, Y. Jiang, N. E. Lanier, S. C. Prager, J. C. Reardon, and J. S. Sarff, “Reduced edge instability and improved confinement in the mst reversed-field pinch,” *Phys. Rev. Lett.*, vol. 87, p. 205001, Oct 2001.

- [9] J. S. Sarff, J. K. Anderson, T. M. Biewer, D. L. Brower, B. E. Chapman, P. K. Chattopadhyay, D. Craig, B. Deng, D. J. DenHartog, W. X. Ding, G. Fiksel, C. B. Forest, J. A. Goetz, R. O’Connell, S. C. Prager, and M. A. Thomas, “Tokamak-like confinement at high beta and low field in the reversed field pinch,” *Plasma Phys. and Control. Fusion*, vol. 45, p. A457, 2003.
- [10] B. E. Chapman, A. F. Almagri, J. K. Anderson, D. L. Brower, K. J. Caspary, D. J. Clayton, D. Craig, D. J. D. Hartog, W. X. Ding, D. A. Ennis, G. Fiksel, S. Gangadhara, S. Kumar, R. M. Magee, R. O’Connell, E. Parke, S. C. Prager, J. A. Reusch, J. S. Sarff, H. D. Stephens, and Y. M. Yang, “Generation and confinement of hot ions and electrons in a reversed-field pinch plasma,” *Plasma Phys. Cont. Fusion*, vol. 52, no. 12, p. 124048, 2010.
- [11] R. Lorenzini, E. Martines, P. Piovesan, D. Terranova, P. Zanca, M. Zuin, A. Alfieri, D. Bonfiglio, F. Bonomo, A. Canton, S. Cappello, L. Carraro, R. Cavazzana, D. F. Escande, A. Fassina, P. Franz, M. Gobbin, P. Innocente, L. Marrelli, R. Pasqualotto, M. E. Puiatti, M. Spolaore, M. Valisa, and N. Vianello, “Self-organized helical equilibria as a new paradigm for ohmically heated fusion plasmas,” *Nature Phys.*, vol. 5, no. 8, pp. 570–574, 2009.
- [12] I. Predebon, F. Sattin, M. Veranda, D. Bonfiglio, and S. Cappello, “Microtearing Modes in Reversed Field Pinch Plasmas,” *Phys. Rev. Lett.*, vol. 105, p. 195001, Nov. 2010. 00037.
- [13] D. Carmody, M. J. Pueschel, and P. W. Terry, “Gyrokinetic studies of microinstabilities in the reversed field pinch,” *Phys. Plasmas*, vol. 20, no. 5, pp. –, 2013.
- [14] D. Carmody, M. J. Pueschel, J. K. Anderson, and P. W. Terry, “Microturbulence studies of pulsed poloidal current drive discharges in the reversed field pinch,” *Physics of Plasmas (1994-present)*, vol. 22, p. 012504, Jan. 2015.
- [15] M. J. Pueschel, P. W. Terry, F. Jenko, D. R. Hatch, W. M. Nevins, T. Görler, and D. Told, “Extreme Heat Fluxes in Gyrokinetic Simulations: A New Critical β ,” *Phys. Rev. Lett.*, vol. 110, p. 155005, Apr. 2013.
- [16] P. W. Terry, M. J. Pueschel, D. Carmody, and W. M. Nevins, “The effect of magnetic flutter on residual flow,” *Physics of Plasmas (1994-present)*, vol. 20, p. 112502, Nov. 2013.
- [17] F. Jenko, W. Dorland, M. Kotschenreuther, and B. N. Rogers, “Electron temperature gradient driven turbulence,” *Phys. Plasmas*, vol. 7, no. 5, pp. 1904–1910, 2000.
- [18] J. B. Taylor, “Relaxation of toroidal plasma and generation of reverse magnetic fields,” *Phys. Rev. Lett.*, vol. 33, pp. 1139–1141, Nov 1974.
- [19] P. W. Fontana, D. J. Den Hartog, G. Fiksel, and S. C. Prager, “Spectroscopic observation of fluctuation-induced dynamo in the edge of the reversed-field pinch,” *Phys. Rev. Lett.*, vol. 85, pp. 566–569, Jul 2000.

- [20] D. J. D. Hartog, J. T. Chapman, D. Craig, G. Fiksel, P. W. Fontana, S. C. Prager, and J. S. Sarff, "Measurement of core velocity fluctuations and the dynamo in a reversed-field pinch," *Physics of Plasmas*, vol. 6, no. 5, pp. 1813–1821, 1999.
- [21] H. Ji, A. F. Almagri, S. C. Prager, and J. S. Sarff, "Time-resolved observation of discrete and continuous magnetohydrodynamic dynamo in the reversed-field pinch edge," *Phys. Rev. Lett.*, vol. 73, pp. 668–671, Aug 1994.
- [22] W. X. Ding, D. L. Brower, B. H. Deng, A. F. Almagri, D. Craig, G. Fiksel, V. Mirnov, S. C. Prager, J. S. Sarff, and V. Svidzinski, "The hall dynamo effect and nonlinear mode coupling during sawtooth magnetic reconnection," *Physics of Plasmas*, vol. 13, no. 11, p. 112306, 2006.
- [23] T. D. Tharp, A. F. Almagri, M. C. Miller, V. V. Mirnov, S. C. Prager, J. S. Sarff, and C. C. Kim, "Measurements of impulsive reconnection driven by nonlinear hall dynamics," *Physics of Plasmas*, vol. 17, no. 12, p. 120701, 2010.
- [24] J. Triana, *Measurement of two-fluid relaxation in the Madison symmetric torus*. PhD thesis, University of Wisconsin - Madison, April 2017.
- [25] R. Dexter, D. Kerst, T. Lovell, S. Prager, and J. Sprott, "The madison symmetric torus," *Fusion Tech.*, vol. 19, p. 131, 1991.
- [26] J. Sarff, "The RFP as a fusion power core." Internal MST documentation, 2014.
- [27] J. S. Sarff, S. A. Hokin, H. Ji, S. C. Prager, and C. R. Sovinec, "Fluctuation and transport reduction in a reversed field pinch by inductive poloidal current drive," *Phys. Rev. Lett.*, vol. 72, pp. 3670–3673, Jun 1994.
- [28] J. S. Sarff, A. F. Almagri, M. Cekic, C. Chaing, D. Craig, D. J. D. Hartog, G. Fiksel, S. A. Hokin, R. W. Harvey, H. Ji, C. Litwin, S. C. Prager, D. Sinitsyn, C. R. Sovinec, J. C. Sprott, and E. Uchimoto, "Transport reduction by current profile control in the reversedfield pinch," *Physics of Plasmas*, vol. 2, no. 6, pp. 2440–2446, 1995.
- [29] B. Chapman, "PPCD tutorial: what it is, what it was, what it shall be." Internal MST documentation, 2013.
- [30] J. S. Sarff, A. F. Almagri, J. K. Anderson, T. M. Biewer, A. P. Blair, M. Cengher, B. E. Chapman, P. K. Chattopadhyay, D. Craig, D. J. DenHartog, F. Ebrahimi, G. Fiksel, C. B. Forest, J. A. Goetz, D. Holly, B. Hudson, T. W. Lovell, K. J. McCollam, P. D. Nonn, R. O'Connell, S. P. Oliva, S. C. Prager, J. C. Reardon, M. A. Thomas, M. D. Wyman, D. L. Brower, W. X. Ding, S. D. Terry, M. D. Carter, V. I. Davydenko, A. A. Ivanov, R. W. Harvey, R. I. Pinsker, and C. Xiao, "Tokamak-like confinement at a high beta and low toroidal field in the mst reversed field pinch," *Nucl. Fusion*, vol. 43, p. 1684, 2003.

- [31] J. Sarff, “Phenomenology and consequences of tearing instability in the RFP.” Internal MST documentation, 2014.
- [32] E. Uchimoto, M. Cekic, R. W. Harvey, C. Litwin, S. C. Prager, J. S. Sarff, and C. R. Sovinec, “Lowerhybrid poloidal current drive for fluctuation reduction in a reversed field pinch,” *Physics of Plasmas*, vol. 1, no. 11, pp. 3517–3519, 1994.
- [33] J. Sarff, “Heat transport in a stochastic magnetic field,” in *CMPD and CMSO Winter School 2009*, (UCLA), Jan. 5, 2009 2009.
- [34] L. Lin, W. Ding, D. Brower, A. Almagri, J. Anderson, B. Chapman, J. Koliner, D. Liu, M. Nornberg, J. Sarff, and J. Waksman, “Internal measurements of density and magnetic fluctuations in the MST-RFP,” in *APSDPP 2011*, (Salt Lake City, UT), Nov. 14, 2011 2011.
- [35] Y. Jiang, D. L. Brower, and N. E. Lanier, “Interferometric measurement of high-frequency density fluctuations in Madison symmetric torus,” *Review of Scientific Instruments*, vol. 70, no. 1, pp. 703–706, 1999.
- [36] W. X. Ding, L. Lin, J. R. Duff, D. L. Brower, and J. S. Sarff, “Density fluctuation measurements by far-forward collective scattering in the MST reversed-field pinch,” *Review of Scientific Instruments*, vol. 83, no. 10, p. 10E302, 2012.
- [37] J. R. Duff, Z. R. Williams, D. L. Brower, B. E. Chapman, W. X. Ding, M. J. Pueschel, J. S. Sarff, and P. W. Terry, “Observation of trapped-electron-mode microturbulence in reversed field pinch plasmas,” *Physics of Plasmas*, vol. 25, no. 1, p. 010701, 2018.
- [38] P. Fimognari, “Demodulation of the magnetic modes.” Internal MST documentation, 2016.
- [39] D. Craig, “Magnetic mode analysis in MST.” Internal MST documentation, 2005.
- [40] H. Stephens, *Electron Temperature Structures Associated With Magnetic Tearing Modes in the Madison Symmetric Torus*. PhD thesis, University of Wisconsin - Madison, January 2010.
- [41] I. H. Hutchinson, *Principles of Plasma Diagnostics*. The Edinburgh Building, Cambridge CB2 2RU, UK: Cambridge University Press, second ed., July 2005.
- [42] J. Sheffield, *Plasma scattering of electromagnetic radiation*. New York, NY (USA): Academic Press, 1975.
- [43] J. Anderson, C. Forest, T. Biewer, J. Sarff, and J. Wright, “Equilibrium reconstruction in the Madison Symmetric Torus reversed field pinch,” *Nuclear Fusion*, vol. 44, no. 1, p. 162, 2004.
- [44] N. E. Lanier, J. K. Anderson, C. B. Forest, D. Holly, Y. Jiang, and D. L. Brower, “First results from the far-infrared polarimeter system on the Madison Symmetric Torus reversed field pinch,” *Review of Scientific Instruments*, vol. 70, no. 1, pp. 718–721, 1999.

- [45] E. Parke, W. X. Ding, J. Duff, and D. L. Brower, “An upgraded interferometer-polarimeter system for broadband fluctuation measurements,” *Review of Scientific Instruments*, vol. 87, no. 11, p. 11E115, 2016.
- [46] W. X. Ding, L. Lin, J. R. Duff, and D. L. Brower, “High-frequency fluctuation measurements by far-infrared laser faraday-effect polarimetry-interferometry and forward scattering system on MST,” *Review of Scientific Instruments*, vol. 85, no. 11, 2014.
- [47] F. L. Hinton and R. D. Hazeltine, “Theory of plasma transport in toroidal confinement systems,” *Rev. Mod. Phys.*, vol. 48, pp. 239–308, Apr 1976.
- [48] J. K. Anderson, J. Adney, A. Almagri, A. Blair, D. L. Brower, M. Cengher, B. E. Chapman, S. Choi, D. Craig, D. R. Demers, D. J. D. Hartog, B. Deng, W. X. Ding, F. Ebrahimi, D. Ennis, G. Fiksel, C. B. Forest, P. Franz, J. Goetz, R. W. Harvey, D. Holly, B. Hudson, M. Kaufman, T. Lovell, L. Marrelli, P. Martin, K. McCollam, V. V. Mirnov, P. Nonn, R. OConnell, S. Oliva, P. Piovesan, S. C. Prager, I. Predebon, J. S. Sarff, G. Spizzo, V. Svidzinski, M. Thomas, and M. D. Wyman, “Dynamo-free plasma in the reversed-field pinch: Advances in understanding the reversed-field pinch improved confinement mode,” *Physics of Plasmas*, vol. 12, no. 5, p. 056118, 2005.
- [49] F. F. Chen, *Introduction to Plasma Physics and Controlled Fusion*. Springer US, second ed., 1984.
- [50] W. Horton, “Drift waves and transport,” *Reviews of Modern Physics*, vol. 71, pp. 735–778, 4 1999.
- [51] B. Coppi and F. Pegoraro, “Theory of the ubiquitous mode,” *Nuclear Fusion*, vol. 17, no. 5, p. 969, 1977.
- [52] H. Nordman, J. Weiland, and A. Jarman, “Simulation of toroidal drift mode turbulence driven by temperature gradients and electron trapping,” *Nuclear Fusion*, vol. 30, no. 6, p. 983, 1990.
- [53] T. Dannert and F. Jenko, “Gyrokinetic simulation of collisionless trapped-electron mode turbulence,” *Physics of Plasmas*, vol. 12, no. 7, p. 072309, 2005.
- [54] M. A. Mahmood, T. Rafiq, M. Persson, and J. Weiland, “Collisionless trapped electron and ion temperature gradient modes in an advanced tokamak equilibrium,” *Physics of Plasmas*, vol. 16, no. 2, p. 022503, 2009.
- [55] J. H. E. Proll, P. Xanthopoulos, and P. Helander, “Collisionless microinstabilities in stellarators. ii. numerical simulations,” *Physics of Plasmas*, vol. 20, no. 12, p. 122506, 2013.
- [56] G. G. Plunk, J. W. Connor, and P. Helander, “Collisionless microinstabilities in stellarators. part 4. the ion-driven trapped-electron mode,” *Journal of Plasma Physics*, vol. 83, no. 4, 2017.

- [57] Z. R. Williams, M. J. Pueschel, P. W. Terry, and T. Hauff, “Turbulence, transport, and zonal flows in the madison symmetric torus reversed-field pinch,” *Physics of Plasmas*, vol. 24, no. 12, p. 122309, 2017.
- [58] D. R. Ernst, J. Lang, W. M. Nevins, M. Hoffman, Y. Chen, W. Dorland, and S. Parker, “Role of zonal flows in trapped electron mode turbulence through nonlinear gyrokinetic particle and continuum simulation,” *Physics of Plasmas*, vol. 16, no. 5, p. 055906, 2009.
- [59] P. H. Diamond, S.-I. Itoh, K. Itoh, and T. S. Hahm, “Zonal flows in plasmas review,” *Plasma Physics and Controlled Fusion*, vol. 47, no. 5, p. R35, 2005.
- [60] B. Galperin and P. Read, *Zonal Jets*. Cambridge: Cambridge University Press, first ed., 2018.
- [61] R. J. Goldston and P. H. Rutherford, *Introduction to Plasma Physics*. Redcliffe Way, Bristol BSI 6NX, UK: Institute of Physics Publishing, second ed., July 1995.
- [62] G. G. Plunk, P. Helander, P. Xanthopoulos, and J. W. Connor, “Collisionless microinstabilities in stellarators. iii. the ion-temperature-gradient mode,” *Physics of Plasmas*, vol. 21, no. 3, p. 032112, 2014.
- [63] D. Carmody, *Microinstabilities and turbulent transport in the reversed field pinch*. PhD thesis, University of Wisconsin - Madison, December 2014.
- [64] M. Zuin, S. Spagnolo, I. Predebon, F. Sattin, F. Auremma, R. Cavazzana, A. Fassina, E. Martines, R. Paccagnella, M. Spolaore, and N. Vianello, “Experimental observation of microtearing modes in a toroidal fusion plasma,” *Phys. Rev. Lett.*, vol. 110, p. 055002, Jan 2013.
- [65] X. Garbet, Y. Idomura, L. Villard, and T. Watanabe, “Gyrokinetic simulations of turbulent transport,” *Nuclear Fusion*, vol. 50, no. 4, p. 043002, 2010.
- [66] R. G. Littlejohn, “A guiding center hamiltonian: A new approach,” *Journal of Mathematical Physics*, vol. 20, no. 12, pp. 2445–2458, 1979.
- [67] R. G. Littlejohn, “Hamiltonian formulation of guiding center motion,” *The Physics of Fluids*, vol. 24, no. 9, pp. 1730–1749, 1981.
- [68] R. G. Littlejohn, “Hamiltonian perturbation theory in noncanonical coordinates,” *Journal of Mathematical Physics*, vol. 23, no. 5, pp. 742–747, 1982.
- [69] R. G. Littlejohn, “Variational principles of guiding centre motion,” *Journal of Plasma Physics*, vol. 29, no. 1, p. 111125, 1983.
- [70] D. H. E. Dubin, J. A. Krommes, C. Oberman, and W. W. Lee, “Nonlinear gyrokinetic equations,” *The Physics of Fluids*, vol. 26, no. 12, pp. 3524–3535, 1983.
- [71] T. S. Hahm, W. W. Lee, and A. Brizard, “Nonlinear gyrokinetic theory for finite-beta plasmas,” *The Physics of Fluids*, vol. 31, no. 7, pp. 1940–1948, 1988.

- [72] T. S. Hahm, “Nonlinear gyrokinetic equations for tokamak microturbulence,” *The Physics of Fluids*, vol. 31, no. 9, pp. 2670–2673, 1988.
- [73] A. Brizard, “Nonlinear gyrokinetic maxwell-vlasov equations using magnetic co-ordinates,” *Journal of Plasma Physics*, vol. 41, no. 3, p. 541559, 1989.
- [74] J. R. Cary, “Lie transform perturbation theory for hamiltonian systems,” *Physics Reports*, vol. 79, no. 2, pp. 129 – 159, 1981.
- [75] J. R. Cary and R. G. Littlejohn, “Noncanonical hamiltonian mechanics and its application to magnetic field line flow,” *Annals of Physics*, vol. 151, no. 1, pp. 1 – 34, 1983.
- [76] M. Pueschel, *Electromagnetic effects in gyrokinetic simulations of plasma turbulence*. PhD thesis, Westfalischen Wilhelms-Universitat Munster, December 2009.
- [77] X. Garbet, P. Mantica, F. Ryter, G. Cordey, F. Imbeaux, C. Sozzi, A. Manini, E. Asp, V. Parail, R. Wolf, and t. J. E. Contributors, “Profile stiffness and global confinement,” *Plasma Phys. Control. Fusion*, vol. 46, no. 9, p. 1351, 2004.
- [78] M. Beer, *Gyrofluid Models of Turbulent Transport in Tokamaks*. PhD thesis, Princeton University, December 1994.
- [79] F. Merz, *Gyrokinetic Simulation of Multimode Plasma Turbulence*. PhD thesis, Westfalischen Wilhelms-Universitat Munster, December 2008.
- [80] V. Tangri, P. W. Terry, and R. E. Waltz, “A circular equilibrium model for local gyrokinetic simulations of ion temperature gradient fluctuations in reversed field pinches,” *Physics of Plasmas*, vol. 18, no. 5, p. 052310, 2011.
- [81] P. W. Terry, D. Carmody, H. Doerk, W. Guttenfelder, D. R. Hatch, C. C. Hegna, A. Ishizawa, F. Jenko, W.M. Nevins, I. Predebon, M. J. Pueschel, J. S. Sarff, and G. G. Whelan, “Overview of gyrokinetic studies of finite- microturbulence,” *Nucl. Fusion*, vol. 55, no. 10, p. 104011, 2015.
- [82] G. T. Hoang, C. Bourdelle, X. Garbet, G. Giruzzi, T. Aniel, M. Ottaviani, W. Horton, P. Zhu, and R. V. Budny, “Experimental determination of critical threshold in electron transport on Tore Supra,” *Phys. Rev. Lett.*, vol. 87, p. 125001, Sep 2001.
- [83] D. Villegas, R. Guirlet, C. Bourdelle, G. T. Hoang, X. Garbet, and R. Sabot, “Experimental electron temperature gradient dependence of heavy impurity transport in fusion devices,” *Phys. Rev. Lett.*, vol. 105, p. 035002, Jul 2010.
- [84] J. C. Hillesheim, J. C. DeBoo, W. A. Peebles, T. A. Carter, G. Wang, T. L. Rhodes, L. Schmitz, G. R. McKee, Z. Yan, G. M. Staebler, K. H. Burrell, E. J. Doyle, C. Holland, C. C. Petty, S. P. Smith, A. E. White, and L. Zeng, “Observation of a critical gradient threshold for electron temperature fluctuations in the DIII-D Tokamak,” *Phys. Rev. Lett.*, vol. 110, p. 045003, Jan 2013.

- [85] J. Anderson, C. Forest, T. Biewer, J. Sarff, and J. Wright, “Equilibrium reconstruction in the madison symmetric torus reversed field pinch,” *Nuclear Fusion*, vol. 44, no. 1, p. 162, 2004.
- [86] J. Wesson, *Tokamaks*. OUP Oxford, 2011: Oxford Science Publications, fourth ed., July 2011.
- [87] A. Dimits, B. Cohen, N. Mattor, W. Nevins, D. Shumaker, S. Parker, and C. Kim, “Simulation of ion temperature gradient turbulence in tokamaks,” *Nuclear Fusion*, vol. 40, no. 3Y, p. 661, 2000.
- [88] N. E. Lanier, D. Craig, J. K. Anderson, T. M. Biewer, B. E. Chapman, D. J. D. Hartog, C. B. Forest, S. C. Prager, D. L. Brower, and Y. Jiang, “Measurement of electron transport in the Madison Symmetric Torus reversed-field pinch (invited),” *Review of Scientific Instruments*, vol. 72, no. 1, pp. 1039–1045, 2001.
- [89] L. Lin, W. X. Ding, D. L. Brower, W. F. Bergerson, T. A. Carter, T. F. Yates, A. F. Almagri, B. E. Chapman, and J. S. Sarff, “Role of nonlinear coupling and density fluctuations in magnetic-fluctuation-induced particle transport,” *Phys. Rev. Lett.*, vol. 108, p. 175001, Apr 2012.
- [90] B. E. Chapman, A. F. Almagri, J. K. Anderson, C.-S. Chiang, D. Craig, G. Fiksel, N. E. Lanier, S. C. Prager, J. S. Sarff, M. R. Stoneking, and P. W. Terry, “Eb flow shear and enhanced confinement in the madison symmetric torus reversed-field pinch,” *Physics of Plasmas*, vol. 5, no. 5, pp. 1848–1854, 1998.
- [91] D. Craig, A. F. Almagri, J. K. Anderson, J. T. Chapman, C.-S. Chiang, N. A. Crocker, D. J. Den Hartog, G. Fiksel, S. C. Prager, J. S. Sarff, and M. R. Stoneking, “Enhanced confinement with plasma biasing in the mst reversed field pinch,” *Phys. Rev. Lett.*, vol. 79, pp. 1865–1868, Sep 1997.
- [92] C. Sovinec, *Magnetohydrodynamic simulations of noninductive helicity injection in the reversed-field pinch and tokamak*. PhD thesis, University of Wisconsin - Madison, 1995.
- [93] D. Mikkelsen, H. Shirai, H. Urano, T. Takizuka, Y. Kamada, T. Hatae, Y. Koide, N. Asakura, T. Fujita, T. Fukuda, S. Ide, A. Isayama, Y. Kawano, O. Naito, and Y. Sakamoto, “Stiff temperature profiles in JT-60U ELMY H-mode plasmas,” *Nuclear Fusion*, vol. 43, no. 1, p. 30, 2003.
- [94] F. Ryter, C. Angioni, M. Beurskens, S. Cirant, G. T. Hoang, G. M. D. Hogeweij, F. Imbeaux, A. Jacchia, P. Mantica, W. Suttrop, and G. Tardini, “Experimental studies of electron transport,” *Plasma Physics and Controlled Fusion*, vol. 43, no. 12A, p. A323, 2001.
- [95] D. J. Thuecks, A. F. Almagri, J. S. Sarff, and P. W. Terry, “Evidence for drift waves in the turbulence of reversed field pinch plasmas,” *Physics of Plasmas*, vol. 24, no. 2, p. 022309, 2017.

- [96] T. D. Rempel, C. W. Spragins, S. C. Prager, S. Assadi, D. J. Den Hartog, and S. Hokin, "Edge electrostatic fluctuations and transport in a reversed-field pinch," *Phys. Rev. Lett.*, vol. 67, pp. 1438–1441, Sep 1991.

APPENDIX

Spectral analysis

This appendix outlines the procedure for finding spectral power, coherence, and the wavenumber-frequency power spectra for a set of signals, as described by Beall, 1982. By taking the Fourier transform of a set of signals, information on the wavenumber spectra can be found using the phase information of the signals.

A.1 Fourier transforms

the Fourier transform \mathcal{F} of a time dependent signal $f(t)$ is defined as $g(\omega) = \mathcal{F}(f(t))$, where ω is the angular frequency ($\omega = 2\pi f$), such that

$$g(\omega) = \frac{1}{\sqrt{2\pi}} \int_{-\infty}^{\infty} f(t)e^{i\omega t} dt \quad (\text{A.1})$$

$$f(t) = \frac{1}{\sqrt{2\pi}} \int_{-\infty}^{\infty} g(\omega)e^{-i\omega t} dt \quad (\text{A.2})$$

is the Fourier transform (A.1) and inverse Fourier transform (A.2). The units of $g(\omega)$ and $f(t)$ are the same. Assuming $f(t)$ is real, and that $f(t) \leftrightarrow g(\omega)$ are a transform pair, then the Fourier transform has the following properties:

$$g(-\omega) = g^*(\omega) \quad (\text{A.3})$$

$$f(at) = \frac{1}{|a|} g\left(\frac{\omega}{a}\right) \quad (\text{A.4})$$

$$\frac{1}{|b|} f\left(\frac{t}{b}\right) \leftrightarrow g(b\omega) \quad (\text{A.5})$$

$$f(t - t_0) \leftrightarrow g(\omega)e^{2\pi i\omega t_0} \quad (\text{A.6})$$

$$g(\omega - \omega_0) \leftrightarrow f(t)e^{-2\pi i\omega t_0} \quad (\text{A.7})$$

A.2 Autopower spectrum

The Fourier spectrum of a set of data can be used to find the power spectrum of the signal. The power spectrum of a data set $f(t)$ is given by:

$$S(\omega) = g(\omega)g^*(\omega) \quad (\text{A.8})$$

such that the units of $S(\omega)$ are the square of the units associated with $f(t)$. Power spectra are often presented as one-sided, such that no negative frequencies are given. The one-sided power spectrum is given by:

$$S(\omega) = \begin{cases} g(\omega)g^*(\omega) & \omega = 0, \frac{\omega}{2} \\ 2g(\omega)g^*(\omega) & \text{elsewhere} \end{cases} \quad (\text{A.9})$$

Power spectra curves display the power spectrum or power spectral density of a signal. If we have an N -sample signal $f(t)$ with a Fourier transform $g(\omega)$, then the auto-power spectral density APSD is given by $APSD(\omega) = \frac{g(\omega)g^*(\omega)}{\Delta f}$ where $\Delta f = f_s/N$, and f_s is the sampling frequency.

A.3 Cross-power spectrum,

Given two signals of N samples $f_1(t_n)$ and $f_2(t_n)$, where $n = 1, 2, 3, \dots, N-1, N$, the Fourier transforms of the two signals are given by $g_1(\omega_n)$ and $g_2(\omega_n)$. The cross power spectrum is then given by:

$$H_{1,2}(\omega_n) = g_1(\omega)g_2^*(\omega) \quad (\text{A.10})$$

The coherence is then given by:

$$\gamma_{1,2}^2(\omega_n) = \frac{|H_{1,2}(\omega_n)|^2}{S_1(\omega_n)S_2(\omega_n)} \quad (\text{A.11})$$

or, more importantly, for an ensemble of M signals, the coherence is given by:

$$\gamma_{1,2}^2(\omega_n) = \frac{|\sum_{j=1}^M H_{1,2}^{(j)}(\omega_n)|^2}{[\sum_{j=1}^M S_1^{(j)}(\omega_n)][\sum_{j=1}^M S_2^{(j)}(\omega_n)]} \quad (\text{A.12})$$

where $\gamma_{1,2}^2$ is significant when:

$$\gamma_{1,2}^2(\omega_n) \geq \frac{1}{M}. \quad (\text{A.13})$$

A.4 Wavenumber frequency spectrum

For an ensemble of data N ($n = 1, N$) samples long with M ($j = 1, M$) realizations (e.g. sawtooth crashes, PPCD shots, etc.), with measurements at 2 spatial locations $f_1^{(j)}(t_n)$ and $f_2^{(j)}(t_n)$ with separation χ , there are two sets of Fourier transforms, $g_1^{(j)}(\omega_n)$ and $g_2^{(j)}(\omega_n)$. The cross power is then given by:

$$H_{1,2}^{(j)}(\omega_n) = g_1^{(j)}(\omega_n)g_2^{(j)*}(\omega_n). \quad (\text{A.14})$$

The local phase between the two sets of spectra are then:

$$\Theta^{(j)}(\omega_n) = \tan^{-1}\left(\frac{\Im H_{1,2}^{(j)}(\omega_n)}{\Re H_{1,2}^{(j)}(\omega_n)}\right) \quad (\text{A.15})$$

Where $\Im H_{1,2}^{(j)}(\omega_n)$ is the imaginary part of the cross power spectrum and $\Re H_{1,2}^{(j)}(\omega_n)$ is the real part of the cross power spectrum. The local wavenumber is given by:

$$K^{(j)}(\omega_n) = \frac{\Theta^{(j)}(\omega_n)}{\chi}. \quad (\text{A.16})$$

The wavenumber-frequency power spectrum can then be found by:

$$S(k, \omega) = \frac{1}{M} \sum_{j=1}^M I_{[0, \Delta K]}(k - K^{(j)}(\omega_n)) \frac{S_1^{(j)}(\omega_n) + S_2^{(j)}(\omega_n)}{2} \quad (\text{A.17})$$

Where $\frac{S_1^{(j)}(\omega_n) + S_2^{(j)}(\omega_n)}{2}$ is the average autopower spectrum of the two signals, and

$$I_{[0, \Delta K]}(k - K^{(j)}(\omega_n)) = \begin{cases} 1 & 0 \leq (k - K^{(j)}(\omega_n)) < \Delta K \\ 0 & \text{elsewhere} \end{cases} \quad (\text{A.18})$$

is boxcar function used to determine resolution in wavenumber. The following code is what the author used to calculate the $S(k, \omega)$ spectrum in IDL.

A.5 $S(k, \omega)$ IDL code

IDL routine used to calculate $S(k, \omega)$ plots used in this thesis. Built and maintained by the author.

A.5.1 $S(k, \omega)$ top level code

```

pro skw, shotlist,node1=node1,node2=node2,$
    dt=dt,f_min=f_min,f_max=f_max,title=title

;set defaults for nodes 1&2 as p36 and p43, can also set to other
;chords and magnetics channels
if n_elements(node1) ne 1 then node1 = '\fir_fast_p36'
if n_elements(node2) ne 1 then node2 = '\fir_fast_p43'
;set duration of fft in ms
if n_elements(dt) ne 1 then dt = 1.0
;set minimum and maximum of frequency plotted
if n_elements(f_min) ne 1 then f_min = 0
if n_elements(f_max) ne 1 then f_max = 200
;set displayed plot title for reference
if n_elements(title) ne 1 then title = node1 +' vs ' + node2

;go to external code lsb_skw, which reads an lsb file and calculates
;the spectral power
data = lsb_skw(shotlist,node1,node2,dt)

;number of elements in data array in x and y directions
nx=n_elements(data(*,1))-1
ny=n_elements(data(1,*))-1

;crops data array to extract a frequency array, wavenumber array, and
;skw array
freq_arr=data[nx,0:ny-1]
k_arr=data[0:nx-1,ny]

```

```

skw=data[0:nx-1,0:ny-1]

;save plot to file asdf.eps as encapsulated postscript
plotfile = 'asdf.eps'
set_plot,'ps'
device, /encapsul,filename=plotfile,xsize=8,ysize=8,/color,/inches

;;;;;;following block for plotting the S_kw spectra for a data set

skw_ind=where(skw ne 0.0)
maxdata=max(skw)
mindata=min(skw(skw_ind))
;mindata=max(skw)/50
;print, mindata,maxdata
nl=60
l_c=dblarr(nl)
c_c=dblarr(nl)
cto=1.0
;stop

zer_arr=where(skw eq 0.0)
skw(zer_arr)=mindata/100
skw=log10(skw)
mindata=min(skw(skw_ind))+3.5
maxdata=max(skw)
print, mindata,maxdata

;set minimum and maximum of data for display purposes due to log scaling

```

```

;can adjust lines 51,52 to get colors to display properly
;but must remove 0s from data or plot will fail
skw(where(skw le mindata))=mindata
skw(where(skw ge maxdata))=maxdata

for i=0,nl-1 do begin
    l_c[i]=(maxdata-mindata)*i/(nl-1.0)+mindata
    c_c[i]=(255.0-cto)*i/(nl-1.0)*cto
endfor

skw=10^(skw)
l_c=10^(l_c)
;stop
loadct,39

;error in plotting requires multiple runs, with and without lines
;78-80, to get seperate plots with data and scale
contour,skw,k_arr,freq_arr,/nodata, position=[0.1,0.4,0.8,0.9]$
    ,xtitle='wavenumber (cm^-1)',ytitle='frequency (kHz)',$
    ,xrange=[min(k_arr),max(k_arr)],yrange=[0,f_max],xstyle=1

;contour, rotate([[l_c],[l_c]],1),indgen(2),l_c,/nodata,$
;    position=[0.92,0.4,0.96,0.9],/noerase,xtitle='',ytitle='power (A.U.)',ylog=1,$
;    yrange=[10^floor(mindata),10^ceil(maxdata)];,ystyle=1

loadct, 22

```

```

contour,skw,k_arr,freq_arr,c_linestyle=1,$
    levels=l_c,c_color=c_c,/fill,/overplot, position=[0.1,0.4,0.8,0.9],/noerase

contour, rotate([[l_c],[l_c]],1),indgen(2),l_c,$
    levels=l_c,c_colors=c_c,/overplot,$
    /fill, position=[0.92,0.4,0.96,0.9],/noerase,ylog=1

;print, mean(phi[ind2]*180./!pi)
;stop
device,/close
end

```

A.5.2 lsb_skw.pro subroutine

```

function lsb_skw, file, node1, node2, dt,tselp=tselp,debug=debug

debug = 0
if n_elements(tselp) eq 0 then tselp=16.

    openr,lun1, file+'.lsb',/get_lun
    print, file+'.lsb opened for reading'
    tmp = ''
    readf, lun1, tmp

    shot = 0

```

```

date = '11-111-1111'
t1 = 0
t2 = 0
nreal = 0
tsel = 0.E0
data = fltarr(10)
i = 0
s = 0

readf,lun1,tmp
readf,lun1,format='(i3,2x,a11,2x,i3,2x,i3,2x,i2)',shot,date,t1,t2,nreal

while date ne '00-000-0000' do begin

    for s =0,nreal-1 do begin

        shotf = get_mdsplus_shot(shot,date) ;open shot
                ;print, shotf
        readf,lun1,format='(e12.5,2x,i1)',tsel
    ;endfor

                tsel = tselp ;for selecting a time
                ;other than the one in the lsb file

    ;tsel = tsel+2.0

                tsel = 10.

    data1_arr = raw_data(shotf,node1,tsel,dt)

```

```

if keyword_set(debug) then begin

    ndata = data1_arr[n_elements(data1_arr)-1]
                ;taxis = findgen(ndata)*(1./data1_arr[n_elements(data1_arr)-2])

    f0 = 20.
    f1 = 55.
    f2 = 200.

    noise =0                ;randomu(seed,ndata)*0.1
    data1_arr[0:ndata-1] = cos(2.*!PI*f0*data1_arr[ndata:2*ndata-1]) + $
                cos(2.*!PI*f1*data1_arr[ndata:2*ndata-1]) + $
                3.*cos(2 *!PI*f2*data1_arr[ndata:2*ndata-1]) +noise

endif

n1 = data1_arr(n_elements(data1_arr)-1)
sig1 = data1_arr(0:n1-1)*sqrt(52^2-28^2)/sqrt(52^2-43^2)
stm1 = data1_arr(n1:2*n1-1)
sampr1 = data1_arr(2*n1)
den1 = mean(sig1)
if den1 lt 0.0 then sig1 = -sig1

data2_arr = raw_data(shotf,node2,tse1,dt)

if keyword_set(debug) then begin

    ndata = data2_arr[n_elements(data2_arr)-1]
    noise =randomu(seed,ndata)*0.1

```

```

        data2_arr[0:ndata-1] = cos(2.*!PI*f0*data2_arr[ndata:2*ndata-1] + 50.*!DTOR) +
                                cos(2.*!PI*f1*data2_arr[ndata:2*ndata-1] + 35.*!DTOR) +
endif

n2 = data2_arr(n_elements(data2_arr)-1)
sig2 = data2_arr(0:n2-1)
stm2 = data2_arr(n2:2*n2-1)

                                ;temp = sig2
                                ;sig2 = interpol(temp, stm2, stm1)
                                ;stm2 = stm1

sampr2 = data2_arr(2*n2)
den2 = mean(sig2)
if den2 lt 0.0 then sig2=-sig2

n = n1<n2
h1 = hanning(n,/double)
h2 = hanning(n,/double)

                                ;stop

                                ;sig1 = sig1-mean(sig1)
                                ;sig2 = sig2-mean(sig2)

ft1 = fft(sig1*h1,-1)
ft2 = fft(sig2*h2,-1)

```

```
;stop
```

```
ft1 = ft1(0:n-1)*2
```

```
ft2 = ft2(0:n-1)*2
```

```
node_loc1 = strsplit(node1, '_', /extract)
```

```
node_loc1 = node_loc1(0)
```

```
node_loc2 = strsplit(node2, '_', /extract)
```

```
node_loc2 = node_loc2(0)
```

```
;print, node_loc1,node_loc2
```

```
if node_loc1 eq '\Bpdot' or node_loc1 eq '\Btdot' then begin
```

```
    freq_arr = (findgen(n))*(sampr1/n)
```

```
    freq_arr(where(freq_arr lt 1.)) = 1.
```

```
    ft1 = ft1/(2 * !pi* freq_arr)
```

```
endif
```

```
if node_loc2 eq '\Bpdot' or node_loc2 eq '\Btdot' then begin
```

```
    freq_arr = (findgen(n))*(sampr2/n)
```

```
    freq_arr(where(freq_arr lt 1.)) = 1.
```

```
    ft2 = ft2/(2 * !pi* freq_arr)
```

```
endif
```

```
s12 = conj(ft1)*ft2
```

```
s11 = abs(ft1)^2
```

```
s22 = abs(ft2)^2
```

```

nra = n_elements(s12)
freq_arr = (findgen(nra))*sampr1/nra

freq_ind=where(freq_arr ge 5.0 and freq_arr le 150.)
freq_arr=freq_arr(freq_ind)
;print, i
phi = atan(imaginary(s12(freq_ind)),real_part(s12(freq_ind)))
x=16.5          ;16.5 cm for regular setup, p43 and p36
;x=1.5          ;1.5 cm for 2 mixer setup
;x=13.9         ;13.9 cm for regular setup, p06 and p13
int=50
k=phi/x
k_max=!pi/x
;stop
del_k=k_max/int
skw_tmp = make_array(2*int+1,n_elements(freq_arr))
k_arr=indgen(int*2+1)*del_k-k_max+del_k/2
k_arr(n_elements(k_arr)-1)=0
for q=0,2*int-1 do begin
    w_tmp=make_array(n_elements(freq_arr))
    w_allowed=where(k gt k_arr(q) and k le k_arr(q+1))
    w_tmp(w_allowed)=1
    skw_tmp(q,*)=w_tmp*(s11(freq_ind)+s22(freq_ind))/2
    ;if max(skw_tmp gt 0.01) then skw_tmp(where(skw_tmp eq max(skw_tmp)))=0
;stop
endfor
;stop
;if max(skw_tmp) gt 0.01 then begin

```

```
        ;   skw_tmp(where(skw_tmp eq max(skw_tmp)))=0
;stop
;endif

if i eq 0 then begin
    sum_sig1 = sig1
    sum_sig2 = sig2
    sum_stm1 = stm1
    sum_stm2 = stm2
    sum_s12 = s12
    sum_s11 = s11
    sum_s22 = s22
    sum_ft1 = ft1
    sum_ft2 = ft2
    sum_skw = skw_tmp
    i = i+1
endif else begin
    sum_sig1 = sum_sig1+sig1
    sum_sig2 = sum_sig2+sig2
    sum_stm1 = sum_stm1+stm1
    sum_stm2 = sum_stm2+stm2
    sum_s12 = sum_s12+s12
    sum_s11 = sum_s11+s11
    sum_s22 = sum_s22+s22
    sum_ft1 = sum_ft1+ft1
    sum_ft2 = sum_ft2+ft2
    sum_skw = sum_skw+skw_tmp
    i = i+1
```

```

endelse

print, i
;plot, freq_arr, (s11^2)/i, xrange=[0,100], ylog=1, yrange=[1e-12,1e-7]
;oplot, freq_arr, (sum_s22^2)/i, psym=-1
;plot, freq_arr, (sum_s11^2)/(sum_s22^2), xrange=[0,200], yrange=[-2,20]
;plot, freq_arr, atan(imaginary(s12), real_part(s12))*180./!pi/5., xrange=[0,100]
;stop

endfor
;print, max(skw_tmp)
;print, where(skw_tmp eq max(skw_tmp))
;stop

readf, lun1, tmp
readf, lun1, format='(i3,2x,a11,2x,i3,2x,i3,2x,i2)', shot, date, t1, t2, nreal

endwhile

print, i

;sum_phi = atan(imaginary(sum_s12), real_part(sum_s12))
sampr = fltarr(n_elements(sum_ft1))
sampr(0) = sampr1<sampr2
sampr(1) = i
sampr(2) = den1
sampr(3) = den2

```

```

;print, sampr1, sampr2
;data_arr = [[sum_sig1],[sum_sig2],[sum_stm1],[sum_stm2],[sampr*i]]
;data_arr=[[sum_ft1],[sum_ft2],[sum_s11],[sum_s22],[sum_s12],[sum_phi*i],[sampr*i]]

data_arr = [[sum_skw/i]]
data_arr(int*2,*)=freq_arr
data_arr = [[data_arr],[k_arr]]
;stop

free_lun,lun1

return, data_arr

end

```

A.5.3 Other subroutines

The subroutine 'lsb_skw.pro' calls a few other subroutines for fairly trivial tasks. For example, the routine 'raw_data.pro' simply finds the data associated with the given data path, time, and shot number and saves it to the specified variable. Various other routines, like 'fft' and 'hanning', are defined in IDL and can be looked up independently. These routines are trivial enough to not be included in the text of this thesis.

APPENDIX

Other plots

B.1 $S(k, \omega)$ plots across the diameter of the plasma

Figure 5.7 represents the largest observed spectral power between two chords through the plasma for the ensemble of 200kA PPCD plasmas. However, as each chord passes through the edge region of the plasma, each pair of toroidally separated chords can measure an $S(k, \omega)$ plot for each ensemble of data in this thesis. Following are plots for alternating chords, starting with the data from figure 5.7 in figure B.1(top), and alternating chords through the full minor radius of the plasma.

In figure B.1 the signal at chord p36 is compared to the signal at chords p43 (top) and p28 (bottom). The observed spectral power is largest in the first plot, and drops significantly further in at p28, and has the same peak frequency and wavenumber. Figure B.2 moves in further to comparing the signal at chord p21 to the signal at chord p28 (top) and p13 (bottom). There is a further decrease in spectral power for the density fluctuations at ~ 50 kHz and ~ 15 kHz and $\sim -0.10 - 0.15 \text{cm}^{-1}$, and an increase in the observed spectral power associated with the residual magnetic tearing fluctuations, at ~ 15 kHz and $\sim 0.02 - 0.03 \text{cm}^{-1}$. Figure B.3 looks at the core of the plasma, using the chord p06 compared to chord p13 (top) and n02 (bottom). The density fluctuation power between these chords is quite low, on the order of $10^{30} \text{m}^{-4} / \text{kHz}$, at wavenumber $k \sim -.15$ and $k \sim .14$, respectively. Figure B.4 looks toward the inboard core of the plasma, comparing chord n09 to chords n02 (top) and chord n17 (bottom). The mode power increases as the gradients increase on the inboard side of the plasma, and the wavenumbers peak at ~ -0.1 for both plots. Figure B.5 looks toward the inboard edge of the plasma, comparing chord n24 to chords n17 (top) and chord n32 (bottom). Dynamics for these sets of chords becomes a bit odd,

with each $S(k, \omega)$ plot becoming fairly broad for the spectral feature. the wavenumber peaks at ~ -0.12 for both plots, but is very broad, with significantly less peaking than in figure B.1.

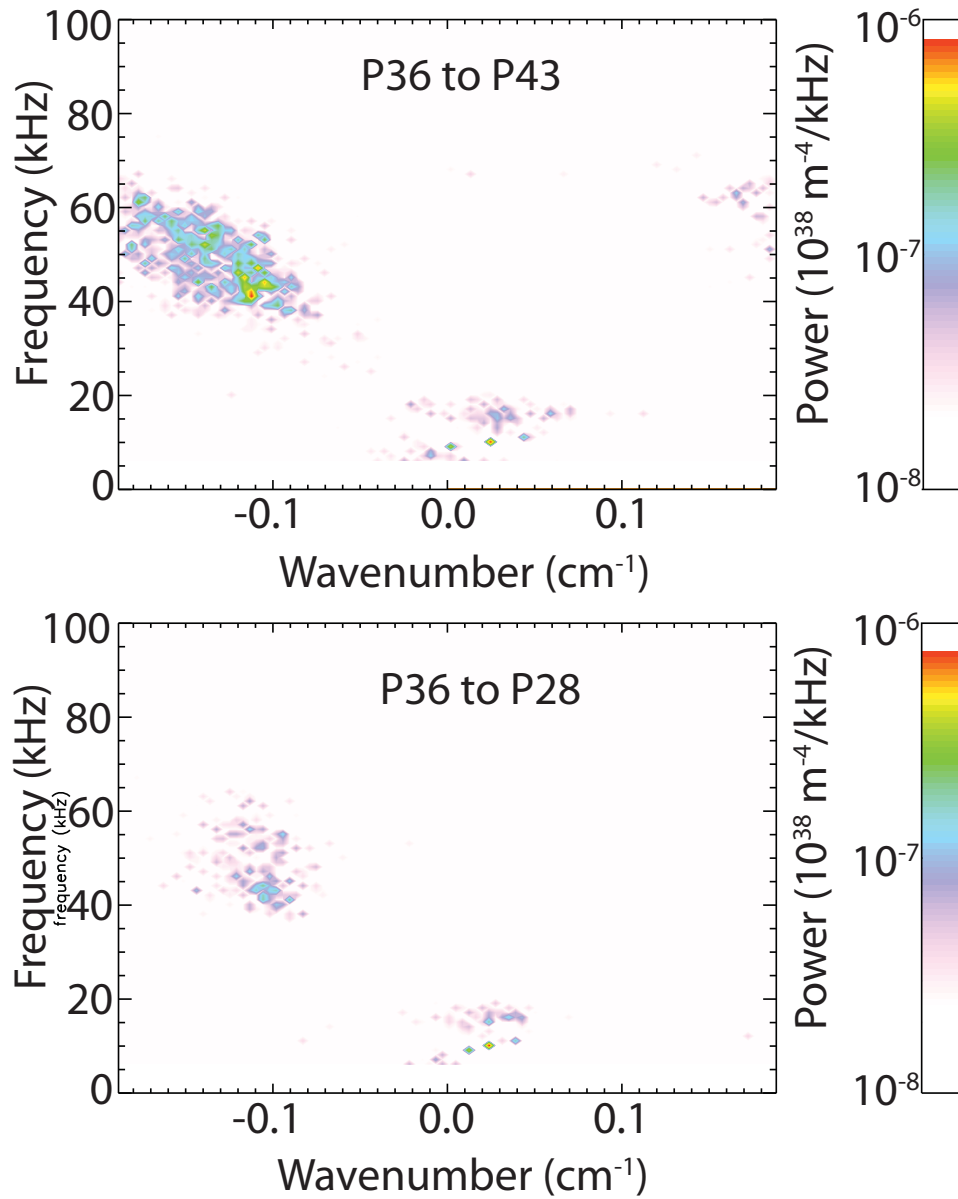


Figure B.1 Frequency-wavenumber power spectrum of the line-integrated electron density fluctuations between chords at impact parameters of (a) $R - R_0 = 36, 43\text{cm}$ and (b) $R - R_0 = 36, 28\text{cm}$.

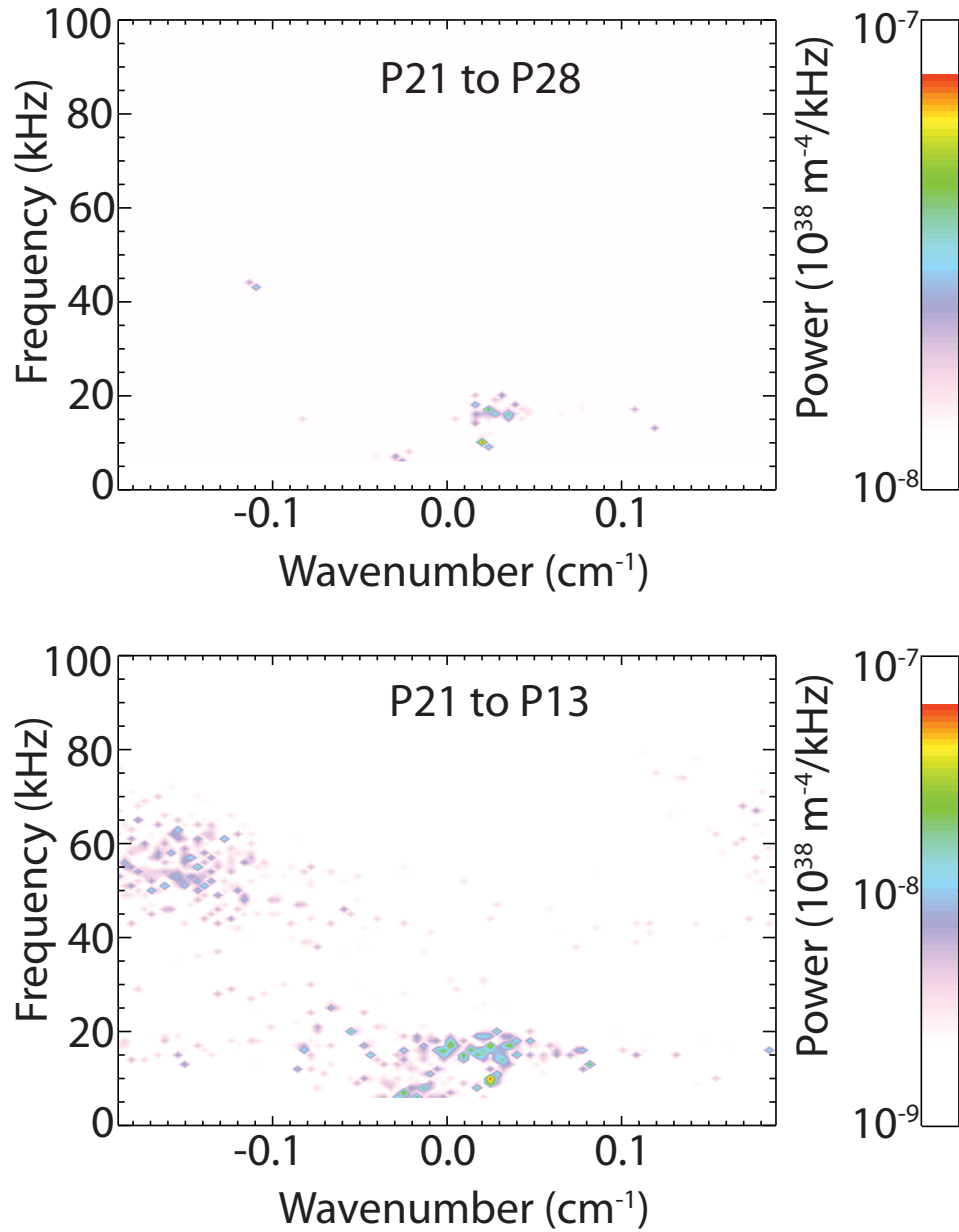


Figure B.2 Frequency-wavenumber power spectrum of the line-integrated electron density fluctuations between chords at impact parameters of (a) $R - R_0 = 21, 28\text{cm}$ and (b) $R - R_0 = 21, 13\text{cm}$.

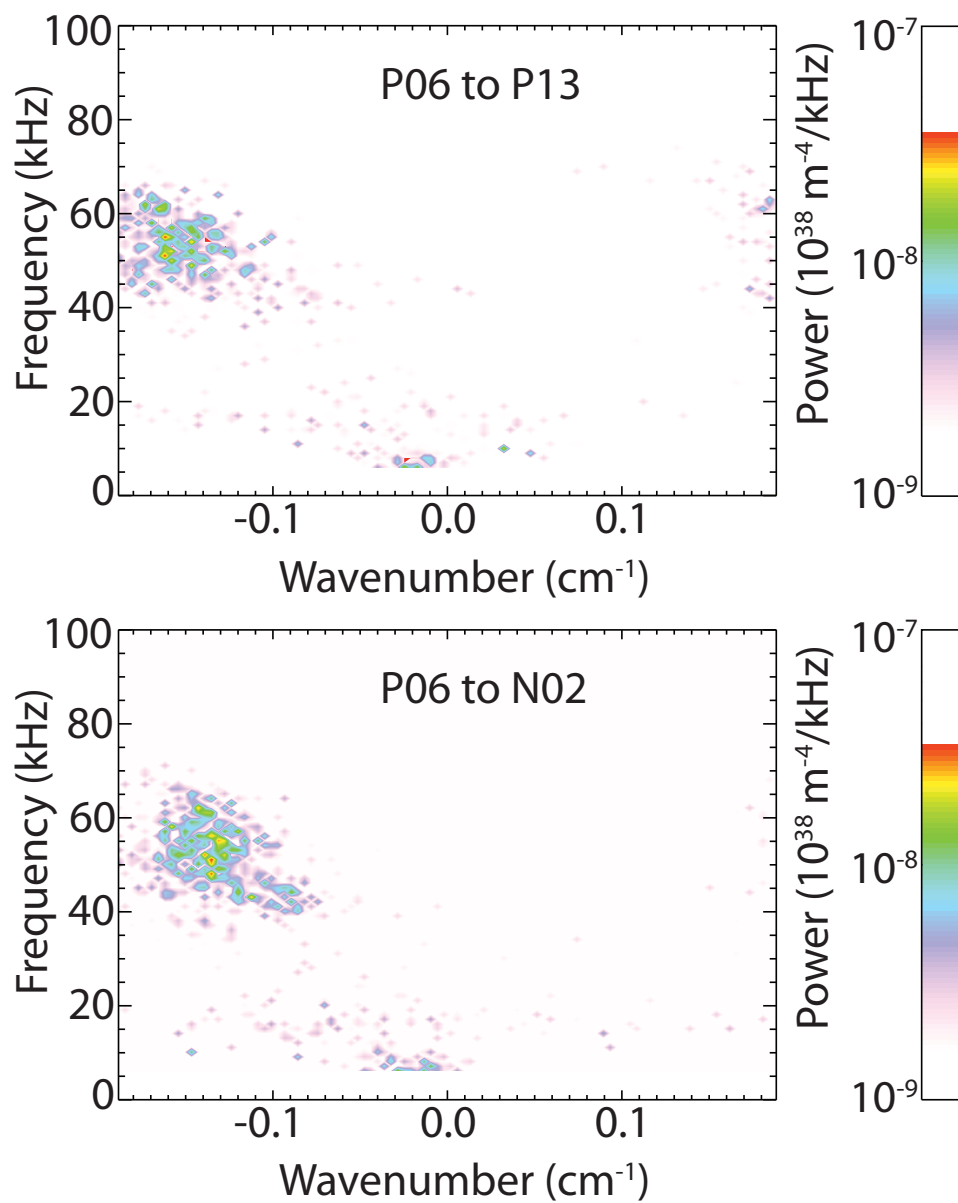


Figure B.3 Frequency-wavenumber power spectrum of the line-integrated electron density fluctuations between chords at impact parameters of (a) $R - R_0 = 6, 13\text{cm}$ and (b) $R - R_0 = 6, -2\text{cm}$.

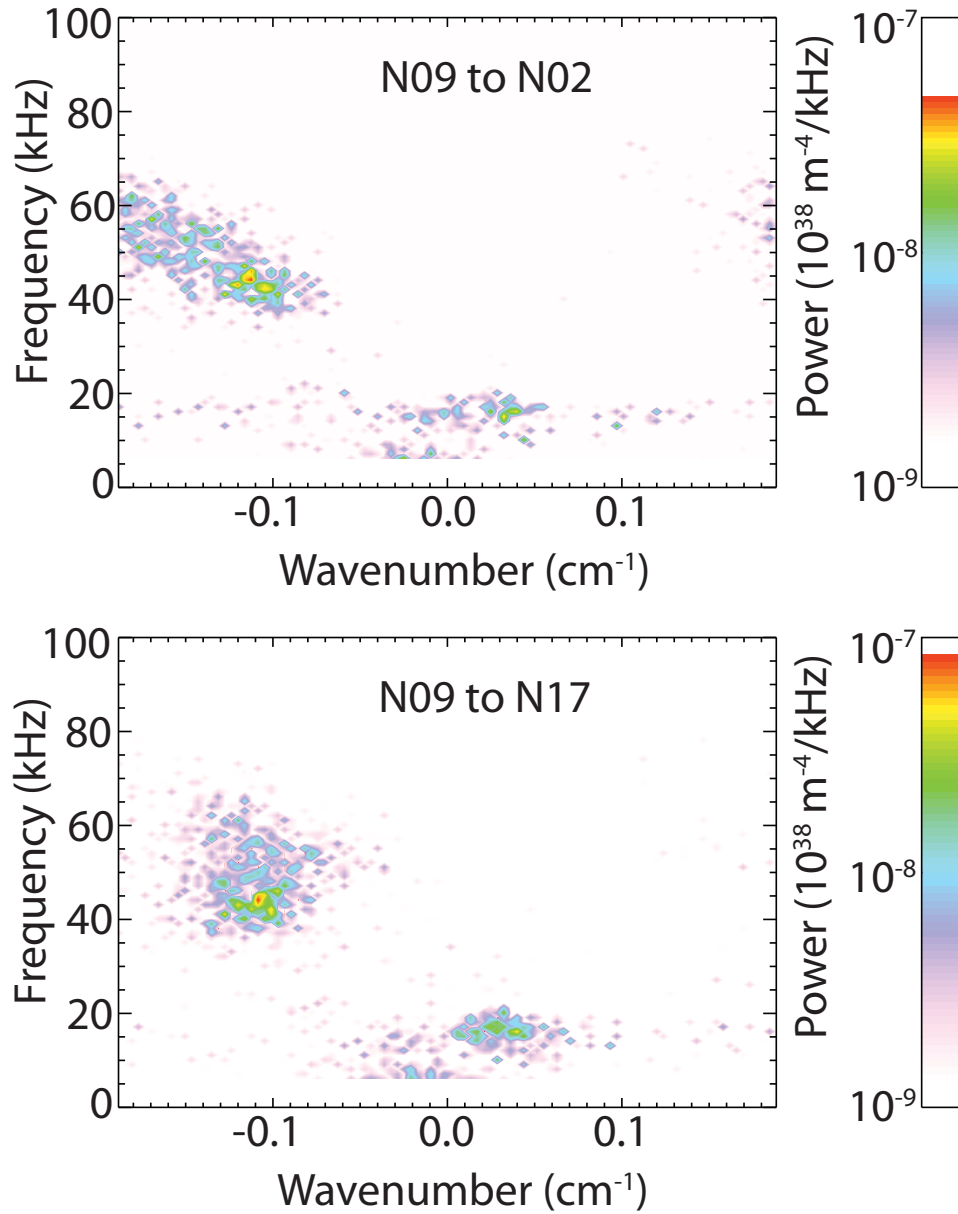


Figure B.4 Frequency-wavenumber power spectrum of the line-integrated electron density fluctuations between chords at impact parameters of (a) $R - R_0 = -9, -2$ cm and (b) $R - R_0 = -9, -17$ cm.

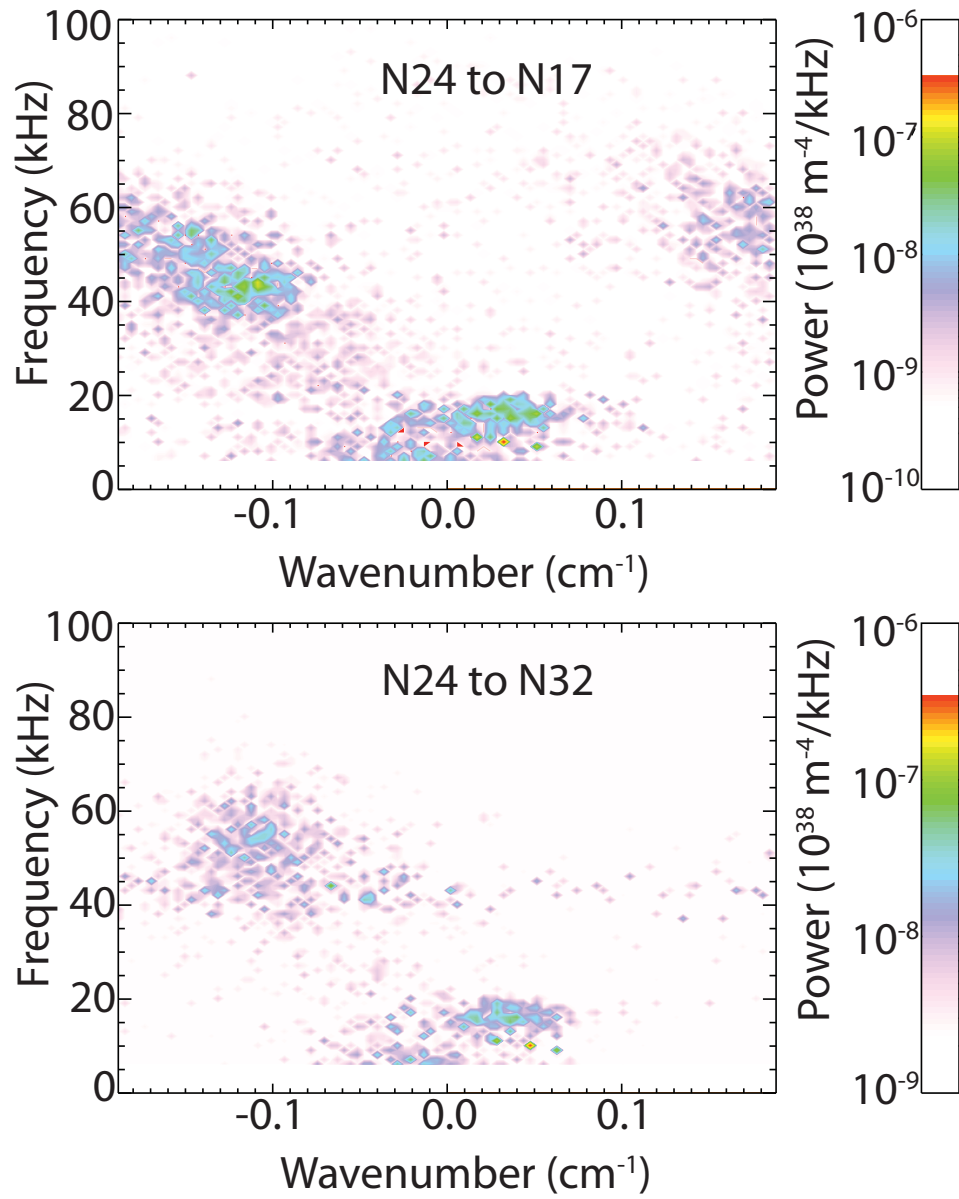


Figure B.5 Frequency-wavenumber power spectrum of the line-integrated electron density fluctuations between chords at impact parameters of (a) $R - R_0 = -24, -17$ cm and (b) $R - R_0 = -24, -32$ cm.